DOTTORATO DI RICERCA IN CHIMICA

Convenzione tra

UNIVERSITÀ DEGLI STUDI DI TRIESTE

e

UNIVERSITÀ CA' FOSCARI DI VENEZIA

CICLO XXX

DESIGN AND PREPARATION OF CARBON NANODOTS FOR BIOMEDICAL APPLICATIONS

Settore scientifico-disciplinare: **CHIM/06**

DOTTORANDA
INMACULADA JÉNNIFER GÓMEZ PÉREZ

COORDINATORE
PROF. MAURO STENER

SUPERVISORE DI TESI
PROF. MAURIZIO PRATO

ANNO ACCADEMICO 2016/2017

Acknowledgments

The end always finds its own way. The end of these three years as a PhD student has arrived. I wasn't alone in this period and I could not have had a better company to walk along this way. There are many people to whom I have to say thank you. Thanks for contributing somehow in this thesis, by helping with an experiment or by simply smiling during the bad days. Every little detail was important to reach the final goal!

Foremost, I would like to express my deepest and most sincere gratitude to my supervisor Prof. Maurizio Prato. Thanks for giving me the opportunity to join his group as a PhD student and for the continuous support, something that I will never forget.

Besides my advisor, I am especially grateful to Francesca, who taught me how to make CNDs, without that this thesis would have never happened. "Grazie mille" for your continuous support and for being there for me any time.

Prof. Tatiana Da Ros, thanks for your wise advises and for taking care of all the members of the group and of course for your amazing Christmas's dinners.

Part of the work of this thesis would have never happened without the help of the collaborators and the technician support from the University of Triste and CIC biomaGUNE. I am thankful to Dr. Carolina Carrion and Prof. Wolfgang J. Parak for the work developed in Chapter 4. Dr. Sonia Serna for the help with MALDI technique and Dr. Blanca Arnaiz for their support and work in all the biological experiments. Claudio Gamboz for his lessons and support in TEM images. Prof. Mauro Stener, Michela, Franco, Manuela, Ricardo, Luigi, Luis and Javi. To all of them, I show my gratitude, your work has been absolutely necessary to developed this thesis.

I would like to thank all the members of the Prato's group, for making me feel at home even when I was so faraway from it. Ana, I cannot acknowledge you enough for all the times that I disturbed you with chemistry doubts. Agnieszka, my polish friend! It was a pleasure to share with you both lab and office. Tanja, for your compression. Valentina, for always being so lovely. Maria, for being one of the most adorable persons I have ever known. Jose and Caroline, for being good friends inside and outside the lab. Francesco, for all the Italian lessons and the good moments in mensa. Dani and Ana for being always willing to help. Thanks to all the other labmates of the group during over 3 years: Angela, Andrea, Cristina, Davide, Susanna, Zois, Luka, Eva, Michele, Vicky, Federico, Alexa and Lorenzo.

I don't forget either those who came to the group for short periods of time, but yet made a difference: Radek, thanks for the support with magnetic nanoparticles.

Robert, thanks for spicing up our meals with your stories and Iro, thanks for all the great moments and the good talks both inside and outside the lab.

I also met wonderful people outside the lab who helped me to maintain the mental sanity beyond chemistry. Martu, Mauro, Fabri, Elena, Laura and Hector, thanks to all of you for the great memories that we created.

Half way through my PhD, I moved to San Sebastian where I met Blanca. She was the person who taught me about the world of the cells, thanks for sharing with me your knowledge. Juampe, thanks for all the laugher in the lab. Antonio, thanks for bringing your magic to the lab, for all the good moments and for your friendship. HuiLei, thanks for all the chinese lessons it was a pleasure to learn more about your country. “Eskerrik asko” to all the rest of the friends from biomagune for all the good moments: Anna, Julie, Cris, Maria, Eli, Álvaro, Javi, Juan, Dorleta, Susana, Idoia, Carolina, Bea, Anabel and Elena.

I have to highlight a few people I shared every step of this way with: Alex, it doesn’t matter the place, Santiago, Trieste or San Sebastian, you are always there willing to help and giving good advices. Thanks for all the amazing moments inside and outside the lab. Arturo, my favorite manchego, thank you for being always there for me and for the great stories that we share. Núria, my bestie, the word thank is not enough. I couldn’t be more grateful with you, for your help, your advices, for being just the way you are…I’ll always be there for you.

In the way to become Dr. I couldn’t forget to thank my first chemist family: Astu, Marina, Maru, Lili, Iván, Xoel, Sabela and Paula for all the support over these 9 years together. My first mentor Prof. Diego Peña, for their lessons and good advices. My labmates from CIQUS: Sara, Andrea, Manuel Vilas, García, Lojo for being the most easy-going people in the world, thanks for everything.

Gracias a todos mis amigos de Creciente por seguir ahí a pesar de la distancia: Chupe, Alba, Angela, Martínez, Díaz, Elva. Especialmente a Ana Robles y mis cascarillas, Cecilia y Chelo, por escucharme siempre y darme los mejores consejos.

Desexo agradecerlle as personas máis importantes da miña vida o seu incondicional apoio e todo o seu cariño. A miña abueliña, meu pai e miña nai por confiar en min sempre sen dudalo. Meu irmá e miña cuñada, por escoitarme sempre e animarme nos malos momentos. Meu afillado Anxo, por facer feliz a miña vida. A meu abueliño, por todo o cariño que sempre me deches.

Finally, I could not be more thankful to have Manu as my partner in crime in this adventure. My roommate, labmate, officemate and of course my friend. The person who suffered and enjoyed the most all the emotions I could possibly have experience over these three years. I wish you the best because you really deserve it. Gracias amigo por ser tú!

Now, when I look back I realize that I am the luckiest person in the world to have you all to helping me in the way to became Dr. For all of this, my sincerer gratitude!

Moitas gracias,

Jénnifer

A mis padres y mis abuelos

A mi hermano e Inés

A mi ahijado

Index

List of abbreviations

A549: Human lung cancer cell line

A.C: Alternate current

ACD: Amphiphilic carbon dots

AFM: Atomic force microscopy

Arg: L-arginine

ATPR: Atom-transfer radical-polymerization

BBB: Blood brain barrier

BSA: Bovine serum albumina

CBL: Chlorambucil

C-Dots: Carbon dots

CNDs: Carbon nanodots

CNMs: Carbon nanomaterials

CNTs: Carbon nanotubes

CPS: Counts per second

CQDs: Carbon quantum dots

CV: Cyclic voltammetry

Cy5: Sulfo-Cyanine 5

Cy7: Sulfo-Cyanine 7

DAPI: 4',6-diamidino-2-phenylindole

D.C: Direct current

DDS: Drug delivery system

DEGd: [2-(2-Methoxyethoxy)ethoxy]acetyl chloride

DETA: Diethylenetriamine

DI: Deionized

DIPEA: *N,N*-diisopropylethylamine

DLS: Dynamic light scattering

DMAP: 4-dimethylaminopyridine

DMEM: Dulbecco's modified eagle medium

DMF: N,N-dimethylformamide

DNA: Deoxyribonucleic acid

DOX: Doxorubicin

DWCNTs: Double-walled carbon nanotubes

ECL: Electrochemiluminescence

EDA: Ethylenediamine

EDC: 1-Ethyl-3-(3-dimethylaminopropyl)-carbodiimide

EDIPA: Ethylenediisopropylamine

equiv: Equivalents

FBS: Fetal bovine serum

FITC: Fluorescein isothiocyanate

FL: Fluorescence

FRET: Fluorescence resonance energy transfer

FTIR: Fourier transform infrared

FWHM: Full width at half maximum

GO: Graphene oxide

GQDs: Graphene quantum dots

HDFa: Human dermal fibroblasts cell line

HeLa: Cervix cancer cells

HepG2: Human liver cancer cell line

HRTEM: High-resolution transmission electron microscopy

HSA: Human serum albumin

HUVEC: Human umbilical vein endothelial cells

IC_{50}: Half maximal inhibitory concentration

IR: Infrared

KT: Kaiser test

LDA: Laser doppler anemometry

LED: Light-emitting diode

LSCM: Laser scanning confocal microscopy

MALDI-TOF: Matrix-assisted laser desorption ionization time-of-flight

MB: Methylene blue

MCF-7: Human breast cancer cell line

MDA-MB-231: Breast human cancer cell lines

MFI: Mean fluorescence intensity

NCNDs: Nitrogen-doped carbon nanodots

MTS: (3-(4,5-dimethyl-thiazol-2-yl)-5-(3-carbocymethoxyphenyl)-2-(4-sulfophenyl)-2H-tetrazolium

MTT: 3-(4,5-dimethylthiazol-2-yl)-2,5-diphenyltetrazolium bromide

MW: Molecular weight

MWCNTs: Multi-walled carbon nanotubes

NHS: N-hydroxysuccinimide

NIR: Near infrared

NMR: Nuclear magnetic resonance

NP: Nanoparticle

OLED: Organic light-emitting diode

P_{app}: permeability coefficient

PBS: Phosphate buffer saline

PC-3: Human prostate cancer cell line

PC: Protein corona

PCDs: Polymer carbon dots

PET: Photoinduced electron transfer

PL: Photoluminescence

PTX: Paclitaxel

QDs: Quantum dots

QY: Quantum yield

RBITC: Rhodamine B isothiocyanate

RNA: Ribonucleic acid

SEC: Size exclusion chromatography

SEM: Scanning electron microscope

SWCNTs: Single-walled carbon nanotubes

TEM: Transmission electron microscopy

TEPSA: 3-(triethoxysilyl)propylsuccinic anhydride

TFA: Trifluoroacetic acid

TGA: Thermogravimetric analysis

Tris: Tris(hydroxymethyl)methyl aminomethane

UCPL: Up-conversion photoluminescence

UHV: Ultra-high vacuum

XPS: X-ray photoelectron spectroscopy

XTT: 2,3-bis-(2-methoxy-4-nitro-5-sulfophenyl)-2H-tetrazolium-5-carboxanilide

ς-potential: Zeta potential

Abstract

Riassunto

In the last few decades great efforts have been placed in studying carbon nanomaterials. Nowadays the nanocarbon family spans from fullerene, the first member, to Carbon Dots (C-Dots), the last to join. C-Dots have attracted considerable attention for a wide range of applications, especially bioapplications, because of their properties: emission, small sizes, aqueous solubility, biocompatibility and chemical stability.

The aim of this doctoral thesis was to synthesize carbon nanodots (CNDs), in particular nitrogen-doped CNDs, and functionalize their surface with properly designed molecules/biomolecules for bioapplications.

In the first chapter, an introduction on the different types of C-Dots is provided, with a particular emphasis on CNDs. An overview of their most common production methods, characterization techniques and properties is given. A brief discussion on their applications, especially bioapplications, is reported.

In chapter 2, highly fluorescent and water-soluble nitrogen-doped CNDs were prepared. A simple bottom approach by employing low-cost carbon and nitrogen sources (arginine and ethylenediamine) was used. The as-prepared CNDs were purified and characterized. They showed an excitation wavelength dependent emission, several functional groups on their surface such as amines and a narrow size distribution.

Chapter 3 reported the covalent and non-covalent modification of CNDs in preparing hybrid materials for diverse bioapplications. The covalent modification of the CNDs surface with iron nanoparticles or drugs, such as paclitaxel and chlorambucil, was described. Moreover, it was studied the attachment of human serum albumin *via* non-covalent approaches.

The Chapter 4 focused on the *in vitro* bioapplications of the materials described in chapter 3 as drug delivery systems, bioimaging agents and nanocarriers. Moreover, the effect of a protein corona around CNDs on their cellular uptake it was studied, since it is a prerequisite for their successful use for such applications. The CNDs and related materials presented non-toxicity, biocompatibility and good cellular imaging capability. They were tested through the IC_{50} and a high pharmacological activity in solid tumors was observed. Finally, their *in vitro* permeability was evaluated through an inverted BBB using a real-time cell response and observing that they are able to cross the BBB model.

I nanomateriali di carbonio sono stati ampiamente studiati negli ultimi decenni. Questa famiglia di materiali va dal fullerene, che è stato il primo ad essere scoperto, ai Carbon Dots (C-Dots), gli ultimi membri che sono entrati a farne parte. I C-Dots hanno attratto un considerevole interesse per un'ampia gamma di applicazioni, specialmente in ambito biologico, grazie alle loro proprietà di emissione, piccole dimensioni, solubilità in acqua, biocompatibilità e stabilità chimica.

Lo scopo di questa tesi di dottorato è stato di preparare carbon nanodots (CNDs), in particolare CNDs dopati con azoto, e di funzionalizzare la loro superficie con molecole/biomolecole opportunamente scelte per la loro applicazione biologica.

Nel primo capitolo, viene fornita una introduzione sulle diverse tipologie di C-Dots, con una particolare enfasi sui CNDs. Viene presentata una panoramica sui loro più comuni metodi di preparazione, tecniche di caratterizzazione e proprietà. Infine, è riportata una breve discussione sulle loro applicazioni, specialmente in ambito biologico.

Nel secondo capitolo viene descritta la preparazione di CNDs dopati con azoto, altamente fluorescenti e solubili in acqua. È stato impiegato un semplice metodo *bottom-up* utilizzando dei precursori a basso costo come fonti di carbonio e azoto (arginina ed etilendiammina). Tali CNDs sono stati purificati e caratterizzati. Essi hanno mostrato una emissione dipendente dalla lunghezza d'onda di eccitazione, molti gruppi funzionali sulla loro superficie, come ad esempio ammine, e una stretta distribuzione dimensionale.

Nel capitolo 3 è presentata la modificazione covalente e non covalente dei CNDs al fine di preparare dei materiali ibridi per varie applicazioni biologiche. Viene descritta la modificazione covalente degli CNDs con nanoparticelle di ferro o farmaci, come il paclitaxel e il clorambucile. Inoltre, è stata studiata la coniugazione di sieroalbumina umana attraverso approcci non covalenti.

Il capitolo 4 è incentrato sulle applicazioni biologiche *in vitro* dei materiali descritti nel capitolo 3, come sistemi di drug delivery, agenti per bioimaging e nanocarrier. Inoltre, è stato studiato l'effetto di una proteina corona attorno ai CNDs sul loro uptake cellulare, dal momento che esso rappresenta un prerequisito per il loro uso in tali ambiti. I CNDs e i relativi materiali hanno mostrato di non indurre tossicità, di essere biocompatibili e di essere capaci di ottime capacità di imaging cellulare. Essi sono stati testati mediante IC_{50} ed è stata osservata una elevata attività farmacologica in tumori solidi. Infine, è stata valutata la loro permeabilità *in vitro* attraverso un BBB invertito utilizzando una risposta cellulare in tempo reale e osservando che sono in grado di attraversare il modello BBB.

CHAPTER 1

Introduction

CHAPTER 1

Introduction

"The discovery of carbon atom has revolutionized the science and technology to a great extent and now it is reality that carbon has the potential to make the chemistry stable. It is believed that the discovery of carbon-related materials and their development will be crucial for the future of chemistry and technology. The existing works of literature reflected that carbon is the most studied element of the nano era." Nobel Laureate Dr. Richard Smalley

1. Carbon nanomaterials

Carbon is one of the most abundant element on the Earth's crust and it is present on the nature with different allotropic forms. The world-renowned allotropes of carbon are graphite and diamond, among the many that are possible (**Figure 1.1**). During the last few decades great efforts has been placed in studying carbon nanomaterials, and nowadays these efforts had paid off with a wide family of nanocarbons from fullerene, the first member, to Carbon Dots (C-Dots), the last to join.[1]

Nanomaterials are defined by their morphological properties, smaller than 1μm in at least one dimension. However, generally their size is restricted from 1 to 100 nm.[2] Carbon nanomaterials can be classified according to their dimensionality: zero-dimensional, such as fullerene; one-dimensional, such as carbon nanotubes; and two-dimensional, such as graphene. The nanocarbon family have gained tremendous interest since the discovered of the first member, which was the fullerene by Harold W. Kroto, Robert F. Curl and Richard E. Smalley in 1985.[3] This discovery gave them the Nobel Prize in 1996. The most common fullerene is composed by 60 atoms of

carbon (C_{60}). C_{60} is an insoluble or only sparingly soluble in most solvents material with a spherical shape and its surface contains 20 hexagons and 12 pentagons. The sp^2 carbon atoms can form single or multiple sheet rolled up in a cylindrical shape called carbon nanotubes (CNTs) discovered in 1991 by Iijima.[4] A general classification for CNTs is based on the number of layers or walls they are made of, such as single wall CNTs (SWCNTs) or multi-walled CNTs (MWCNTs). Another material with carbon atoms in a sp^2 hybridization arranged in a hexagonal lattice is graphene.[5] In 2010 the Nobel Prize was awarded jointly to Andre Geim and Konstantin Novoselov for their prominent discovery regarding the two dimensional material graphene. Another allotrope that are not composed by sp^2 carbon atoms, but consists of sp^3 carbon atoms, is the nanodiamond.[6] The last member to join the carbon family was the fluorescent carbon dot (C-Dots) that will be fully described in the following sections.

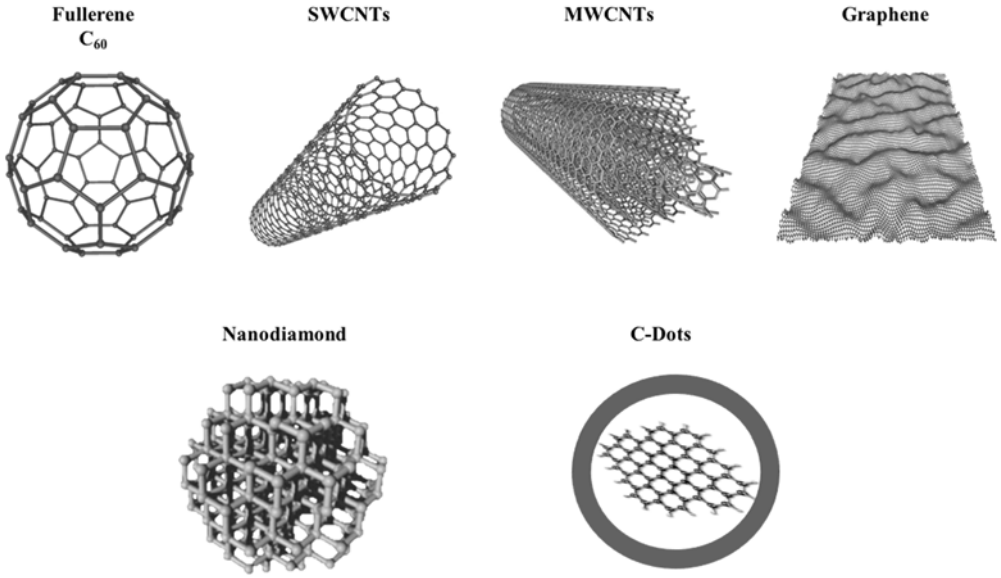

Figure 1.1. Most representative examples of the nanocarbon family.

All these nanocarbons have inspired an extensive and novel science field not only because of their unique properties, but also due to their great potential for a wide variety of applications, from electronics to biomedicine.[7]

1.1. Carbon-based dots

C-Dots were serendipitously discovered in 2004 by Walter A. Scrivens and colleagues in the University of South Carolina.[8] They described a preparative electrophoretic method to purify SWNTs derived from arc-discharge soot (**Figure 1.2**). Since the authors used arc-discharge to prepare CNTs, the latter contained several impurities. During the material purification, by means of a traditional gel

electrophoresis of agarose gel slab, an unexpected luminescent fraction was discovered and isolated from the crude (**Figure 1.2**). It was a mixture of fluorescent nanoparticles, known today as C-Dots.

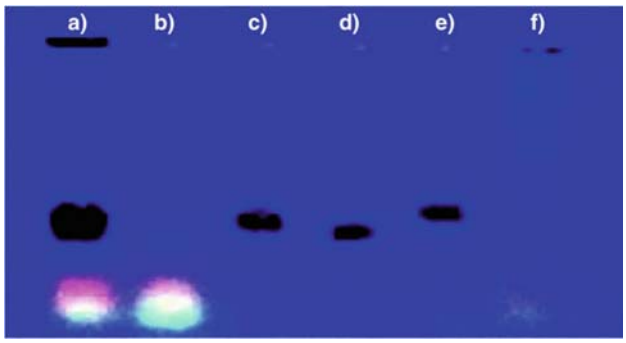

Figure 1.2. Images of the electrophoretic profile upon visible ultraviolet (UV) light illumination of 1 % agarose gel. Reprinted with permission from ref. 8. Copyright 2004 American Chemical Society.

During the last decade, several types of C-Dots have been emerging because of their interesting properties, the high number of their possible application in various fields and their easy-fast production (**Figure 1.3**). At first, they were called ‘‘carbon quantum dots’’. However, the term quantum dot (QD) was assigned without accomplishing all the necessary requirements to be called like this.[9] QDs are usually referred to small semiconductor particles with quantum-confinement effect, which means that the size of the particles is less than the Bohr radius of the charge carrier; the charge (*i.e.*, electrons or exciton) in these particles is confined in spatial dimensions with quantized energy states.[10] Besides, the morphology of the structure of C-Dots could be; crystalline or amorphous, and the shape; spherical or plane. There are several properties that can be studied in order to make a clear classification of C-Dots (**Figure 1.3**).[11] Nevertheless, some researchers call generally these nanomaterials as “C-Dots” in order to avoid misunderstandings. **Figure 1.3** reports the types of C-Dots that scientists are considering nowadays: graphene quantum dots (GQDs), carbon quantum dots (CQDs), polymer carbon dots (PCDs) and carbon nanodots (CNDs). In the next section of this chapter, the different types of C-Dots will be described in detail with a special emphasis on their differences, as for example their photoluminescence mechanism.

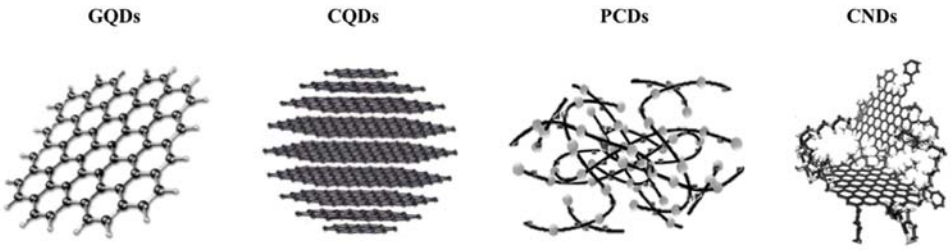

Figure 1.3. Classification of fluorescent carbon nanoparticles, C-Dots.

1.1.1. Graphene Quantum Dots

Graphene quantum dots (GQDs) or graphene quantum discs do not present spherical shapes. Typically, they are based on graphene sheets (3-10 layers) with lateral dimensions in the range of 2-20 nm. GQDs present the whole pack of unique properties of C-Dots, such as chemical inertness, high water solubility, low toxicity, tunable photoluminescence, and high photostability, among the others.[12] Moreover, GQDs exhibit quantum confinement, edge effects, carboxylic acids at the edges, and high surface area. As compared to the semiconductor quantum dots, they are non-toxic.

Besides the properties commented above, one of the most important and common feature for carbon nanoparticles showing quantum-confinement effect is the photoluminescence (PL) mechanism (*i.e.* GQDs and CQDs). Although it is still matter of debate, generally two mechanisms are accepted: one related to size-dependent fluorescence from the quantum-confinement of the core, and the other from the surface (*e.g.* groups or surface defects).[12,13,14]

1.1.2. Carbon Quantum Dots

In 2006 Sun *et al.*,[15] proposed the name carbon quantum dots (CQDs) reporting a post-synthetic route to enhance their emission *via* surface passivation. CQDs are quasi-spherical nanoparticles, in contrast as GQDs. The fluorescent nanoparticles, CQDs are formed by a crystalline core of a mixture of sp^2 and sp^3 carbon atoms with quasi-spherical shape. Generally, they present sizes below 10 nm, high chemical stability, strong PL with tunable excitation and emission, low toxicity and biocompatibility. Usually, CQDs have many carboxylic acid groups onto their surface, which impart them not only excellent water solubility, but also the possibility of post-synthetic surface functionalization. Moreover, they present quantum confinement as GQDs, this is the main feature to differentiate them among the others. Although, they can be considered as a non-toxic alternative for semiconductor, their usually low QYs strongly limit their real applications.

1.1.3. Carbon NanoDots

C-Dots usually composed of spherical nanoparticles without crystal lattices are principally named carbon nanodots (CNDs). CNDs present the same properties of the aforementioned carbon nanoparticles: low toxicity, biocompatibility, chemical inertness, strong PL with tunable emission and easy to be functionalized with organic molecules, biomolecules or even nanoparticles, thanks to the functional groups that are present on the CNDs surface, such as acids and amines. Finally, one of the most important feature that is different between the several kinds of C-Dots is their emission mechanism of photoluminescence. On one hand, they all presented strong fluorescence with excitation wavelength dependence. On the other hand, the emission of CNDs could be attributed to the large heterogeneity in functional groups onto their surface, in all cases they always present emission PL properties without the presence of a fluorophore.[19]

1.1.4. Polymer Carbon Dots

C-Dots principally composed of a polymer structure rather than a graphitic one are usually named polymer carbon dots (PCDs) or polymer dots. PCDs present the structure of both C-Dots and non-conjugated polymers. The most important feature to distinguish this kind of C-Dots to the others is the carbonization degree, which is the lowest of the carbon family.[16]

The typical model to distinguish PCDs from CNDs was studied by Li and co-workers,[17] and was based on the pyrolysis treatment of citric acid and ethylenediamine. In this work, the authors studied the synthesis of the dots modifying three parameters: the amount of the starting materials, the pH and the temperature. Afterwards, they analyzed all the products in terms of absorbance, QY and λ_{ex} dependence. Especially the temperature was identified as an important factor: by using low temperatures (100-200 ºC) they obtained PCDs and by using high temperatures (200-300 ºC) they obtained CNDs (**Figure 1.4**).[18]

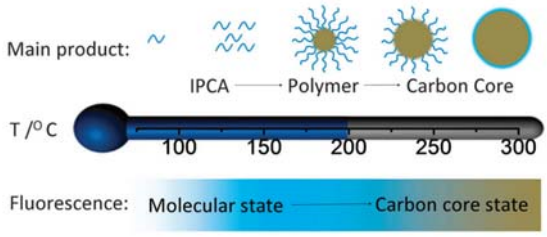

Figure 1.4. Scheme of C-Dots obtained at different reaction temperature. Reprinted with permission from ref. 16. Copyright 2015 Royal Society of Chemistry.

1.2. Preparation of C-Dots

Since their first preparation *via* arc-discharged in 2004,[8] the production of C-Dots grew-up exponential. Nowadays, they can be synthesized *via* several techniques classified in two main groups: top-down and bottom-up methods (**Figure 1.5**). Especially green, easy, low-cost and large-scale approach are attracting attention. In **Figure 1.5**, a schematic representation of the formation of C-Dots *via* the two main methodologies is reported, together with the most common starting materials.

In the following paragraphs, the general production of C-Dots it is described, with a special mention to CNDs that were used in this thesis.

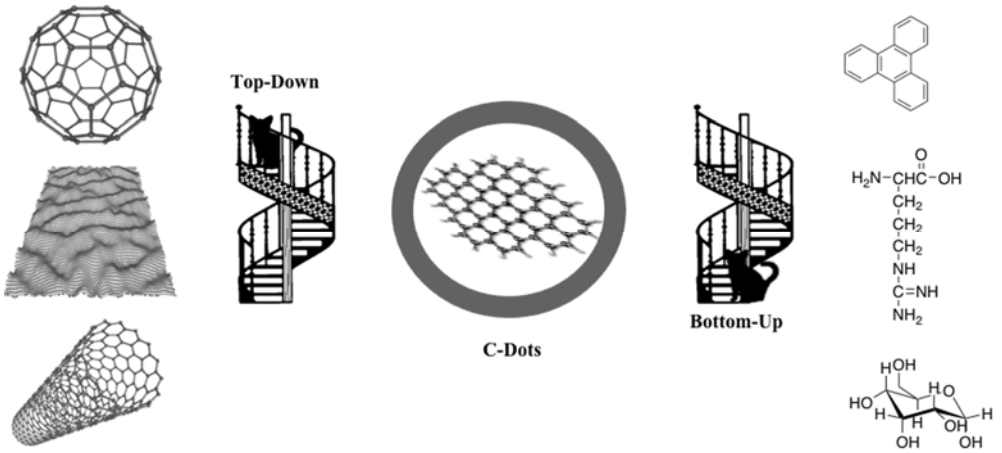

Figure 1.5. Schematic representation of the formation of C-Dots *via* top-down and bottom-up methods.

1.2.1. *Top-down* methods

Top-down approaches consist of chemical, electrochemical and physical treatments of carbon structures, such as graphite or carbon nanotubes. These techniques can be especially being used for the large-scale production of CNDs.

1.2.1.1. Arc-discharge

Typically, arc-discharge consists in two graphite rods as electrodes with a small separation between the anode and the cathode. A direct (D.C) or alternate (A.C) current arc voltage is applied through the electrodes in low pressures of Argon or Helium atmosphere and high temperatures (**Figure 1.6**). After the current is applied, the nanomaterial is obtained by its condensation on the cathode. The quantity and quality obtained of C-Dots depend on several parameters, such as pressure, temperature and current. This technique was the first approach described to obtain C-Dots (see section; 1.2 Preparation of C-Dots) and single-walled carbon nanotubes (SWCNTs).[8,4]

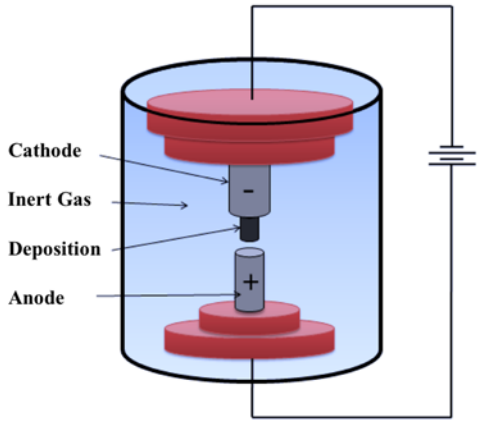

Figure 1.6. Schematic representation of the arc-discharge technique

1.2.1.2. Laser ablation

Laser ablation consists in a process where a laser beam, with a particular excitation wavelength, is focused on a sample surface, such as fullerene or CNTs, to remove material (*i.e.* ablation) from the irradiated zone in a specific time.[20] The most common laser used is based on the neodymium-doped yttrium aluminum garnet, Nd:$Y_3Al_5O_{12}$ (Nd:YAG), which typically emit light with a wavelength of 1064 nm. However, their wavelength can be tuned up to the ultraviolet.[21] Laser ablation procedures can be performed in solid state,[15] vapor phase or in solution.[22] Laser ablation techniques in solution are the less used, because of the effect that the physical parameters, such as laser wavelength and power impart on the size and optical properties. However, Reyes and co-workers reported the optimal conditions to synthesize CNDs by laser ablation in solution.[22] They have observed that the emission of the CNDs can be correlated with the excitation wavelength and the time of the laser irradiation process, by investigating the following wavelengths and times of irradiation: 1064, 532, and 355 nm for 150, 300, 600, and 900 s. TEM images revealed that the smallest CNDs were obtained at 355 nm and. It was observed that the PL emission depend on the time of irradiation since it was decreasing by increasing the irradiation time. In **Figure 1.7** is reported a schematic representation of the experimental design for the preparation of the C-Dots by using laser ablation in solution.

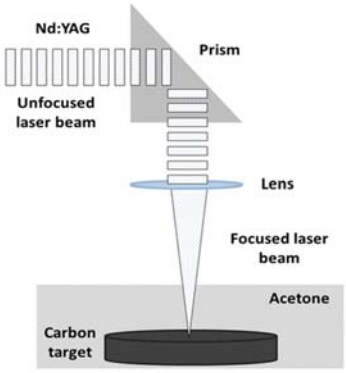

Figure 1.7. The experimental setup used for the preparation of C-Dots by using laser ablation. Reprinted with permission from ref. 22. Copyright 2016 Springer.

1.2.1.3. Electrochemical oxidation

The preparation of CNDs *via* electrochemical oxidation take advantage of a simple and low-cost procedures. The most common electrode are based on graphite and platinum, while ionic liquids are the most used electrolytes.[17,18]

Liu and co-workers described the preparation of C-Dots by using a conventional three-electrode cell with a graphite working electrode, a platinum counter electrode and Ag/AgCl as the reference electrode (**Figure 1.8**). A mixture of alkaline alcohols (*e.g.* NaOH/EtOH) was used as electrolyte.[25] The as-prepared C-Dots solution presented a dark yellow color at room temperature and then tuned colorless at 4 ºC. This phenomenon was due to the oxygenation of surface species over the time. Moreover, the potential was found to affect the size with higher potential resulted in larger C-Dots.

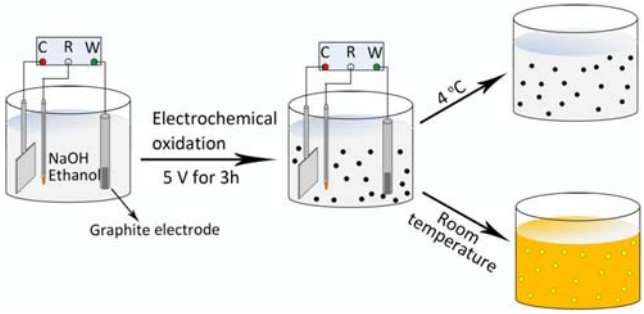

Figure 1.8. Schematic illustration for the production of C-Dots *via* electrochemical oxidation. Reprinted with permission from ref. 25. Copyright 2016 Royal Society of Chemistry.

1.2.1.4. Chemical oxidation

The most common starting materials used for the formation of fluorescent carbon nanoparticles *via* chemical oxidation are natural carbon sources or side products generated in reactions or processes that involve carbon, such as carbon soot. The use of strong acids, such as nitric acid, is required in order to carried out the redox process.[26,23] *Via* chemical oxidation of Chinese ink, Jiang and colleagues reported the large-scale preparation of C-Dots.[27] More than 100 g of oxidized C-Dots doped with N, S, and Se by an *in situ* doping were prepared in one step (**Figure 1.9**).

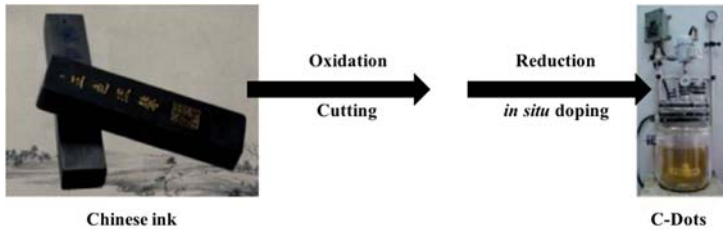

Figure 1.9. A schematic diagram of the preparation of C-dots by chemical oxidation. Adapted with permission from ref. 27. Copyright 2014 Royal Society of Chemistry.

1.2.1.5. Ultrasonic synthesis

During ultrasonication synthesis, ultrasonic waves or sound energy are applied on the starting precursors in solution with frequencies of (>20 kHz), these ultrasonic waves can cut macroscopic carbon nanomaterials into small pieces. In consequence, this process homogenizes and reduces the small particles in to the liquid and therefore, improves the uniformity and stability of the samples. The use of ultrasonic synthesis for the production of nanomaterials is a very powerful technique due to the high quality and quantity of the materials obtained. For instance, Kang and co-workers have produced carbon nanoparticles with excellent photoluminescent properties, *via* one-step ultrasonic synthesis.[28] They have treated for 4 h glucose in an ultrasonicator and the as-prepared dots presented an emission photoluminescent spectra up to the near infrared (NIR). Besides, they claimed that their carbon nanoparticles presented excellent up-conversion fluorescent properties.

1.2.2. *Bottom-up* methods

Bottom-up approaches consist on the preparation of C-Dots from small organic precursors. The majority of the processes used for the production of C-Dots are based on *bottom-up* techniques. However, generally these techniques cannot be easily applied for a large-scale production.

1.2.2.1. Microwave synthesis

Microwave-based synthesis is a very popular approach in material chemistry because it offers easy-fast and low-cost production. However, the production of C-Dots by microwave synthesis can result in a material with relatively low quantum yield (QY).[29] The process can be hydrothermal or solvothermal and small organic molecules are the most used starting materials. It is well known that heating small organic molecules above their melting points leads to condensation, nucleation and finally the formation of C-Dots; all of this in one-step in a microwave reactor.

Recently, Choi and colleagues reported the production of amphiphilic C-Dots *via* microwave-assisted synthesis.[30] They used as starting materials citric acid and 4,7,10-trioxa-1,13-tridecanediamine (TTDDA) as surface passivation agent. They performed a short synthesis in 5 min in the household microwave oven and they obtained C-Dots with a QY of 29 % and amphiphilic solubility in several solvents. Moreover, Arcudi and co-workers described the synthesis of nitrogen doped CNDs in a microwave reactor in 3 min.[31] The resulting dots were purified by size exclusion chromatography and finally they presented sizes from 1.24 nm to 2.65 nm.

1.2.2.2. Thermal decomposition

The possible use of low-cost starting materials and the mild conditions offered make this technique a good candidate for an environmentally-friendly process. Moreover, this kind of approach can be performed without the use of solvents

Reisner and co-workers described the synthesis of C-Dots starting from the thermal decomposition of citric acid under air at 180 ºC for 40 h.[32] Enough time of heating was given to complete the reaction and then the resulting dissolution in water was neutralized to produce a concentrated brown solution of sodium carboxylate-terminated C-Dots. Their dots presented a spherical shape with an average size of 6.8 $\pm$ 2.3 nm.

1.2.2.3. Hydrothermal treatment

The procedure consists on a water solution of small organic molecules or natural compounds, such as waste peels seal in a reactor at high temperatures and pressures.[33] Lau and colleagues synthesized fluorescent carbon nanoparticles in one-step by using glucose as carbon source in a conventional microwave oven.[34] The as-prepared C-Dots have shown a QY from 7 to 11 %. Besides, they claimed that the QY is related to the reaction time. For instance, from 1 min to 6 min the QY was increased from 7 % to 11 %. This phenomenon was due to the evolution on the dots along the time in the hydrothermal treatment.

1.3. Characterization of C-Dots

Reliable characterization techniques are extremely important to study the chemical and structural characteristics of carbon nanomaterials and to recognize their possible modifications.[35] The most common characterization techniques for CNDs, which were also used for this doctoral thesis were ultraviolet-visible (UV-Vis), fluorescence (FL), Fourier transform infrared (FTIR) spectroscopies, nuclear magnetic resonance (NMR), thermogravimetric analysis (TGA), transmission electron microscopy (TEM), atomic force microscopy (AFM), X-ray photoelectron spectroscopy (XPS), dynamic light scattering (DLS), zeta potential (ς-potential), matrix-assisted laser desorption ionization time-of-flight (MALDI-TOF) and Kaiser test (KT). In the following paragraphs, it will be described some of the major instrumental methods (**Figure 1.10**).

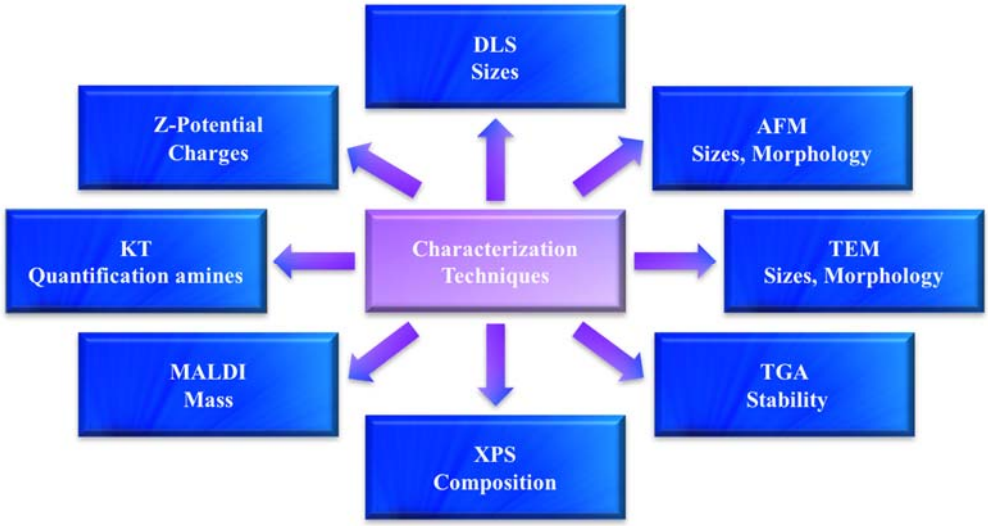

Figure 1.10. Summary of the principles techniques for the characterization of C-Dots.

1.3.1. Thermogravimetric analysis

Thermogravimetric analysis or thermal gravimetric analysis (TGA) is an analytical technique used to determine the thermal stability of a material, the fraction of its components and impurities. It is based on recording the weight change as the temperature is increased on the sample, generally up to 800 ºC in inert atmosphere (N_2 or Ar) or in air for carbon nanomaterials.[36]

1.3.2. Transmission electron microscopy

Transmission electron microscopy (TEM) uses a high-energy electron beam (up to 300 kV) thus can penetrate several μm of a solid (**Figure 1.11**). When a crystalline solid is irradiated by a beam, the electrons are diffracted by the atomic planes into the

material, being possible to form a diffraction pattern of electron transmission,[37] as first demonstrated by Thomson in 1927.[38] Nevertheless, the electrons used for imaging can themselves cause damage and structural modification. In order to avoid this problem, the sample should be exposed to the electron beam for short periods. TEM provides direct images of atomic level (<1 nm). Thus, this technique gives morphological information, such as diameter and length. High-resolution TEM (HRTEM) can be used to observe the graphite lattice planes of the carbon core in CNDs, which are related to their crystalline nature.

1.3.3. Atomic force microscopy

Atomic force microscopy (AFM) generally consists in "feel" the surface of the sample with a sharp tip at the end of the cantilever (**Figure 1.11**). AFM measures the deflection of the cantilever tip caused by electrostatic and van der Waals interactions, as well as the attraction between atoms at the tip and the measured surface. Thus, AFM describes a three-dimensional image of the sample capable of providing information at any angle of its height, length, width or volume. Thanks to that, it is constructed a surface map of the topography of a sample with high resolution, with a range of work from 100 mm to the nanometer scale. In 1990 the instrument raised near-atomic resolution. Moreover, AFM is gaining tremendous importance due to its capability for imaging without causing appreciable damage onto the surfaces of the materials as TEM does. Usually, three types of modes are used for this technique, which are: the contact mode, non-contact and tapping mode.[35] In this thesis, tapping mode was used.

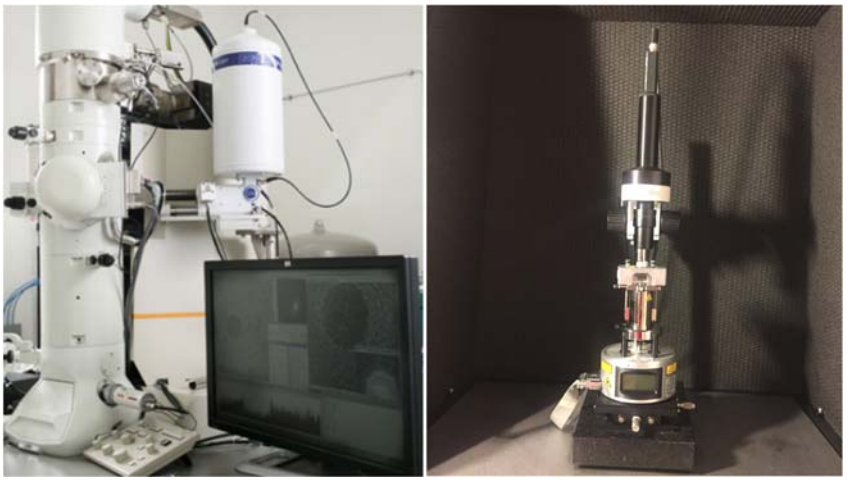

Figure 1.11. Digital images of TEM and AFM apparatus.

1.3.4. X-ray photoelectron spectroscopy

X-ray photoelectron spectroscopy (XPS) is the most widely technique used in material science, which allows to detect, quantify and define the elemental

composition of the material surface (**Figure 1.12**). The material is irradiated with X-rays, causing the emission of photoelectrons from the sample surface. Afterwards, a photodetector measures the intensity and the binding energy of the generated photoelectrons. Since each element has defined binding energies, XPS can be used in order to identify the element on the C-Dots surface and their chemical composition. Besides, semi-quantitative information about the elemental composition of carbon nanoparticles can be obtained with this technique.

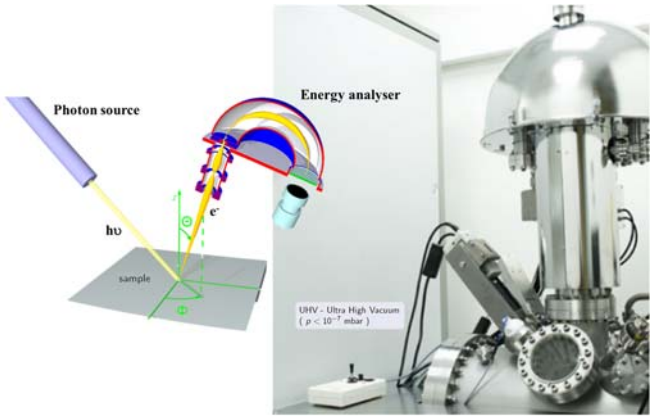

Figure 1.12. Schematic representation and digital image of the XPS technique.

1.3.5. Dynamic light scattering

Dynamic light scattering (DLS) is also known as photon correlation spectroscopy or quasi-elastic light scattering. It is one of the most used techniques to determine the physicochemical characteristics of nanomaterials, such as the hydrodynamic size, shape, and aggregation of the species. The samples are illuminated by a monochromatic laser and the scattering, depending on the Brownian motion, is measured by a detector. The Stokes-Einstein relation connects diffusion coefficient (Dh) measured by DLS from fluctuations with the velocity of the Brownian motion to particle size (**Equation 1.1**).[39]

Equation 1.1
$$D_h = \frac{K_B T}{3\pi\eta D_t}$$

Where D_h is the hydrodynamic diameter, K_B is the Boltzmann's constant, T is the temperature, η viscosity and D diffusion coefficient.

1.3.6. Zeta potential

The zeta potential (ς-potential) is generally used to study the behavior of solids in solutions, in particular the electrokinetic potential. Solids in solutions form a double layer or electrical double layer. Thus, ς-potential is the electric potential between the interfacial double layer the solid, which is generally measured by the velocity of the charged species towards the electrode in the presence of an external potential. The ς-

potential indicates the electrostatic repulsion between similarly charged particles in a dispersion. Nanoparticles with a zeta potential between −10 and +10 mV are considered neutral, +30 mV are considered strongly cationic and less than −30 mV strongly anionic.[39]

1.3.7. Matrix-assisted laser desorption

Matrix-assisted laser desorption ionization time-of-flight (MALDI-TOF) is a useful technique that allows to determine the molecular weight of nanoparticles. This technique is based on the irradiation, typically with a nitrogen laser, onto a stainless steel that contains the crystals of the mixture sample-matrix. The sample sublimate to a gas phase where ionization of the sample. Afterwards, the analyzer TOF, measures the time of flight of the ions since they are accelerated, by the source, until they arrived to the detector.[40]

1.3.8. Kaiser test

Kaiser test (KT) is commonly used in the chemistry of peptides. Nowadays is extend to the semi-quantitative analyses of primary amino groups present in nanomaterials. KT, which is based in the specific reaction between free primary amino groups and ninhydrin, which affords a product with a deep violet blue color, known as Ruhemann's purple (**Figure 1.13**). By measuring the intensity of the corresponding peak in UV-Vis spectrum, a semi-quantitative amount of amino groups can be calculated as follows (**Equation 1.2**).[41]

Equation 1.2

$$\mu mol/g = \frac{A_{570} \cdot V \cdot 10^6}{\varepsilon \cdot m}$$

Where A_{570} is the absorbance at 570 nm, V is the final volume in ml, ε is the absorptivity of the colorful compound at 570 nm and m is the exact mass of the analyzed materials in mg.

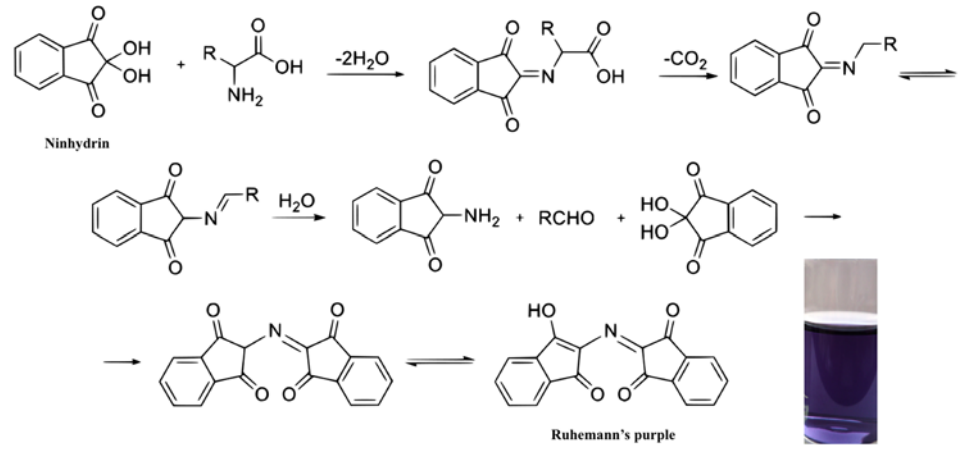

Figure 1.13. Reaction of ninhydrin with primary amines.

1.4. Properties of Carbon Dots

1.4.1. Composition and structure

C-Dots are quasi-spherical carbon nanoparticles with diameters between 2−10 nm. Furthermore, C-Dots can be amorphous or nanocrystals with sp^2 carbon clusters. In contrast to the other C-Dots, all kinds of GQDs have a graphitic structure. Principally, C-dots present carboxylic moieties at their surface, with a wide range of oxygen contents, depending on the experimental conditions used. Thus, impart excellent solubility in water and biocompatibility.[42] Moreover, they can be doping, a widely used approach to tune the PL properties. Several doping methods with various elements, such as N,[43] S,[44] and P,[44] have been reported to tune the properties of the dots.

1.4.2. Optical properties

1.4.2.1. Absorbance

C-Dots usually present a strong optical absorption in the UV region (260-320 nm) with a tail extending towards the visible range, which is attributed to the core and surface transitions states, such as n-π* which corresponds to the transition of C=O and π-π* due to the C=C transitions. However, depending on the production of the dots, their functional groups can be modified, therefore their optical absorption (**Figure 1.14**).[42,42,45]

1.4.2.2. Photoluminescence

The most important feature of C-Dots is the excitation-dependent photoluminescence (**Figure 1.14**). There is a controversy in the origin of this feature, scientifics proposed a different mechanism for each kind of C-Dots making clear a different between the C-Dots with quantum-confinement and the others.[42,45,46] Recently, Feldmann and colleagues have reported the formation of the internal structure and therefore the study of the optical properties of C-Dots. The dots were synthesized *via* hydrothermal reaction from citric acid and ethylenediamine variyng the time of reaction.[47] Feldmann found that the C-Dots grow within 30 minutes of the reaction and maintained the size for the rest of the synthesis. Moreover, they showed that early on mainly fluorescent molecules formed, similar in structure to citrazinic acid. Along the time, aromatic domains appeared, grow in size and leading to additional absorption and PL at longer wavelengths. Finally, they concluded that the elucidated mechanism of the formation of C-Dots showed that it is possible to control the optical properties of the emitters through modifications on the synthesis procedures, such as the time.

Several reports have showed that the fluorescence emissions of C-Dots are pH-dependent, due to the presence of functional groups, such as -OH or -COOH groups, onto the surface of the dots, the fluorescence of C-Dots solution is very sensitive to

pH.[48] Moreover, as compared to conventional organic or inorganic fluorophores, carbon dots present excellent photostability.[49]

The efficiency of a fluorescence process is evaluated with the QY. The QY of the C-Dots varies with the fabrication method and the surface passivation perform onto their surface.[50]

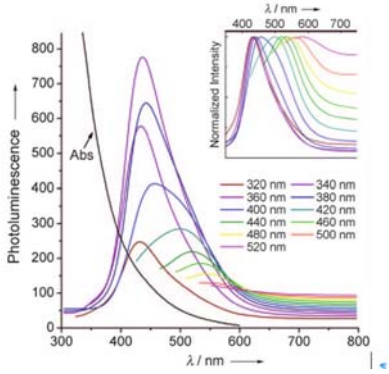

Figure 1.14. UV-Vis absorption and photoluminescence emission spectra of carbon dots surface-passivated with PEG1500N. Adapted with permission from ref. 48. Copyright 2009 John Wiley and Sons.

1.4.2.3. Up-Conversion photoluminescence

Nanoparticles with up-conversion photoluminescence (UCPL) properties absorb light in the infrared (IR) or near infrared (NIR) and emit light in the visible range (*i.e.* the emission wavelength is shorter than the excitation wavelength).[51] In 2007 Cao from Clemson university reported the first C-Dots with UCPL properties.[52] From that date several dots with UCPL features were emerging; however, the origin is not clear yet. Normal fluorescent spectrophotometer with lamps of xenon without the use of filters presented the second-order diffraction light, and this was understood as UCPL properties.[53] Some publications have reported C-Dots with up-conversion phenomena, however those C-Dots presented a normal photoluminescence excited by the second-order diffraction light (λ/2) coming from the excitation monochromator.

Today, UCPL particles are currently used for their use in *in vivo* bioapplications, due to their excitation in the NIR range where light absorption and scattering from biological tissues is minimum.

1.4.3. Electrochemical properties

The electrochemical properties of carbon dots could vary depending on the complex interplay of the material core, functional groups and heteroatoms, for that reason each nanomaterial has a specific application.[54] In order to present efficient electron transfer properties, carbon dots should present a large specific surface area and abundant

edges sites, such as graphene quantum dots.[55] Jing Zhao *et al.* described in 2011 a platform based on carbon dots for electrochemical biosensors, they could identify different molecules, complementary DNA or proteins.[56]

1.4.4. Toxicity

1.4.4.1. *In vitro*

The investigation of the cytotoxicity of C-Dots have gained tremendous attention in the last decade in order to use them for the possible wide range of bioapplications. Cytotoxicity studies are based on colorimetric techniques, such as 3-(4,5-dimethylthiazol-2-yl)-2,5 diphenyltetrazolium bromide assay (MTT) that can be used to test the cell viability. All the studies so far reported show that C-Dots are non-toxic up to high concentrations.[57]

1.4.4.2. *In vivo*

Apart from *in vitro* investigation, also the *in vivo* toxicity activity of C-Dots was investigated.[45,46] The reported results show the non-toxicity of the dose used of C-Dots. For instance, Yang and co-workers used CD-1 mice for the toxicity activity *in vivo*. The mice were exposed to three different dosages of C-Dots, 8, 40 and 0 mg (*i.e.* C-Dots-equivalent/kg body weight). The authors claimed that the doses applied to the mice did not show any significant toxic effects even at the 40 mg dose.[57]

1.5. Applications of Carbon Dots

In the following sections, it is presented an overview mainly on the C-Dots bio-related applications and briefly on their use in chemical sensing, photocatalysis, electrocatalysis and optoelectronics.

Among all the applications, chemical sensing is one of the most studied application of fluorescent carbon dots.[46] It is based on the change in the dots fluorescence (intensity and/or emission wavelength) due to the presence of specific analytes.[113,114] In addition, their use in photocatalysis have won a position as greener alternative in organic synthesis. This was motivated for the use of the sunlight, which is the major and inexhaustible source of energy in the world. C-Dots offer an excellent potential for their use as an alternative photocatalysts. They show superiority in chemical stability, water solubility, excellent electron donors and acceptors, and low toxicity in comparison with the most common photocatalysts used, such as ZnO, TiO_2 and CdS. The photocatalytic activity of C-Dots can be effectively modulated by doping the dots and modifying their surface groups.[115,32] Furthermore, It was reported that doped nitrogen carbon nanomaterials improve their electrocatalytic efficiency.[116]

Moreover, it is well known that semiconductor QDs are increasingly used for light emitting diodes (LEDs) fabrication. The technology for lighting and displays based on QDs is now approaching industrial applications. However, fluorescent carbon dots

have started to emerge as a non-toxic alternative to replace phosphors in white light emitting diodes (WLEDs),[118,119] which normally are formed by toxic elements, such as cadmium. Among all the examples existing in the literature, optoelectronic applications are in its infancy, and the efficiency of the dots is expected to be further improved.

C-Dots are good candidates for several applications, such as chemical sensing, photocatalysis, electrocatalysis and optoelectronics as was commented above. Among them, their bioapplications are attracting considerable attention and represent the main focus of this dissertation.

First of all, *why C-Dots appear as more promising and superior than other materials/nanoparticles for bio-related applications than other materials/nanoparticles?*

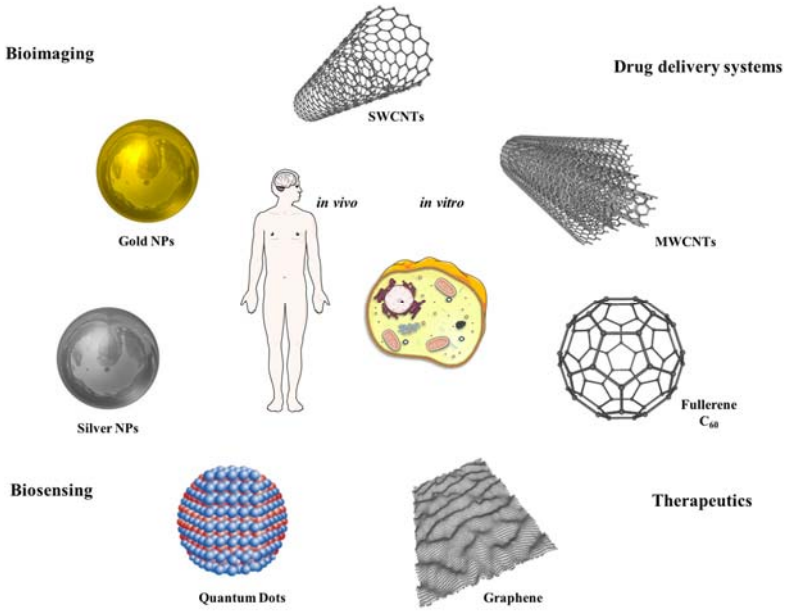

Figure 1.15. The most representative applications of carbon nanomaterials and common nanoparticles.

Their higher non-toxicity and biocompatibility in comparison with other nanomaterials, such as inorganic quantum dots (QDs), gold and silver nanoparticles, graphene or CNTs, make C-Dots promising materials. Despite the great interest in developing biomedical applications with QDs, their potential toxicity limit further developments.[60] Moreover, gold nanoparticles around 45 nm were found toxic with concentration of 10 $\mu g \cdot mL^{-1}$,[61] although these results are not in agreement with others and, thus, more research is needed.[62] Similarly, silver nanoparticles were found to be toxic.[63] Graphene, CNTs or even fullerenes have been largely investigated for

bioapplications, even though they present low solubility in aqueous solution. Therefore, many non-covalent or covalent modifications have been exploited to enhanced their solubility or dispersion in aqueous solvent.[64]

Consequently, the majority of carbon nanomaterials and nanoparticles that have been studied for bioapplications, present toxicity or solubility issues and their chemical modification is an essential step to improve their performance.

On one hand, QDs have been successfully used for bioimaging due to their high quantum yield and narrow emission color purity without photobleaching.[65] However, the efficiency of the cellular uptake is generally low. Thus, Hasegawa *et al.* used functionalized $CHPNH_2$-QDs complexes, which were uniformly internalized into the cells for long-term live cell imaging. The interaction of QDs with cells was successfully controlled by the content of amino groups present in the linker.[66] On the other hand, gold nanoparticles can be easily visualized inside the cells by two-photon absorption from a near-infrared ultrafast laser.[67]

Turning to carbon nanomaterials, NIR excitation for raman imaging is one of the possible advantage in using CNTs, since minimize the autofluorescence of biological species and allow to decrease the photobleaching of CNTs.[68] Particularly promising are hybrid materials, such as the ones graphene based. For instance, Zhang and co-workers grew iron oxide nanoparticles on the surface of graphene oxide (GO) in order to create a hybrid materials to use as contrast agents in MRI.[69] Another common strategy is the functionalization of carbon nanomaterials to make them water soluble in order to facilitate their use for bioapplications. Thus, in our group CNTs were functionalized *via* 1,3-dipolar cycloaddition reaction onto the external surface of the nanotube with N-protected amino acids, in order to obtain water soluble CNTs.[70] In another example, Chen *et al.* fabricated nanofibers encapsulating fullerene functionalized with TEGs to *in vitro* biological imaging.[71]

Drug delivery systems based on nanomaterials are enormously growing nowadays. Several drugs such as methotrexate,[72] doxorrubicin[73] among others were attached onto the surface of gold nanoparticles. Moreover, the surface of the gold nanoparticles can be easily modified by using polyethylene glycol (PEG) and the amphiphilic characteristics of the polymer enhance the stability of the material in physiological conditions.[74] Likewise, semiconductor quantum dots can be modified with biocompatible materials or polymer, such as PEG, to promote their water solubility and biocompatibility. Zhang *et al.* reported a co-loaded system based on QDs and paclitaxel in combination with lipid systems. The lipid matrix provided the protection of PTX and QDs until the destined place inside the cells was reached.[75]

Carbon nanotubes have demonstrated superior drug loading ability than other nanoparticle-based drug delivery systems.[76] However, CNTs can show different levels of toxicity depending on their production method, composition and the applied dosage.[77] Drug delivery systems based on graphene has been increasingly grow in recent years, due to its high specific surface area.[78,79] Nonetheless, several C_{60} derivatives, which are water soluble, were used as biomedical nanocarriers; for example paclitaxel,[80] however the efficiency of the system was worse than the drug alone.

Nowadays, the development of new systems to treat brain diseases is a hot topic. Inorganic materials such as gold, silver or silica nanoparticles and inorganic quantum dots have been extensively studied for drug delivery to the brain.[81] However, they could present some disadvantages since they could be not degraded or present undesired toxicity. Moreover, CNTs, graphene and fullerenes may lead to lipid peroxidation and oxygen radical formation into the brain.[82]

Overall, from a critical point of view C-Dots may provide advantages for bioapplications over the aforementioned materials due to the unique properties that C-Dots present.

1.5.1. Bioapplications

Fluorescent carbon nanoparticles seems to play an important role for biomedical applications, such as biosensing,[83] cellular imaging,[84] drug delivery,[85] and theranostics due to their fascinating features, such as water solubility, low toxicity,[59,86] biocompatibility, ease of functionalization, chemical stability, and unique photoluminescent properties, *e.g.*, excitation-dependent fluorescence emission that allow to minimize the biological background by increasing the Stokes shift.[87]

1.5.1.1. Bioimaging

Organic, inorganic fluorophores and QDs have been the most studied agents for bioimaging so far, both *in vitro* and *in vivo*.[88,89] However, due to their possible hazardous nature and low solubility in aqueous media, C-Dots are emerging as an alternative for bioimaging applications.

Sun and co-workers reported for the first time the use of C-Dots for bioimaging **(Figure 1.16)**.[52] They demonstrated the great potential for PEG_{1500N} passivated C-Dots to be internalized into human breast cancer (MCF-7) cells through two-photon luminescence microscopy. The dots exhibited bright luminescence in both the cell membrane and the cytoplasm regions.

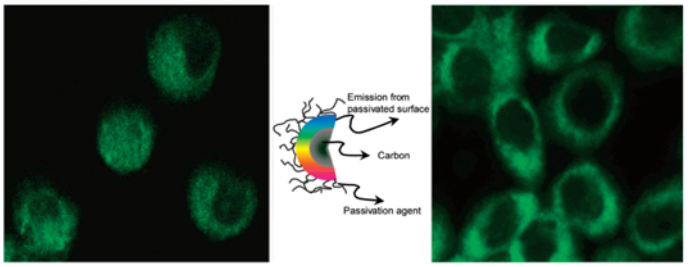

Figure 1.16. Two-photon luminescence image of MCF-7 after incubation for 2 h with C-Dots. Adapted with permission from ref. 52. Copyright 2007 American Chemical Society.

Afterwards, several intracellular imaging of the dots in different type of cells have been reported, such as cervix cancer cells (HeLa),[90] human liver cancer cells (HepG2),[90] and human lung cancer cells (A-549).[91] In all these cases, C-Dots were found mostly in the cytoplasm and cell membrane and they did not reach the nucleus. In order to target the nucleus, Yang and co-workers modified the surface of the dots with a nuclear localization signal peptide.[92]

The emission of CNDs towards the NIR region, would have a great impact for the *in vivo* fluorescence imaging. Yang's group was the first to explore CNDs as contrast agents in mice.[58] They modified CNDs with PEG_{1500N} to inject them subcutaneously into the mice observing a good emissions (**Figure 1.17**).

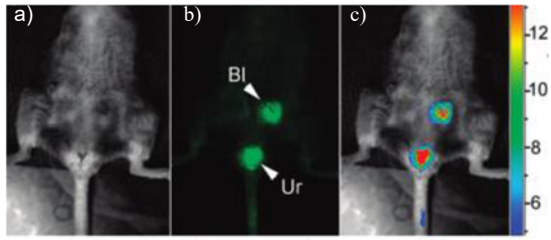

Figure 1.17. Intravenous injection of C-Dots: (a) bright field, (b) as-detected fluorescence (Bl, bladder; Ur, urine), and (c) color-coded images. Adapted with permission from ref. 58. Copyright 2009 American Chemical Society.

1.5.1.2. Drug delivery

Ideal nanoparticles for drug delivery are generally <100 nm in size, stables and they should present high drugs loadings or encapsulation, together with good biocompatibility and low toxicity.[93,94] The most widely investigated drug delivery systems (DDSs) are based on silica,[95] gold or silver nanoparticles,[96,97] semiconductor quantum dots,[98] dendrimers,[99] carbon nanotubes,[100] and liposomes.[101] However, their potential toxicity limits their use in clinical therapy. Therefore, CNDs could be a new and suitable alternative for improved DDSs, by enhancing the water solubility of the drug, preventing severe side effects of many hydrophobic anticancer drugs used in chemotherapy, and efficiently delivering the drug.[102,85]

Recently, Zhang's group described amphiphilic C-Dots (ACD) as a versatile vector for nucleic acid and drug.[103] The dots served as multifunctional platform for drug/gene delivery and bioimaging applications. This PEI 600 derived C-Dots presented micelles-like structures in water after the hydrophobic modification. Then, doxorubicin (DOX) was loaded by hydrophobic interactions onto the ACD. Confocal laser microscopy confirmed a high drug content and encapsulation efficiency of this system (**Figure 1.18**).

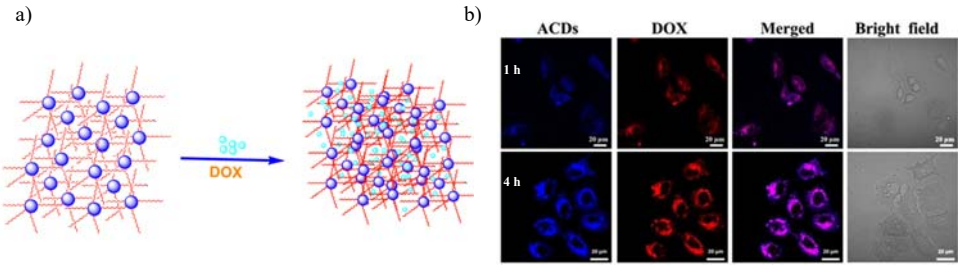

Figure 1.18. a) Schematic illustration of DOX@ACD. b) Confocal laser scanning microscopy (CLSM) of A-549 cells treated with DOX@ACD. Adapted with permission from ref. 103. Copyright 2017 Royal Society of Chemistry.

1.5.1.2.1. Drug delivery systems to target the brain

Within drug delivery systems, the ones that target the brain are the most challenging. First of all, they have to cross the blood brain barrier (BBB). The BBB is a highly selective membrane that separates the circulating blood from the brain. Furthermore, it prevents selectively the entrance into the brain of toxins and circulating neurotransmitters.[104]

Recently, it was reported for the first time the use of C-Dots for the Alzheimer disease treatment. For such kind of purpose, the BBB must be crossed.[105] Han *et al.* delivered C-dots across the BBB in a zebrafish model using human transferrin. The synthesized C-dots were found to inhibit the β-secretases enzyme. These results demonstrate the potential application of C-Dots as new agents for AD treatment.

1.5.1.3. Biosensing

Biosensing plays a crucial role to detect essential changes in living cells, such as differences of pH, temperature and the presence of hazardous concentrations of biological species for an efficient diagnosis. Stable nanomaterials as CNDs with unique PL and electrochemical properties can act as a versatile platform in this field.[45]

CNDs were reported as PL sensor for the detection of hazardous ions for the human health, such as Hg^{2+} and Pb^{2+}, sugar, proteins, among other biomolecules, in large varieties of samples, including body fluids, food samples or cell cultures. Their employment is based on a PL turn-on and turn-off mechanism through the surface modifications from species able to produce fluorescence resonance energy transfer.[106,107,108] Moreover, CNDs can detect differences on the cellular pH. Zhang and co-workers developed a pH sensor using C-Dots modified with fluorescein isothiocyanate.[109] Furthermore, CNDs were efficiently used in immunoassays as fluorescent labels,[110] or for the detection of drugs, such as Norfloxacin as it was reported by Yang.[111] In 2011 Zeng *et al.* reported the detection of DNA with C-Dots.[112] They found that the methylene blue (MB) could bind the dots quenching their

emission that was restored in the presence of DNA because of the specific MB-DNA interaction (**Figure 1.19**).

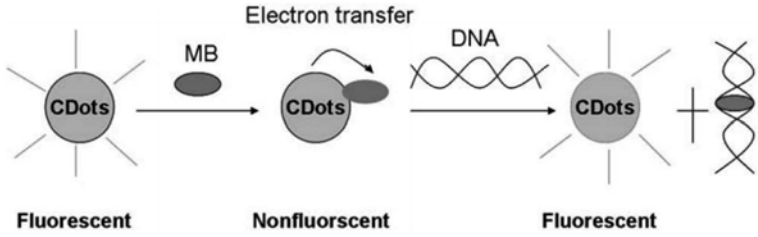

Figure 1.19. Schematic representation of C-Dots biosensors for the DNA detection. Reprinted with permission from ref. 112. Copyright 2011 Japan Society for Analytical Chemistry.

1.5. Impact of Carbon Dots

Fluorescent carbon dots have gained tremendous attention in the last decade. Owing to that, thousands of papers have appeared exponentially, such as new synthetic methods from a variety of starting materials and for diverse applications.

In **Figure 1.20** it is reported the number of publications from the web of knowledge, since the discovery of fluorescent nanoparticles in 2004 up to 2016. It can be observed an exponential growth along the time with a significant increase in the last 5 years.

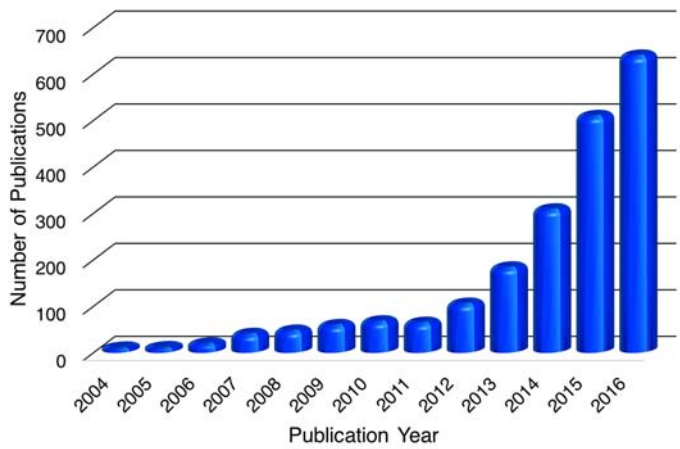

Figure 1.20. Number of C-Dots publications from the web of knowledge.

Among the thousand publications that can be found in literature (**Figure 1.21**), it can be especially observed an increased recent attention in exploring their use various application fields. However, the key challenge for most of these applications is to improve the photoluminescence properties and quantum yield of carbon dots. A lot

of efforts need to be done in order to propose simple and reliable synthesis of dots with defined properties for *ad hoc* applications.

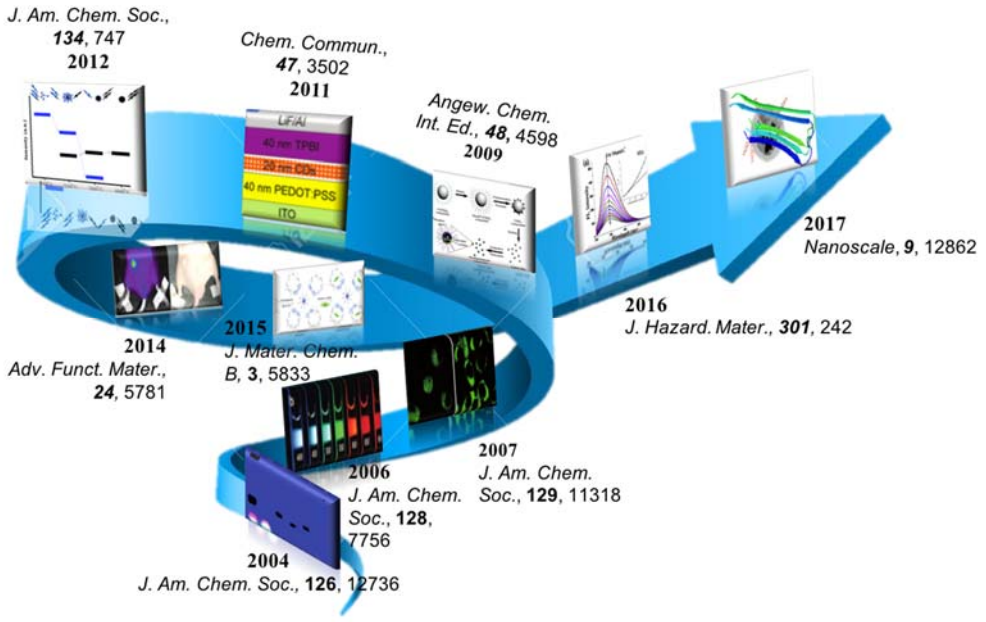

Figure 1.21. Timeline of the major milestones in the field of C-Dots.

1.6. Overview of the dissertation

This thesis tries to contribute and understand the surface modification of C-Dots and their impact towards biomedical applications. The work has been divided into three main chapters, as presented below.

Chapter 2 demonstrates the synthesis of highly fluorescent and water-soluble nitrogen-doped CNDs, without the need of sophisticated equipment and/or additional surface passivation.

Chapter 3 showcases our efforts towards the modification of CNDs for preparing hybrid materials for diverse bioapplications.

Chapter 4 presents the *in vitro* bioapplications of the materials describe in chapter 3 as drug delivery systems, bioimaging agents and nanocarriers. Moreover, the effect of a protein corona around CNDs on their cellular uptake it is studied, since it is a prerequisite for their successful use for such applications.

CHAPTER 2

Synthesis of Carbon NanoDots

CHAPTER 2

Synthesis of Carbon NanoDots

"Chemistry, unlike other sciences, sprang originally from delusions and superstitions, and was at its commencement exactly on a par with magic and astrology" Dr. Thomas Thomson

2.1. Introduction

The synthesis of novel CNDs has gained tremendous attention in the last decade, due to their excellent properties discussed along the Chapter 1. In particular, the use of green chemistry methods is of particular interest.[120] They have been preferred over the traditional approaches, in order to minimize the use and/or the production of hazardous substances. Moreover, a great deal of attention has been paid to cost and time-effective synthetic processes in line with a sustainable synthesis. This could be achieved using natural sources, such as wood, sucrose or low-cost starting materials for the synthesis of the dots, together with facile purification procedures.

Amongst the different types of CNDs, nitrogen-doped CNDs (NCNDs) have usually higher quantum yield (QY) than non-doped CNDS (*i.e.* improvement of the optical properties), so that they are the most commonly used recently.[121,122] Moreover, it was demonstrated that NCNDs have better performance for bioimaging because of stronger resistance to photobleaching as compared to undoped CNDs.[123] Various nitrogen-rich molecules, such as diethylenetriamine (DETA),[124] ethylenediamine (EDA),[16] urea,[125] and tris(hydroxymethyl)methyl aminomethane (Tris)[126] have been used to as precursors for NCNDs. A common synthetic approach is based on hydrothermal treatment, which usually requires several hours and high reaction temperatures and/or pressures. Microwave-assisted hydrothermal method is nowadays preferred because it

offers shorter reaction time, less energy consumption, easy operation, and environmental friendliness.[127,128]

Purification techniques are an essential step of the synthetic process of nanomaterials and dialysis is one of the most used techniques. It offers a simple and effective method for the purification of narrowly distributed nanomaterials.[129] It is based on a diffusion process, *i.e.* substances move from an area of high concentration to an area of low concentration, maintaining the equilibrium in both sides.

Characterization is the last fundamental step by which the structure and the properties of the prepared materials are measured and studied. The most used techniques for the characterization of C-Dots are fully described along the Chapter 1.

2.2. Aim of the work

The main aim of this chapter is obtaining highly water soluble CNDs with excellent photoluminescence properties and several functional groups on their surface that can be used for their post-synthetic functionalization, as it is discussed in Chapter 3. For this propose, low-cost precursors will be used. Moreover, the prepared CNDs must show non-toxicity and biocompatibility for the desired bioapplications that will be discussed in Chapter 4.

In particular, a microwave-assisted hydrothermal synthesis of NCNDs that has been already developed in our research group will be used.[31] Indeed, as it was discussed in the introduction of this dissertation (Chapter 1), microwave-assisted synthesis are ideal methods to prepare high-quality CNDs in an easy-fast way. After their purification, the characterization of the as-prepared NCNDs, by employing UV-Vis, FL, FT-IR, DLS, AFM, TEM and XPS techniques will be presented.

2.3. Results and discussion

2.3.1. Synthesis of CNDs

Highly fluorescent water-soluble NCNDs were synthesized by one-step microwave-assisted hydrothermal synthesis using L-arginine (Arg) and ethylenediamine (EDA) as both carbon and nitrogen sources (**Figure 2.1**).[31] It is already reported that the use of amines coming from EDA give some of the NCNDs highest fluorescence quantum yield.[130,131] Amino acids were used due to their abundance, inexpensive, biocompatible and ecofriendly nature. They possess both amino and carboxyl groups and may serve as an ideal molecular precursor for CNDs Moreover, microwave-assisted methods appear to be a more feasible synthetic technique because they are simple, fast and energy efficient. The as-prepared dots are highly soluble in water and methanol, according to their hydrophilic nature.

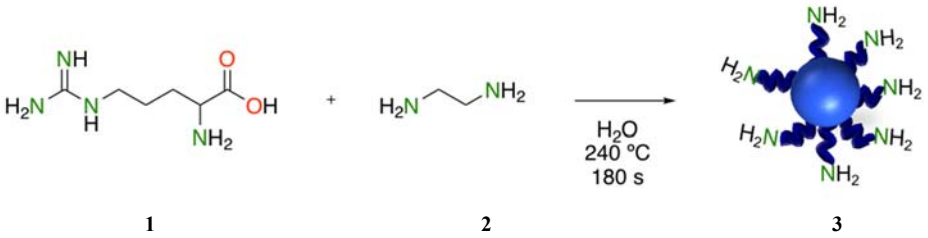

Figure 2.1. Microwave-assisted hydrothermal synthesis of CNDs by using arginine and ethylenendiamine as precursors.

Processes of condensation and nucleation finally result in the formation of the CNDs. During the synthesis, the solution changed color from transparent to dark brown, as a result of the NCNDs formation (**Figure 2.2**).

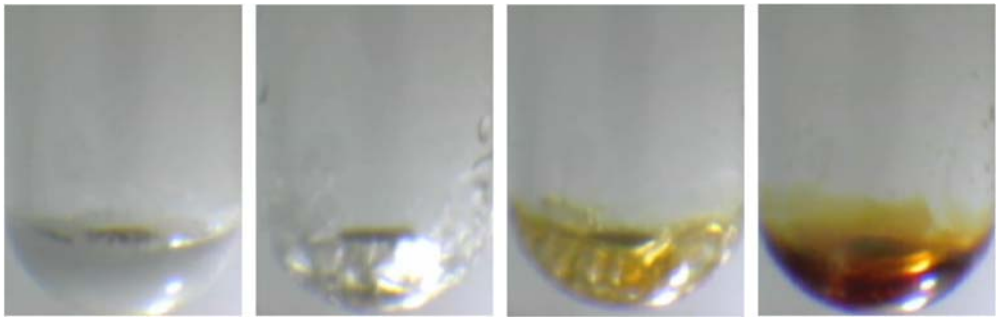

Figure 2.2. Photographs of the vial during the microwave synthesis of CNDs.

2.3.2. Purification

After the heating process, the as-prepared CNDs were dissolved in water and filtered through 0.1 μm microporous membrane to remove large carbon nanoparticles. The filtered solution was dialyzed against water for 48 h, until no basic solution was detected in the wasted waters, due to the unreacted EDA or other small organic molecules. Finally, the CNDs were freeze-dried obtaining a yellowish powder.

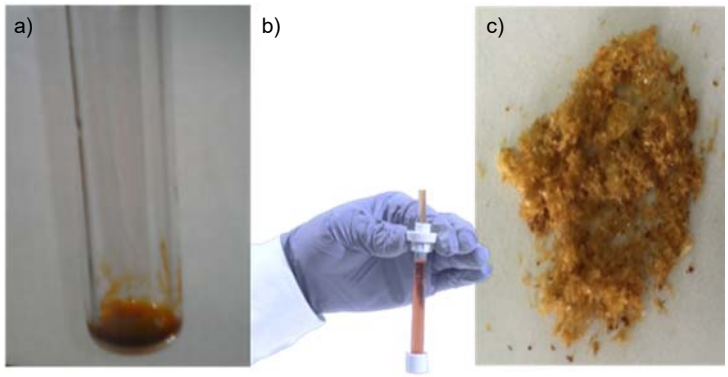

Figure 2.3. Photographs of the a) crude CNDs, b) dialysis procedure and the resulting c) CNDs powder.

2.3.3. Characterization

The as-prepared CNDs were characterized by UV-Vis, FL, FT-IR, XPS, TEM, AFM and DLS techniques. The UV-Vis spectrum presented a broad UV absorption band with a tail extending up to the visible region (**Figure 2.4**). Absorption edge at around 275 nm could be due to the π–π* transition which confirms the existence of aromatic π- system in the dots.[11,12]

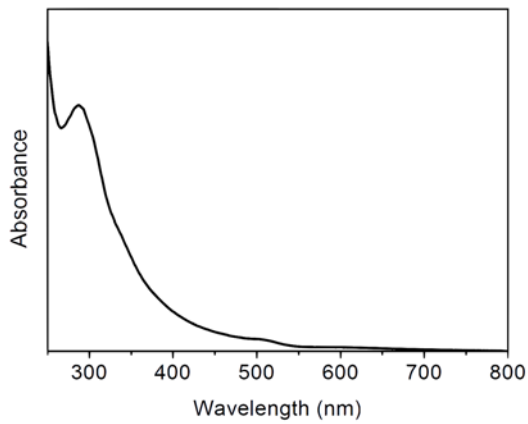

Figure 2.4. UV-Vis spectrum of CNDs in water.

The fluorescence emission (**Figure 2.5**) of CNDs showed the typical excitation-dependence of the nanomaterials,[134] but they did not show up-conversion properties. The maximum emission intensity at 365 nm is observed with an excitation wavelength of 300 nm, and the emission peak red shifts increasing the excitation wavelength. Moreover, the quantum yield (QY) of the nanoparticles was determined by a comparative method using quinine sulfate in 0.1 M H_2SO_4 (QY= 54 %) as reference standard.[135] The relative value of QY under excitation of 300 nm was evaluated as 15 %, which is higher or comparable with most of the nitrogen containing carbon dots reported so far.[130,131]

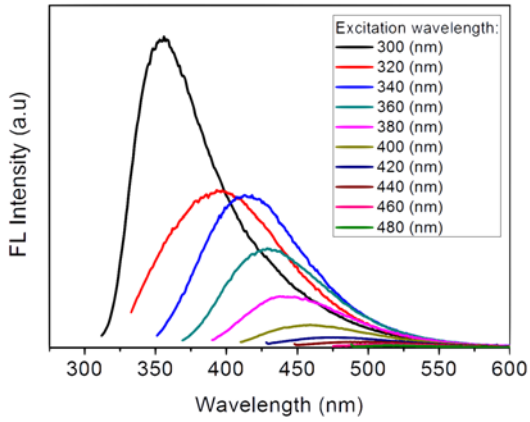

Figure 2.5. FL emission spectra of CNDs at different excitation wavelengths in water.

Figure 2.6 reports the photographs of the solutions of CNDs in H_2O in daylight and under UV light exhibited a high solubility in water (up to 80 $mg \cdot mL^{-1}$)[31] and also in common polar organic solvents. Moreover, a high stability of the solution in water was observed.

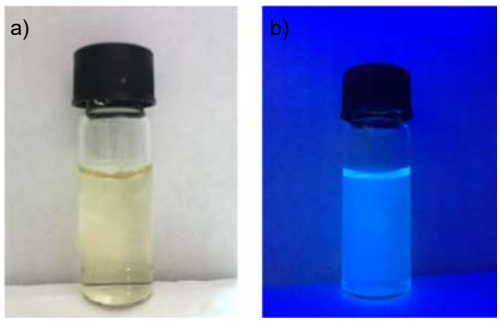

Figure 2.6. Photographs of CNDs in H_2O a) in daylight and b) under UV light (365nm).

Furthermore, the structure and composition of the CNDs were determined by FT-IR and X-ray photoelectron spectroscopy to gain more information about CNDs. The surface of the dots present many O and N functional groups and a representative structural unit was reported by our group (**Figure 2.7**).[31]

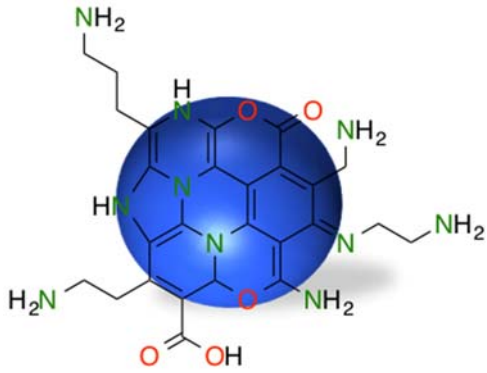

Figure 2.7. Representative structural composition and functional groups of CNDs.[31]

FT-IR spectroscopy was employed in order to identify the NCNDs surface functional groups (**Figure 2.8**). First, the broad peak centered at 3322 cm^{-1} was attributed to the O–H or N–H stretching vibrations. The C–H stretching vibration was showed by the peaks at 2946 and 2866 cm^{-1}, while the peaks between 1550 and 1750 cm^{-1} were attributed to C=O, C=N stretching vibration bands and N–H bending bands. Peaks in the range 1330-1480 cm^{-1} corresponded to a combination of a C–N stretching and C–H bending bands.[16,17] Therefore, the existence of hydroxyl, carboxyl and amino groups was clear. These functional groups contribute to the hydrophilicity and stability of the CNDs in aqueous medium as was observed in **Figure 2.6**. In addition, the presence of a high amount of amine groups (1053 $\mu mol \cdot g^{-1}$) was also confirmed by Kaiser Test.[41]

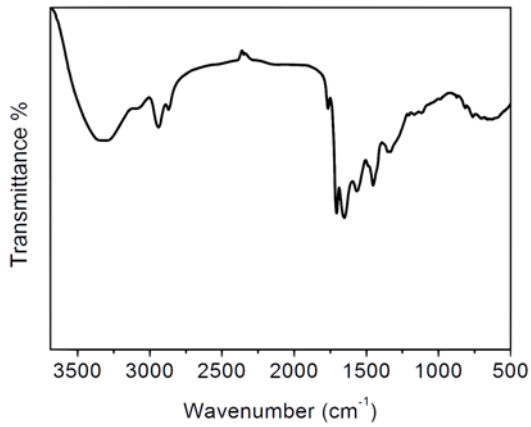

Figure 2.8. FT-IR spectrum of CNDs.

XPS measurements were carried out to confirm the surface composition of CNDs. As shown in **Figure 2.9**, the C 1s 285.2 eV, N 1s 388.5 eV and O 1s 531.3 eV peaks were the three major elements observed for the pristine CNDs, having 70.1, 18.5 and 11.4 atom %, respectively.[31] The high-resolution C 1s spectrum was deconvoluted into four signals corresponding to sp^3 C-C and C-H bond at 285.0 eV, C-N and C-O bond at 286.1 eV, C=N and C=O at 287.7 and COOH bond at 288.6 eV, respectively. Moreover, N1s spectrum was deconvoluted into three peaks centered at 398.9 eV corresponding to C=N, NH_2 and C-N-C at 399.7 eV and N-C_3 at 401.2 eV. Finally, the peak associated with the O 1s was deconvoluted into two signals corresponding to the C=O at 531.3 eV and C-O bond peaks at 532.9 eV (**Figure 2.9**, **Table 2.1**).

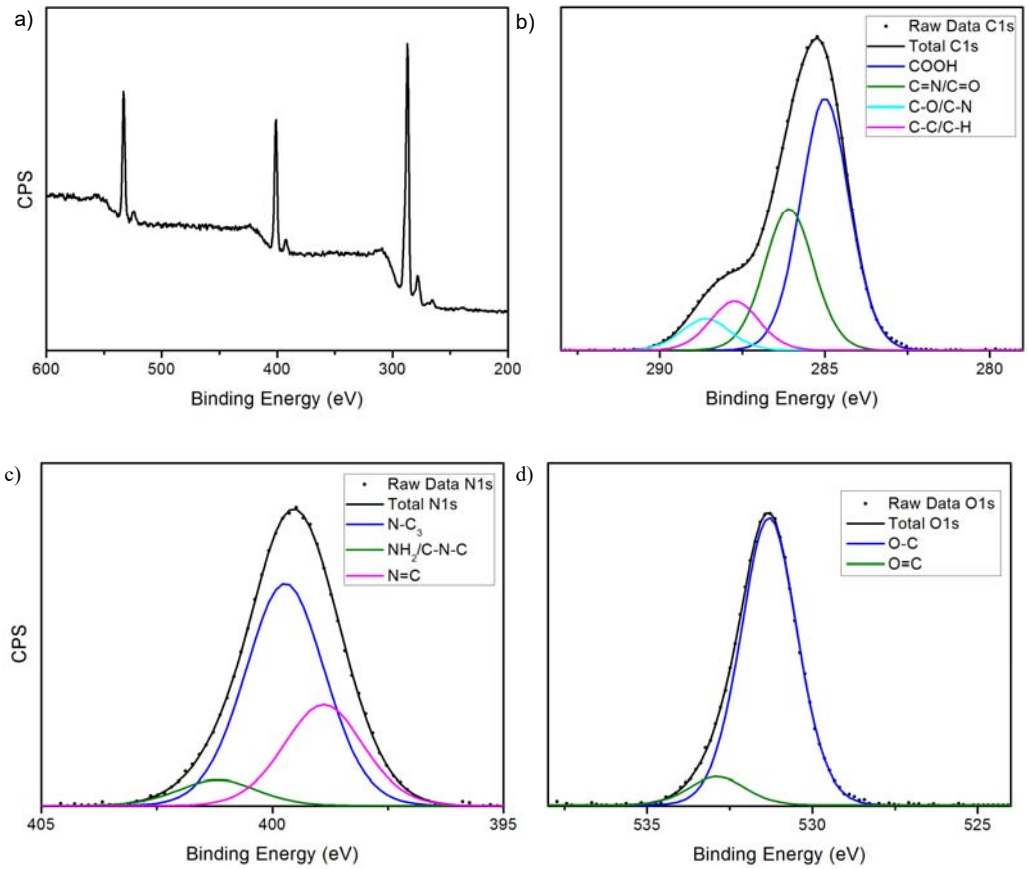

Figure 2.9. a) XPS survey spectrum of the CNDs and the deconvoluted of b) C 1s, c) N 1s and d) O 1s spectra.

Table 2.1. Binding energy and percentage of C, N, and O atoms in CNDs as determined by XPS measurements.

C 1s	**285.2 eV**	**70.1 %**
C-C/C-H	285.0	53.1
C-O/C-N	286.1	29.9
C=N/C=O	287.7	10.4
COOH	288.6	6.6
N 1s	**388.5 eV**	**18.5 %**
N=C	398.9	29.0
NH_2/ C-N-C	399.7	64.0
N-C_3	401.2	7.0
O 1s	**531.3 eV**	**11.4 %**
O=C	531.3	90.1
O-C	532.9	9.9

TGA measurements were carried out in order to study the thermal stability and the weight loss with respect to the temperature. The TGA analysis (**Figure 2.10**) showed that CNDs were stable up to 130 ºC and loss of weight resulted afterwards. The latter at 178 ºC could be related to the degradation of associated chemical moieties with the dots (*i.e.* water molecules and other species attached through weak hydrogen interactions). Besides, it was observed another loss of weight of around 16 % at 350 °C which may be due to the variety of aliphatic moieties from the dots. Subsequently, the degradation of the aromatic functional groups. Finally, it was observed the weight loss of about 90 % surface functional groups at 800 ºC.

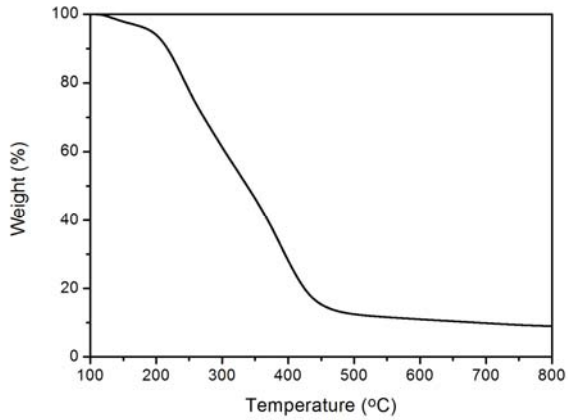

Figure 2.10. Thermogravimetric analysis under N_2 purge with a heating rate of 10 °C·min^{-1}.

The size and morphology of the CNDs were determined by transmission electron microscopy (TEM) and atomic force microscopy (AFM). Negative staining technique was used to enhance the contrast in TEM and thus allowing an easier visualization of

the CNDs.[136] As can be observed in **Figure 2.11** the CNDs are mostly spherical dots and quite monodisperse, with an average size of 4.4 ± 0.9 nm. Moreover, it was carried out HRTEM studies of CNDs, the images of the dots revealed the non-crystalline nature of the particles, which is a typical feature of carbon nanodots in contrast to carbon quantum dots.[134]

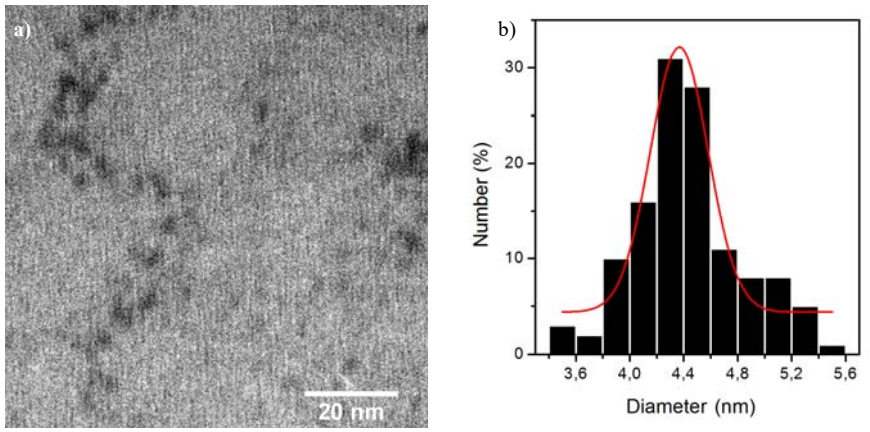

Figure 2.11. a) Negative staining TEM image of CND with the corresponding b) size distribution histogram.

AFM images revealed that CNDs were composed of small spherical particles with a size distribution in the range between 1 nm and 7 nm, with an average size of 3.7 ± 1.8 nm, as determined by statistical analysis of about 100 particles (**Figure 2.12**). Interesting, it was found that the dots had a very strong tendency of self-aggregation during the AFM preparation. Thus, highly diluted samples were used.

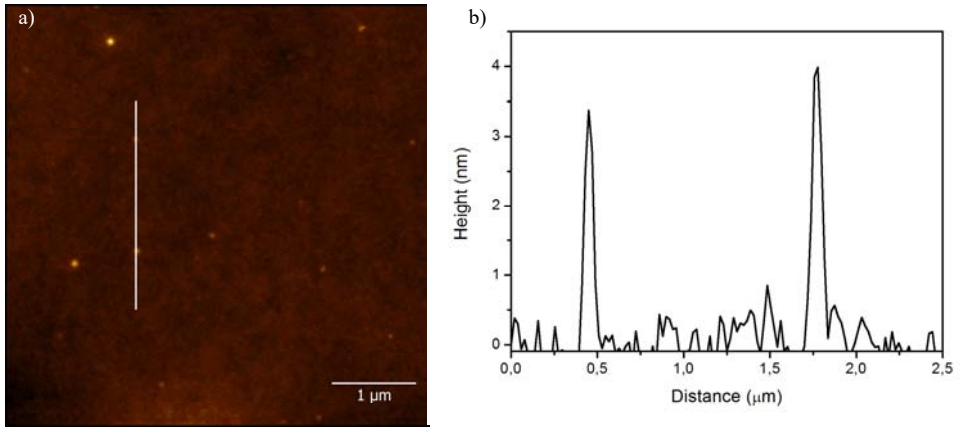

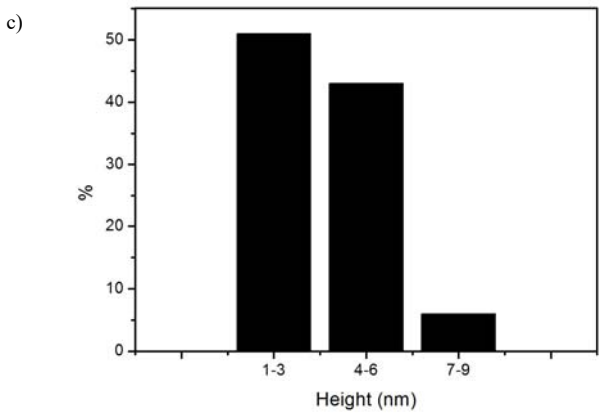

Figure 2.12. a) AFM topography image of CNDs on a mica substrate, b) the corresponding height-profile analysis along the line and c) the size distribution histogram.

To confirm TEM and AFM results, the dynamic light scattering (DLS) measurements further indicated that the CNDs in phosphate buffer solution at pH 7.4 had an average diameter of 8.3 ± 0.7 nm (**Figure 2.13**). As expected, the hydrodynamic diameter was reasonably higher from that obtained by TEM and AFM due to their hydration in solution.

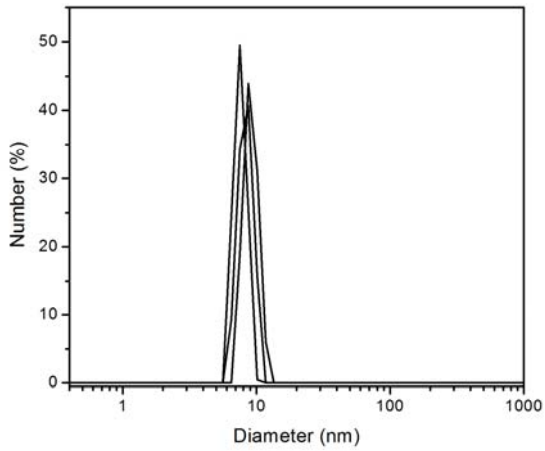

Figure 2.13. Hydrodynamic diameter d_h analysis determined by DLS.

By laser doppler anemometry (LDA) analysis, the surface charge of CNDs in phosphate buffer at pH 7.4 was measured and a zeta potential value of +5.4 ± 1.4 mV was obtained. This slight positive value suggested the presence of protonated amine functionalities and indicated the higher amount of amino groups as compared to hydroxyl- and carboxylic-based groups. The latter observation was further supported by gel electrophoresis. The **Figure 2.14** showed the CNDs upon visible and

ultraviolet light illumination of 1.5 % agarose gels. CNDs migrated to the negative pole indicating that they were positively charged.

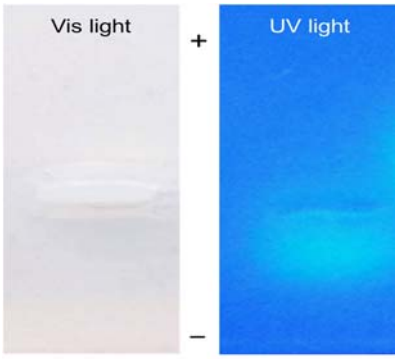

Figure 2.14. Images upon Vis and UV light illumination of 1.5 % agarose gels taken after running the CNDs.

2.4. Conclusions

In the first part of this chapter, a simple and controllable microwave-assisted hydrothermal synthesis of nitrogen-doped CNDs was performed. Arg and EDA were used as both carbon and nitrogen sources, and the nanodots were obtained after three minutes of heating, by following a synthetic protocol recently published from our group. This synthetic approach adheres to the green chemistry principles and holds promise for the development of CNDs for bioapplications.

Furthermore, it was reported the characterization of the prepared material by employing UV-Vis, FL, FT-IR, AFM, TEM, DLS and XPS techniques. CNDs showed tunable fluorescence emission, with sizes below 10 nm, excellent solubility in water and several functional groups onto their surface.

Finally, the as-prepared dots presented a wide range to perform easily functionalization due to several functional groups on their surface, such as amines. This will be discussed in the Chapter 3.

CHAPTER 3

Surface Modification of Carbon NanoDots

CHAPTER 3

Surface Modification of Carbon NanoDots

"It is sometimes said that organic synthesis is at the same time an exact science and a fine art." Nobel Laureate Dr. Robert B. Woodward

3.1. Introduction

Surface functionalization, modification or engineering is a powerful tool to tailor nanomaterials for the desired applications, also adequate the surface of this nanoparticles for the interaction with the environment.[137,138] CNDs have the ability to improve the properties of drugs, such as solubility and the circulation time in the body. Nevertheless, without surface modification, the pristine nanomaterials reduce their use on bioapplications. The surface of CNDs presents several reactive groups, such as amines and acids, which can be functionalized post-synthetically with organic, polymeric, inorganic or biological materials with specific functions.[137,2,3] Moreover, among all the excellent properties that CNDs present, such as their strong photoluminescence, biocompatibility and non-toxicity, make them promising candidates for biomedicine; thus, it is not a surprise the exponential interest emerged in the last years.[42]

Surface functionalization of CNDs consists, as was mentioned above, in introduce an effective linkage to connect them better to the field of bioapplications, such as bioimaging, drug delivery systems and theranostics. For instance, in this thesis, CNDs were modified with: (*i*) polyethylene glycol chains in order to avoid CNDs to be detected by the immune system; (*ii*) maleimide for further attachment of biomolecules; (*iii*) iron nanoparticles to create multifunctional nanoplatforms for

magnetic resonance imaging; (*iv*) drugs for drug delivery systems and (*v*) proteins. For this commitment, the dots were mainly functionalized *via* covalent approaches, thanks to the amines that our CNDs present on their surface. Moreover, CNDs were functionalized *via* non-covalent with proteins, in order to avoid the structural modification of the proteins.

Numerous methods have been employed for the surface modification of fluorescent carbon nanoparticles: heteroatom-doping,[122] surface passivation,[139] covalent and non-covalent functionalization. In this thesis, we will explore the two main methodologies based on covalent and non-covalent modifications (**Figure 3.1**).

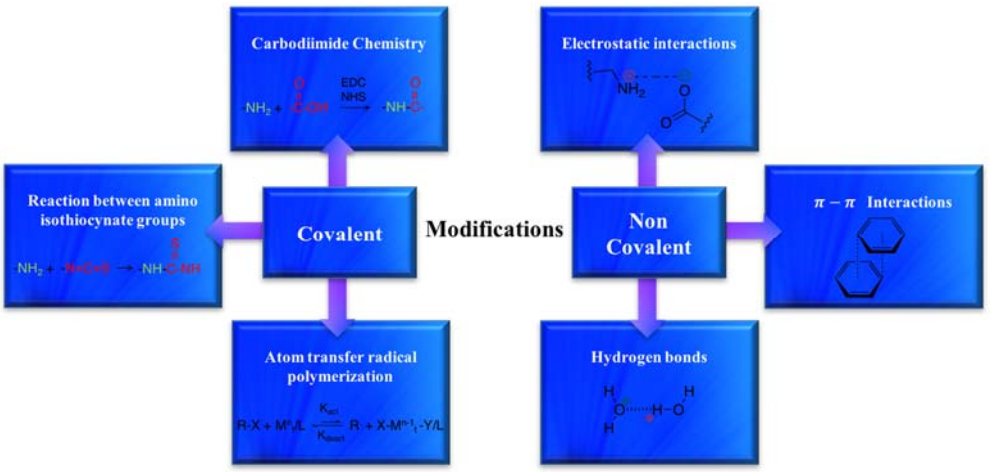

Figure 3.1. Methodologies for the surface modification used for C-Dots.

3.1.1. Covalent functionalization

This functionalization is based on the covalent attachment of functional molecules to the surface of CNDs. The formation of a covalent bond generally presents a high stability; besides, starting points for further modifications can be created.

CNDs, as commented in Chapter 2, present several functional groups on their surface, most of the groups are amines. Amines can contribute to numerous reactions, including amidation reactions. Below, we will discuss the covalent methods used in this thesis and the most used in literature.

3.1.1.1. Carbodiimide chemistry

Carbodiimide chemistry is one of the most exploited functionalization techniques used to conjugate various organic, polymeric, inorganic or biological materials terminated with amine or carboxyl onto the surface of CNDs coated with carboxylic or amine groups.[140] Typically, carboxylic groups are firstly activated by ethyl(dimethylaminopropyl) carbodiimide(EDC)/N-hydroxysuccinimide (NHS), and then reacted with the free amino groups.

For instance, the group of Chen applied the EDC chemistry to create a theranostic system based on chlorine e6-conjugated C-Dots.[141] Specifically, the carboxylic groups of chlorine e6, a photosensitizer used in photodynamic therapy, were activated with EDC/NHS in order to react with the amine groups of C-Dots, to covalent attached chlorine e6 through amide bonds. It is worth noting that amidation of C-Dots is one of the most exploited functionalization technique in this thesis, due to the high amount of amines onto the CNDs surface.

3.1.1.3. Reaction between amino and isothiocyanate groups

Isothiocyanate group –N=C=S can very easily react with amines. For instance, Ma and co-workers described a tunable ratiometric pH sensor based on C-Dots.[142] The sensor was fabricated by conjugating fluorescein isothiocyanate (FITC) and rhodamine B isothiocyanate (RBITC) onto the amino-coated C-Dots. In detail, the amino-coated CNDs solution was treated with FITC and RBITC at different molar ratios in 0.1 M $NaHCO_3$ solution at room temperature overnight. Then, the system was finally purified by thorough dialysis and gel chromatographic separation. Similarly, functionalization of C-Dots with isothiocyanate group –N=C=S allowed Du *et al.* to create a pH ratiometric fluorescent nanosensors based on C-Dots and FITC.[143]

3.1.1.4. Atom transfer radical polymerization

Atom transfer radical polymerization (ATPR) was described for the first time by Matyjaszewski's research group and consists in a controlled "living" polymerization based on the use of radicals to convert monomers to polymers.[144] Radical polymerization, can polymerize hundreds of monomers, copolymerize two or more monomers, and can be performed in water as emulsions or suspensions.[145,146]

The Liu *et al.* in 2014 reported the creation of a multifunctional platform for serum resistant gene delivery and bioimaging through ATPR reaction.[147] In detail, the surface functionalization of the dots was prepared *via* ATPR reaction between the ATRP initiator Dots-Br and the polycation-b-polysulfobetaine block copolymer, chemical known as poly-[2-(dimethylamino) ethyl methacrylate]-b-poly[*N*-(3-(methacryloylamino) propyl)-*N,N*-dimethyl-N-(3-sulfopropyl) ammonium hydroxide] (PDMAEMA-b-PMPDSAH). Then, the mixture was dialyzed against deionized water for 7 days to completely remove the unreacted products. The final dots acquired new properties for biological applications, such as gene delivery and imaging.

3.1.2. Non-covalent functionalization

Non-covalent functionalization of CNDs has been extensively studied since it presents the main advantage of not affecting the properties of the dots.[138] However, non-covalent interactions are weaker than covalent bonds and non-covalent

functionalization is generally less stable than the covalent one. This modification method is based on non-covalent interactions as van der Waals forces, π-π aromatic stacking, electrostatic interactions or hydrogen bonds. There are many examples in the literature with different biomolecules, including proteins, enzymes, oligonucleotides or DNA.[148,149,150]

3.1.2.1. Electrostatic interactions

Electrostatic interactions are based on forces between the different electrical charges of the atoms. Usually occur between atoms that present a completely positive charge and a completely negative charge. Recently, Wu *et al.* argued that charged C-Dots can be functionalized by materials with opposite charges via electrostatic interactions.[151] To prove it, they developed a theranostic nanoagent for gene delivery in lung cancer therapy using modified carbon dots and siRNAs. Similarly, Datta and co-workers prepared a fluorescent hybrid with controlled selective labelling of the cell nucleus and the cytoplasm.[152] Specifically, the dots were modified by anionic graphene oxide sheets *via* electrostatic interactions.

3.1.2.2. Hydrogen bonds

The hydrogen bond consists in an electrostatic attractive force, between an electronegative atom and a hydrogen atom covalently attached to another electronegative atom. By way of illustration, Liu *et al.* developed a novel turn-on biosensor based on the fluorescence of C-Dots.[153] For this purpose, they functionalized carboxy coated C-Dots with folic acid via hydrogen bond. Folic acid was mixed with C-Dots in solution. After being stirred for 10 min, the mixture was dialyzed for 2 h to remove the excess of folic acid.

3.2. Aim of the work

The surface modification is a powerful method to tune the surface properties of materials for selected applications, as commented along the previous introduction. In this chapter, CNDs will be functionalized and, therefore, characterized in order to be applied for the desired bioapplication (Chapter 4).

Figure 3.2 collects a general design of this chapter. In the center, CND is represented, around it all the derivatives used for the functionalization with specific purposes: (*i*) pegylated molecules called also "Stealth Molecules",[154] are used in order to avoid the formation of the protein corona and therefore the detection of the dots by the immune system, (*ii*) maleimide can be used as target molecule for additional attachment of SH groups present in several biomolecules; (*iii*) cyanine dye is used for bioimaging; (*iv*) iron nanoparticles for further bio-applications such as bioimaging or therapeutic functions, which make them promise multifunctional nanoplatforms for both diagnosis and therapy; (*v*) drugs, such as Taxol and Chlorambucil to make drug delivery systems and (*vi*) proteins, to study the cell internalization (studied developed in collaboration with Dr. Carolina Carrillo-Carrión).

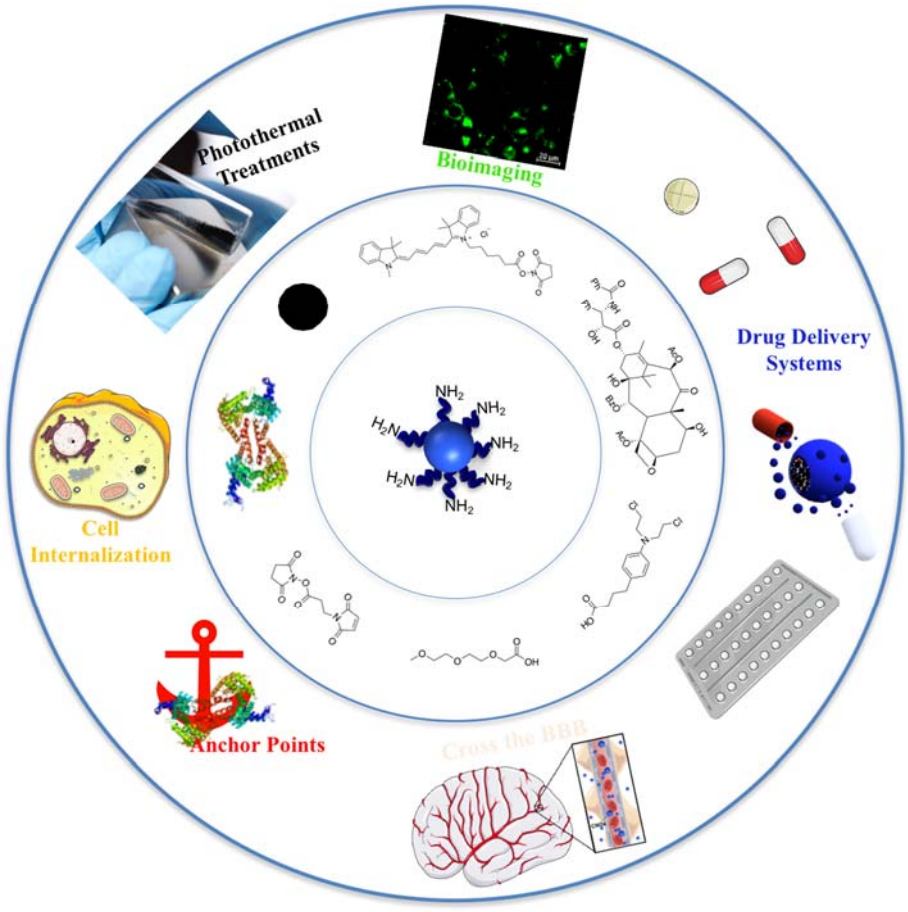

Figure 3.2. General design of CNDs functionalization and their possible bioapplications.

3.3. Results and discussion

Within this section, modification of CNDs with different organic molecules, iron nanoparticles, drugs and proteins will be described by using different synthetic approaches: covalent and non-covalent approaches. Moreover, studies about the influence of the equivalents functionalization of CNDs will be presented.

3.3.1. Covalent functionalization

3.3.1.1 Organic molecules

3.3.1.1.1. CNDs-DEGd

One of the most interesting properties of CNDs is fluorescence. For this reason, the functionalized nanomaterial should maintain this feature, among the others. Therefore, in a first functionalization a study of the influence of the equivalents was performed in this chapter. The first functionalization of CNDs was carried out with [2-(2-Methoxyethoxy)ethoxy]acetyl acid (**4**) (DEGderivative, DEGd) through carbodiimide chemistry, with EDC/NHS as coupling agents (**Figure 3.3**).

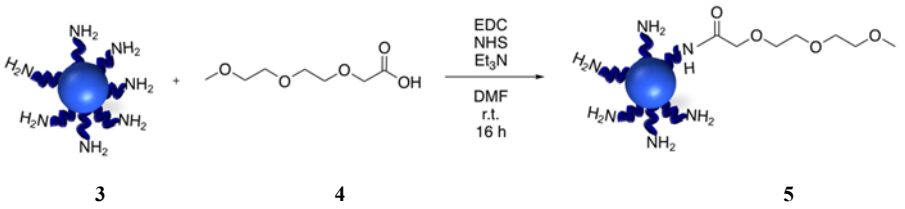

Figure 3.3. Functionalization of CNDs *via* amide bond formation.

In the first step, a scan of different equivalents of organic molecule **4** was carried out (**Table 3.1**, **Figure 3.3)**. More specifically, the molar ratio was increased, therefore their fluorescence properties, among others, will be modified.

Once that our functionalized nanomaterial was obtained and purified, a Kaiser test was performed in order to estimate the degree of reacted amines. As **Table 3.1** showed, the amounts of amines decreased (the initial amount of CNDs batch was 1256 $\mu mol \cdot g^{-1}$). An unexpected result was observed in Entry 3 (**Table 3.1**) which could be related to the saturation point of amine groups, that was reached with 2.5 equivalents of DEGd.

Table 3.1. Optimization of the functionalization and Kaiser test results.

ENTRY	CNDs (equiv)	4 (equiv)	KAISER TEST ($\mu mol \cdot g^{-1}$)
1	1	1	263.2
2	1	2.5	89.4
3	1	5	90.9

The blue spectrum represented **Figure 3.4** showed the characteristic band of 1706 cm^{-1}, which indicates the presence of amide (O=C-NH) in CNDs-DEGd. The broad band centered at 2800 cm^{-1} (ν C-H stretching vibrations) in DEGd it was observed in CNDs-DEGd, indicating that CNDs were modified to CNDs-DEGd successfully.

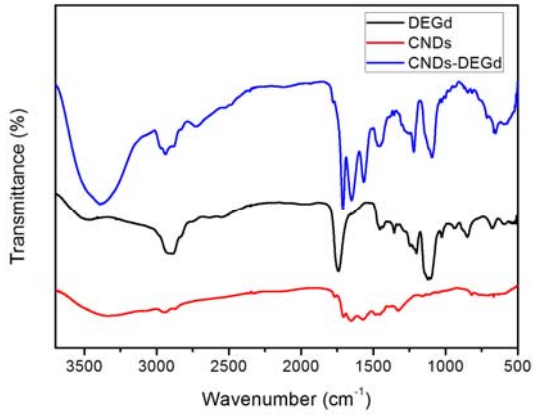

Figure 3.4. FT-IR spectra of CNDs-DEGd, DEGd and CNDs.

The FT-IR spectra of **5** (**Figure 3.5**) showed the same composition for all the CNDs-DEGd materials. An increase in the relationship between the amide and amine band was observed, *i.e.* the band at 1706 cm^{-1} corresponding to amide band increased meanwhile the amine at 1566 cm^{-1} remained (Entry 1 and Entry 2), thus confirming a higher degree of amidation.

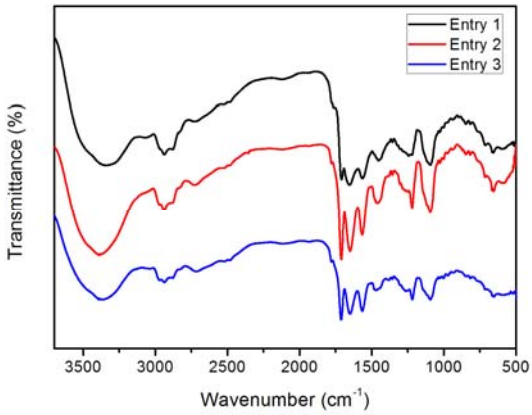

Figure 3.5. FT-IR spectra of the different reactions for CNDs-DEGd (**Table 3.1**).

UV and fluorescence measurements were performed with the same concentration (0.05 mg·mL^{-1}), solution and cuvette in order to minimize errors. As the following figures showed (**Figure 3.6**), a shift in the UV spectra of the CNDs-DEGd was produced, due to the increase of functionalization along the entries. Moreover, the low intensity of the Entry 2 (**Table 3.1**) could be due to the same reason of the result of the Kaiser test mentioned above (related to the saturation point of amine groups). Furthermore, the fluorescence measurements showed a decrease of the intensity compared to pristine CNDs, as expected, due to the changes in the surface. Additionally, the Entry 2 (**Figure 3.6c**) showed a different excitation maximum wavelength comparing with the pristine of CNDs, which showed their maximum at 300 nm (See Chapter 2).

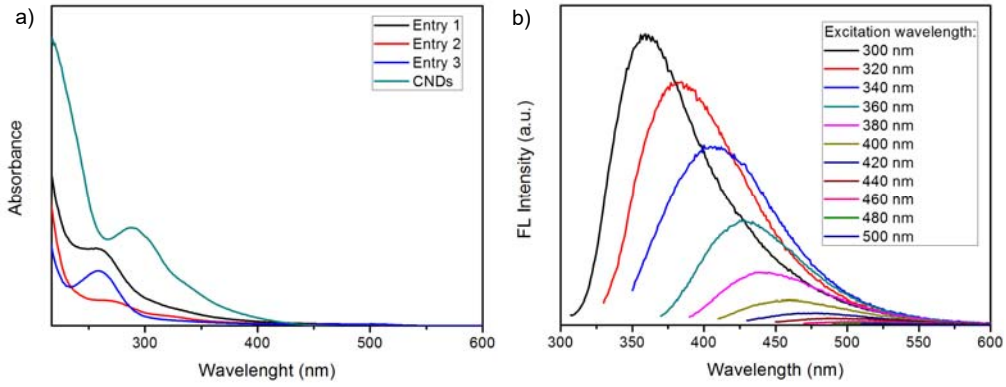

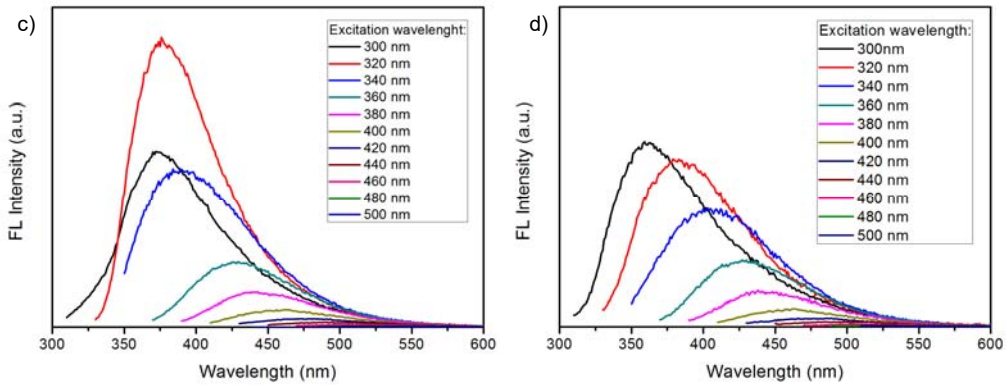

Figure 3.6. a) UV-Visible spectra of CNDs and CNDs-DEGd in water. Fluorescence emission spectra at different excitation wavelengths of CNDs-DEGd b) Entry 1, c) Entry 2, d) Entry 3 (**Table 3.1**) in water.

Moreover, the QY was calculated in order to compare the fluorescence efficiency. A decrease of the QY, in relation with the increased of the equivalents, was observed. From QY = 17 % of pristine CNDs down to QY = 11 % of the most functionalized CNDs-PEG (1:5 equivalents).

Furthermore, AFM measurements revealed almost no differences between the entries of **Table 3.1**. However, in **Figure 3.7** was graphed the AFM images of CNDs-DEGd for the Entry 3 (**Table 3.1**) with an average size of approximately 4.8 ± 1.2 nm.

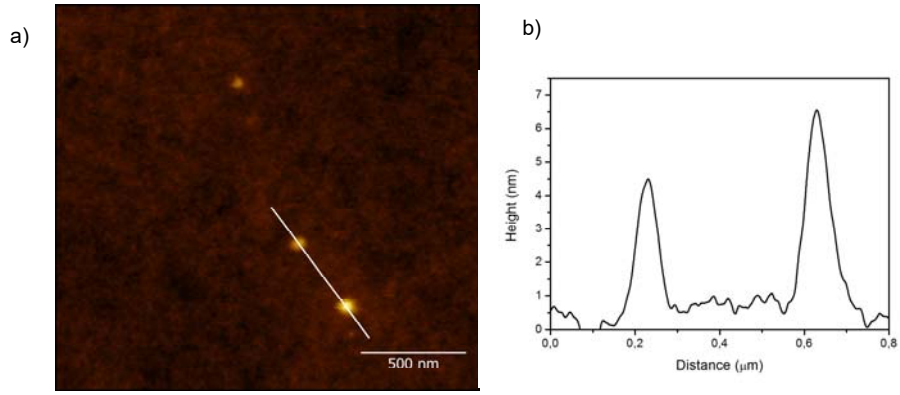

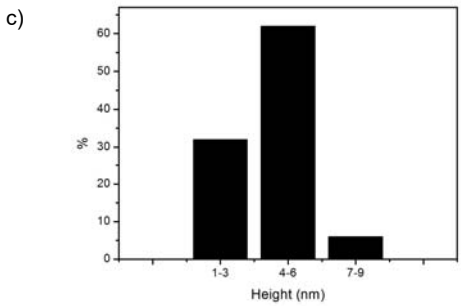

Figure 3.7. a) AFM image and b) height profile along the line of CNDs-DEGd and c) size histogram of CNDs-DEGd.

Finally, the ^{1}H NMR of the functionalized nanomaterial was carried out. One of these experiments was chosen, more specifically the Entry 2. The ^{1}H NMR of CNDs-DEGd did not display the typical peak of the acid from the molecule **4** and presented two additional peaks around 5.6 and 6.5 ppm from the amide bond and the typical signals of the starting material (**Figure 3.8**). Furthermore, the shape of the signal could correspond to this kind of groups. It is important to remark that dialysis with water was used to remove all the excess of the activated acids, which is hydrolyzed in water and returns to the acid form.

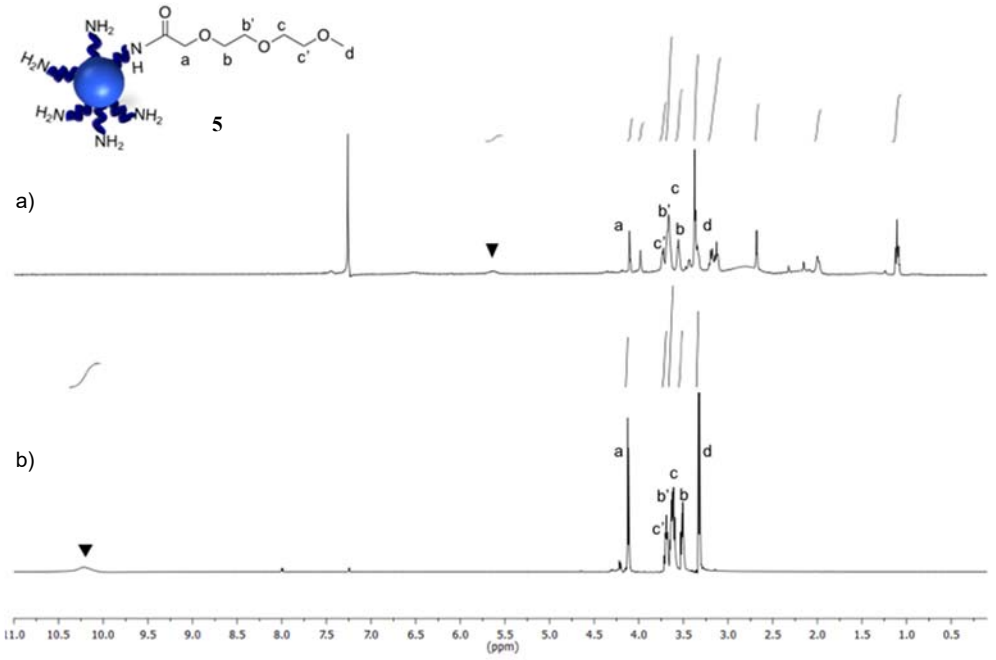

Figure 3.8. ^{1}H NMR of a) CNDs-DEGd and b) DEGd in $CDCl_3$.

To conclude, a change of the CNDs solubility was observed by functionalization with the molecule **4**, from partially soluble to totally soluble in chloroform and the solubility in water was retained. As showed aforementioned results, the functionalization of CNDs occurred successfully.

In order to confirm the results of the functionalization of PEG. We tried the same functionalization with acyl chloride without the use of coupling agents as EDC/NHS that could be retained in our final nanomaterial, and go unnoticed with the characterization techniques. First of all, it was need the functionalization with thionyl chloride of the [2-(2-methoxyethoxy)ethoxy]acetyl acid (**Figure 3.9**).[155] Then, after working up the reaction the [2-(2-methoxyethoxy)ethoxy]acetyl chloride (**6**) was characterized by ^{1}H NMR (see details in experimental section, Appendix). Finally, the acyl chloride **6** was reacted with pristine CNDs using the same equivalents of Entry 2 (**Table 3.1**), in the presence of *N,N*-diisopropylethylamine (DIPEA).

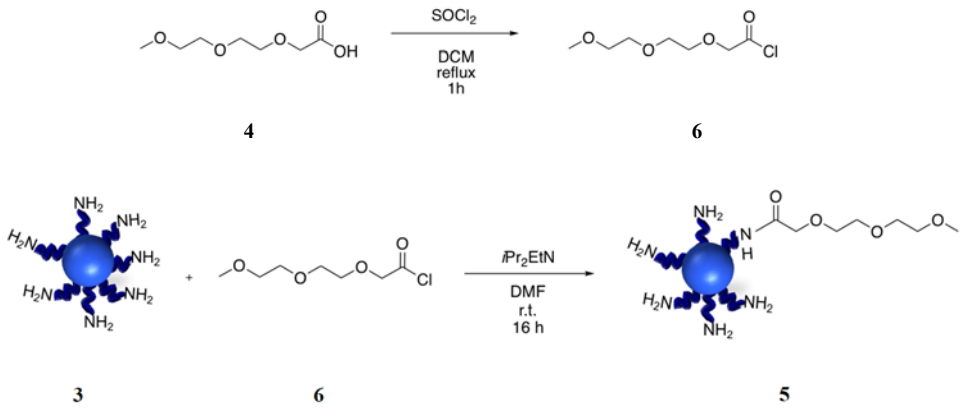

Figure 3.9. Synthesis of the desired [2-(2-Methoxyethoxy)ethoxy]acetyl chloride 6, and post-functionalization of CNDs via amide formation.

All the characterization techniques suggested the same results for the functionalization of the **Figure 3.9** in comparison with **Figure 3.3**. Thus, all the results indicated that the final nanosystem can be obtained from different starting materials and coupling agents. Moreover, we confirm that dialysis was able to purify the non-desire products, as we obtained the same results from different synthesis.

Moreover, in order to expand the CNDs candidates for our final bioapplications, the carbon dots were modified with a PEG chain, specifically PEG_{400} (see details in experimental section, Appendix).

3.3.1.1.2. CNDs-Maleimide

The preparation of the next nanosystem was carried out with N-succinimidyl 3-maleimidopropionate, the maleimide derivative **7**, previously synthesized in our group by Dr. Arturo Juzgado. Maleimide can be use as target molecule for additional attach of -SH groups, which are present in several biomolecules (**Figure 3.10**). This functionalization was carried out with a maleimide derivative activated with NHS ester. Then, following the same study of equivalents that were mentioned above (**Table 3.2**). The results of the Kaiser tests showed that the amount of free amines was decreased when more equivalent of maleimide derivative 7 was used.

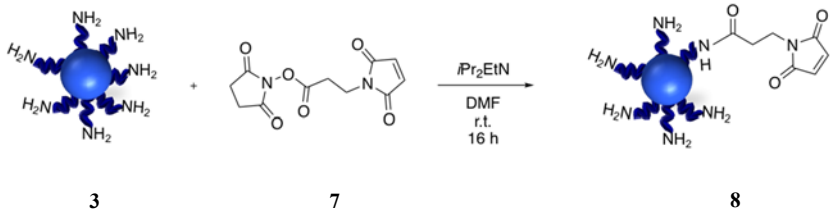

3 **7** **8**

Figure 3.10. Functionalization of CNDs via amide formation.

Table 3.2. Optimization of the functionalization and Kaiser test results.

ENTRY	CNDs (equiv)	7 (equiv)	KAISER TEST (μmol·g^{-1})
1	1	1	720.0
2	1	2.5	361.6
3	1	5	125.9

The entry 3 was chosen to follow with the analysis. In **Figure 3.11**, the blue spectrum showed the characteristic bands of CNDs (see, Chapter 2),[43] indicating that CNDs were modified on CNDs-Maleimide successfully. The as-prepared system CNDs-Maleimide showed the presence of functional groups such as O–H and N–H in the region of 3400–3150 cm^{-1}. The signals at 1615 and 1454 cm^{-1} were assigned to the stretching bands of aromatic carbon atoms (C=C). The weak signals around 1240, 1174 and 1106 cm^{-1} were related to different modes of C–O–C- and C–O- groups, respectively. Moreover, we observed an increased in the band at 1700 cm^{-1} from amide bond, confirming the amidation.

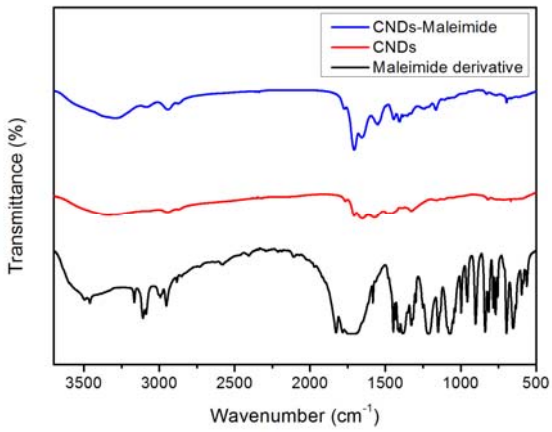

Figure 3.11. FT-IR spectra of CNDs-Maleimide, CNDs and maleimide derivative **7**.

The FT-IR spectra of CNDs-Maleimide showed the same bands for all the experiments, but not the intensity (**Figure 3.12**). The intensity of Entry 3 was higher than the others, as it was expected, due to the higher degree of the amidation.

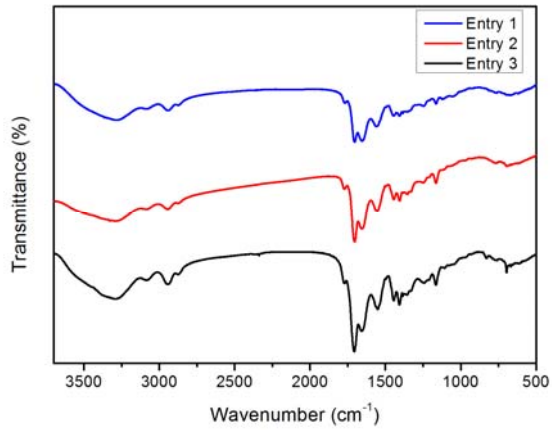

Figure 3.12. FT-IR spectra of the different reactions for CNDs-Maleimide.

As the following figures showed, an increase and shift in the UV spectra of the CNDs-Maleimide was observed, when more equivalent of maleimide derivative **7** was used. Moreover, the fluorescence measurements showed a decrease of the intensity, as expected, and also showed that the **Figure 3.13c** and **d** presented a different optimal excitation wavelength, in comparison with the batch of CNDs that showed their maximum at 300 nm (see chapter 2).

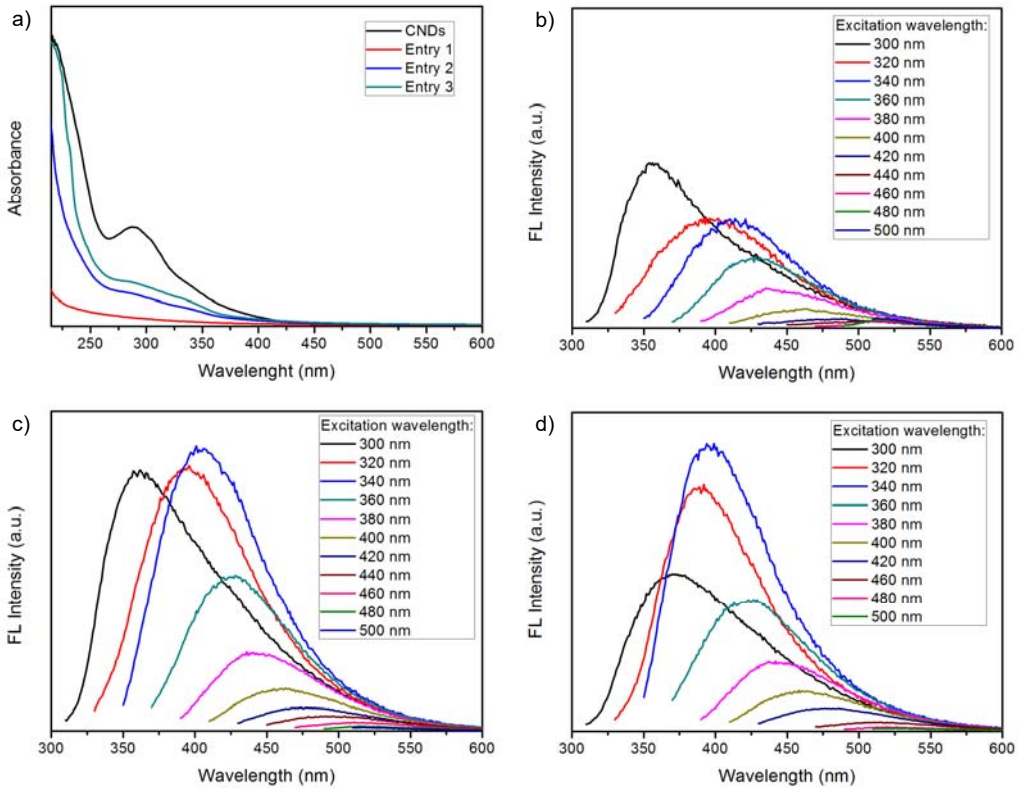

Figure 3.13. a) UV-Visible spectra of CNDs and CNDs-Maleimide in water. The fluorescence emission spectra at different excitation wavelengths of CNDs-Maleimide b) Entry 1, c) Entry 2, d) Entry 3 (**Table 3.2**) in water.

Moreover, the QY was calculated in order to compare the fluorescence efficiency. It was observed a decreased of the QY in relation with the increased of the equivalents. From 17 % of pristine CNDs, almost 17 % for CNDs-Maleimide (1:1 equivalents) and up to 14 % for CNDs-Maleimide from the most functionalized CNDs-Maleimide, 1:5 equivalents and 1:2.5.

Furthermore, **Figure 3.14** showed the AFM image and the height profile, where the measurements revealed similar sizes as was found in the case of CNDs-DEGd. Up to 1:5 equivalents used for the reaction differences in size were not detected, a large range of sizes was observed of functionalization from 3 nm up to 7 nm with an increase of the average size from CNDs pristine. The as-prepared CNDs-Maleimide showed an average of 4.3 ± 1.3 nm.

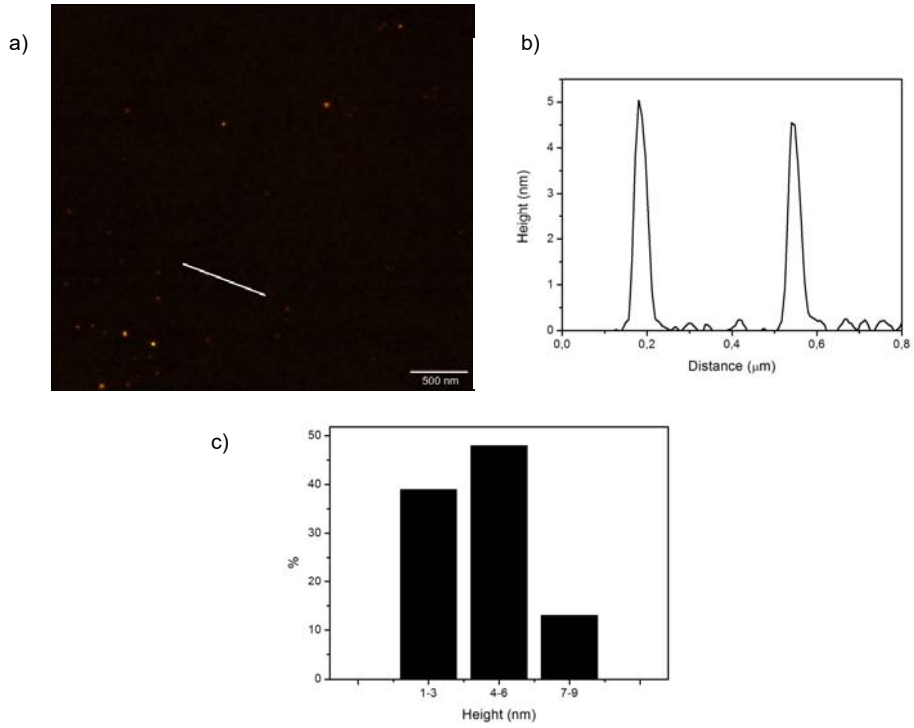

Figure 3.14. a) AFM image and b) height profile along the line of CNDs-Maleimide and c) size histogram of CNDs-Maleimide.

In relation to expand our methodology, in this case we studied different methods of purification. The products mentioned above were purified by dialysis, thus only one sample was obtained (Entry 3, **Table 3.2**). On the other hand, the crude of the reaction was filtered and concentrated under reduced pressure. Then, it was purified by size exclusion chromatography (SEC) (Sephadex LH-20; MeOH), obtaining two fluorescent fractions with light yellow aspect.

The FT-IR spectra of CNDs-Maleimide (**Figure 3.15**) showed no significant differences between the FT-IR of CNDs-Maleimide dialysis and CNDs-Maleimide SEC.

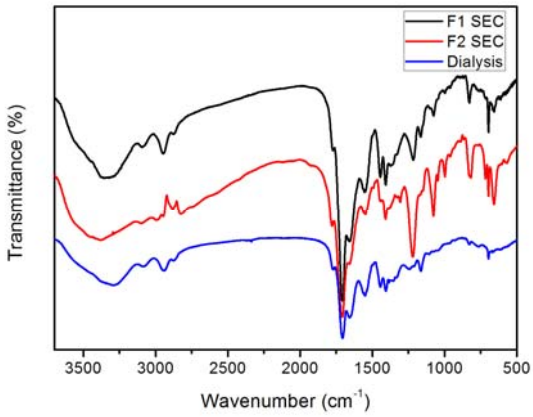

Figure 3.15. FT-IR spectra of CNDs-Maleimide purified by dialysis and SEC.

UV and fluorescence measurements were performed, the size and functional groups affected the optical properties. Thus, the UV-Vis spectra of CNDs from dialysis showed an absorption peak at 287 nm, from SEC F1 at 290 and F2 a broad band from 286-300 nm (**Figure 3.16**).

The fluorescence measurements (**Figure 3.16**) showed a different optimal excitation wavelength (340 nm), when compared to pristine CNDs (maximum at 300 nm). However, the QY of the F2 was slightly higher than F1, which had more molecules onto their surface as was the first fraction of the SEC. The chemical nature of the surface of CNDs was modified. The CNDs modified for SEC purification were produced with an excess of equivalents of the maleimide derivative *i.e.* 1:5 equivalents (Entry 3, **Table 3.2**), due to that pristine CNDs were not found. We could assure that the surface of CNDs with this amount of equivalents was covered.

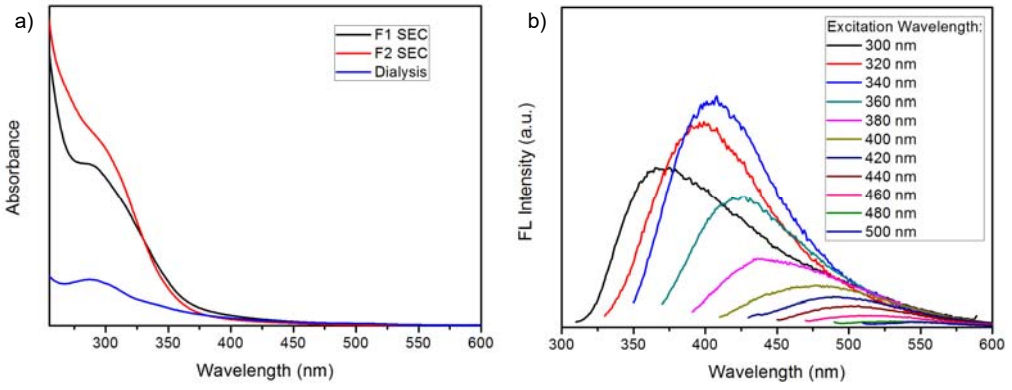

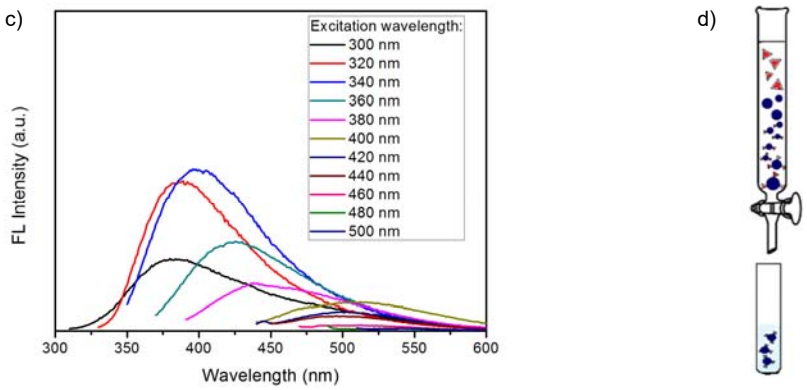

Figure 3.16. a) UV-Visible spectra of CNDs-Maleimide in water purified by SEC and dialysis. The fluorescence emission spectra at different excitation wavelengths of CNDs-Maleimide b) F1 and c) F2 of SEC and d) schematic representation of SEC.

The previous study of equivalents with DEGd and maleimide group can help us to predict the properties of the following functionalization. For instance, when the surface is modified, the optical properties of pristine CNDs as well; depending on the amount used a shift is produced, more specifically in the FL properties. Thus, pristine CNDs showed their maximum emission FL when is irradiated with an excitation wavelength of 300 nm, on the other hand functionalized CNDs showed their maximum emission FL when is irradiated with an excitation wavelength of 320 or 340 nm.

3.3.1.1.3. CNDs-Cy5

This thesis is focused on the synthesis and functionalization of CNDs for bioapplications. CNDs presented a unique photoluminescent properties, *e.g.*, tunable fluorescence emission and excitation-dependent fluorescence emission.[87] However, the fluorescence of CNDs overlaps with several dyes that are necessary to measure the cellular apoptosis, as for example the 4',6-diamidino-2-phenylindole (DAPI), which binds strongly to AT regions of DNA.[156] Since the counterstain and CNDs fluorescence emission spectra overlap, the cyanine (Cy5) label was chosen in order to differentiate CNDs from nuclear counterstains (**Figure 3.17**).

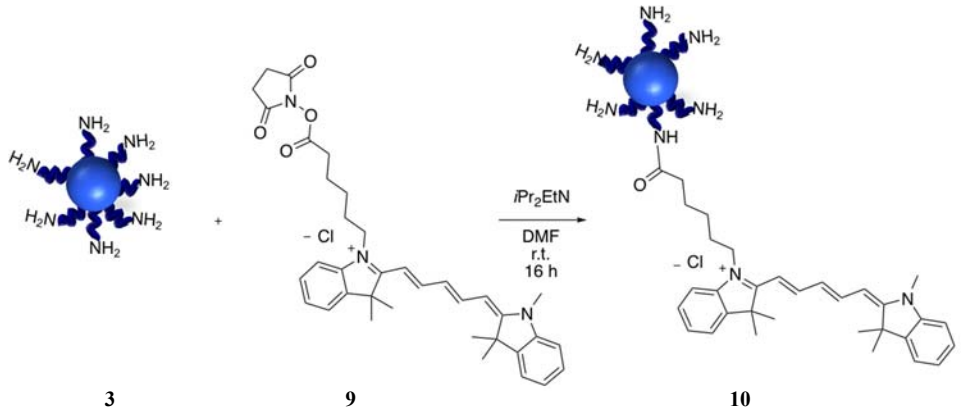

Figure 3.17. Scheme modification of CNDs with Cy5.

The optical properties were investigated with UV-Vis and FL spectroscopies (**Figure 3.18**). As showed in **Figure 3.18a**, the UV spectrum of the CNDs-Cy5 is composed by a shoulder in the 250-350 nm range (attributed to CNDs) and the 550-680 nm range (from Cy5 dye). Moreover, the fluorescence spectrum of CNDs-Cy5 (plotted in **Figure 3.18b**) showed also excitation wavelength-dependent emission, similarly to the pristine CNDs (see Chapter 2), and the emission at 660 nm from Cy5.

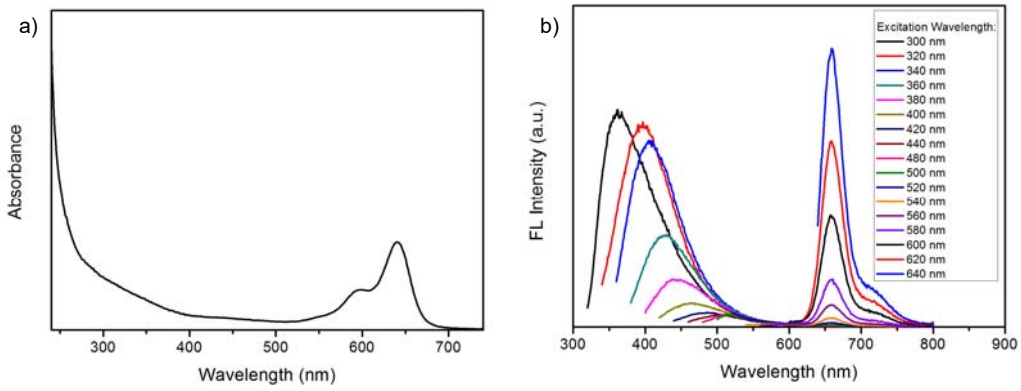

Figure 3.18. a) UV-Vis and b) FL spectra of CNDs-Cy5 in H_2O.

The FT-IR spectrum of CNDs-Cy5 (**Figure 3.19**) showed the characteristic bands of CNDs, such as O–H or N–H stretching vibrations in the range 3000-3500 cm^{-1}. The C–H stretching vibration showed at 2946 and 2866 cm^{-1}, while the peaks between 1550 and 1750 cm^{-1} were attributed to C=O, and C=C vibrations. Peaks in the range 1330-1480 cm^{-1} corresponded to a combination of a C–N stretching and N–H bending bands, respectively (see, Chapter 2).[43] Moreover, the spectrum of CNDs-Cy5 showed new bands around 1100 cm^{-1}, which come from Cy5 label, indicating that CNDs were modified on CNDs-Cy5 successfully.

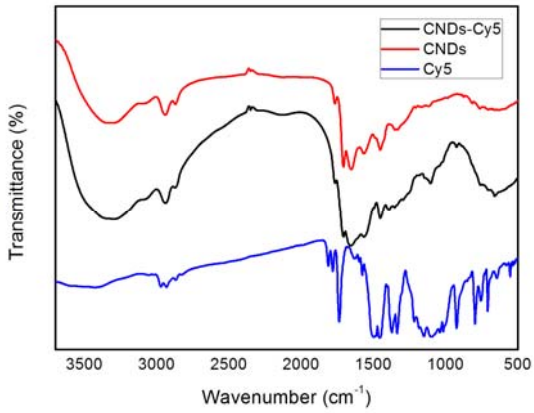

Figure 3.19. FT-IR spectra of CNDs-Cy5, CNDs and Cy5.

AFM images (**Figure 3.20**) did not give more information about the functionalization of the as-prepared system, since the size of the CNDs-Cy5 it was approximately the same of the pristine CNDs. This could be related to the low amount of Cy5 used in the reaction.

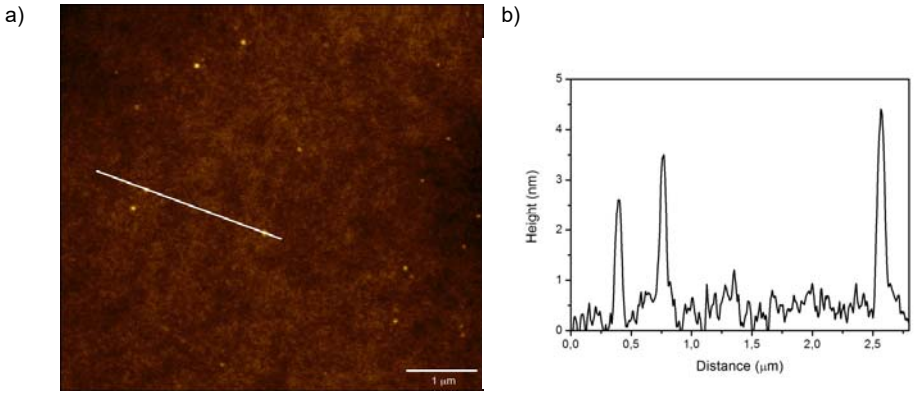

Figure 3.20. a) AFM image and b) height profile along the line of CNDs-Cy5.

3.3.1.2. Iron nanoparticles

Superparamagnetic iron oxide nanoparticles, such as F_3O_4 (FeNPs), present many interesting properties that can be used in a variety of biomedical applications, for instance magnetic resonance imaging, hyperthermia and drug delivery. Moreover, they can be manipulated by an external magnetic field to lead it to the target tissue.[157]

Furthermore, as was highlighted in Chapter 1, CNDs show high potential in bioapplications due to their excellent properties. Therefore, multifunctional nanoparticles based on carbon nanoparticles and FeNPs can efficiently convert NIR

photons to heat and kill the tumor cells by FeNPs.[158] Meanwhile, the cells can be observed due to the multicolor cell imaging properties of CNDs.[159]

Following the research line of this thesis, within this section it will be described a hybrid based on CNDs and FeNPs. First of all, FeNPs nanoparticles were synthesized and characterized. The iron oxide cores were prepared by a method of co-precipitation using ferrous (Fe^{2+}) and ferric (Fe^{3+}) salts.[160] Precise control of pH during the synthesis is required to obtain precipitation of FeNPs. To ensure the stability of the nanoparticles, the use of organofunctional silanes has been used for the biocompatibility of silica and thanks to the formation of a stable Fe-O-Si covalent bond.[161] 3-(triethoxysilyl)propylsuccinic anhydride (TEPSA) was chosen as stabilizing matrix. After that, the FeNPs were magnetically separated and then washed (**Figure 3.21**).

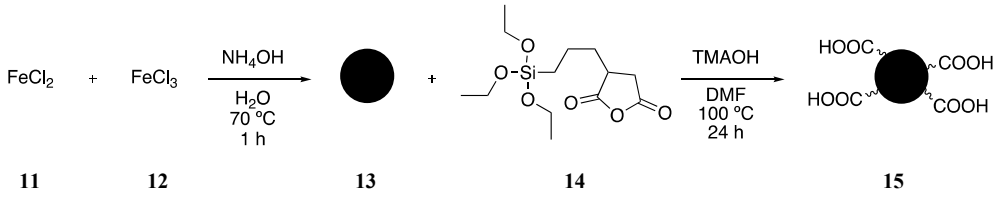

Figure 3.21. Scheme of the formation of FeNPs (**13**) and FeNPs-TEPSA (**15**).

The chemical structure of FeNPs was characterized by FT-IR spectroscopy. In **Figure 3.22** the spectra presented the peak at 582 cm^{-1} of the Fe–O bonds in FeNPs. The FT-IR spectrum of TEPSA-FeNPs showed a band at 1012 cm^{-1} from Si–O–Si or Si-O-Fe stretching vibration,[162] this bands indicated that TEPSA was introduced onto the FeNPs surface.

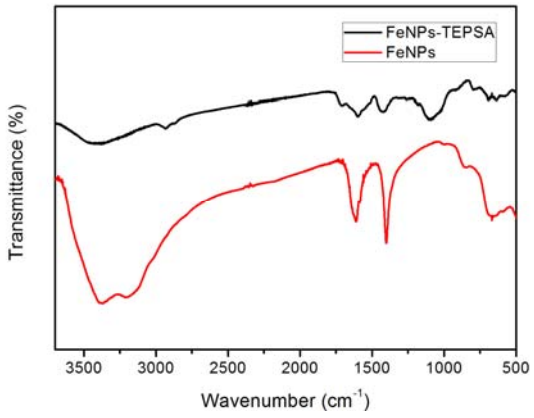

Figure 3.22. FT-IR of FeNPs and FeNPs-TEPSA.

The TEM images of FeNPS and TEPSA-grafted nanoparticles showed a uniform size and spherical shape (**Figure 3.23**). TEM measurements revealed almost no difference in the average size of FeNPs from 11.5 ± 2.9 nm to 11.6 ± 2.6 nm for FeNPs-TEPSA, as determined by statistical analysis of 100 particles.

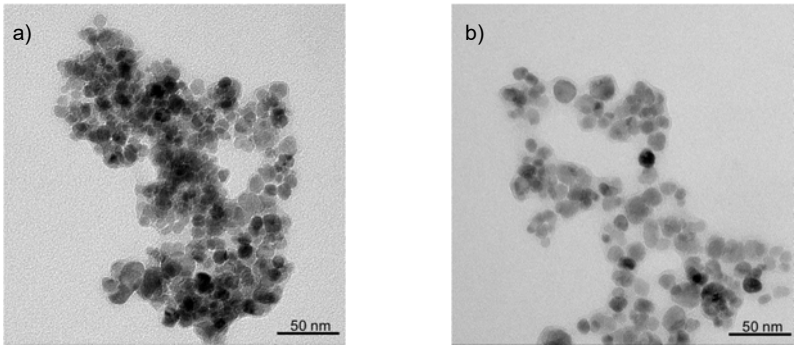

Figure 3.23. TEM images of a) FeNPs and b) FeNPs-TEM.

Conductimetric titration was then used to calculate the amount of -COOH groups on the surface of FeNPs-TEPSA (**Figure 3.24**, more details in experimental section, Appendix). This technique is based on the replacement of one ion by another and invariably these two ions differ in the ionic conductivity during the titration. The equivalence point is the titration of the acid of the surface of FeNPs.[163] The amount of carboxylic groups was estimated as a molar ratio of 0.65 mmol·g^{-1} carboxylic functions compared to the total iron content.

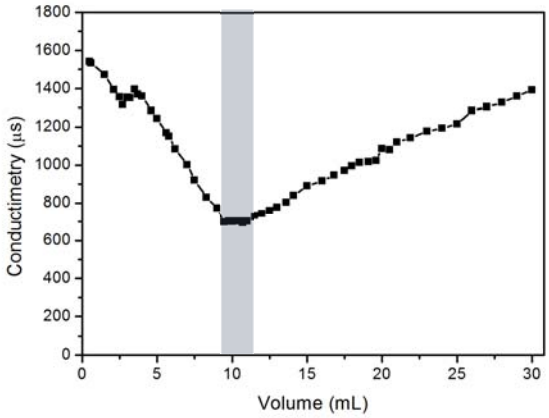

Figure 3.24. Conductimetric titration of FeNPs-TEPSA nanoparticles.

The presence of carboxylic groups allowed the attachment of CNDs, in order to combine FeNPs and fluorescent probes to make a hybrid system for MRI

applications. The CNDs were covalently grafted to the as-synthesized FeNPs-TEPSA nanoparticles by using EDC/NHS as a coupling agent. The uncoupled CNDs nanoparticles were eliminated by filtration and magnetic separation until no fluorescence was detected in the supernatant (**Figure 3.25**).

Figure 3.25. a) Schematic illustration of the functionalization of CNDs with FeNPs. b) Photography of the magnetic decantation of CNDs-FeNPs.

In **Table 3.3** is showed several attempts of reactions carried out to functionalized CNDs with FeNPs; different molar ratios of the materials and solvents were used. However, the attempts were unsuccessful, showing for each reaction a total quenching of the fluorescence emission.

Table 3.3. Optimization of the functionalization.

ENTRY	CNDs (equiv)	FeNPs-TEPSA (equiv)	SOLVENT
1	1	0.3	PBS pH 7.5
2	1.5	1	DMF
3	1.5	1	DMF
4	10	1	DMF
5	1	10	DMF

The resulting characterization by FT-IR showed the attachment of FeNPs onto the surface of the dots. The **Figure 3.26** (black line), showed the appearance of the band at 1700 cm^{-1} from amide bond, confirming the covalent attachment of the FeNPs. Moreover, the spectrum exhibited a decreased from N-H stretching vibrations in the range 3000-3500 cm^{-1} and the appearance of the peak at 582 cm^{-1} from Fe–O bonds in FeNPs.

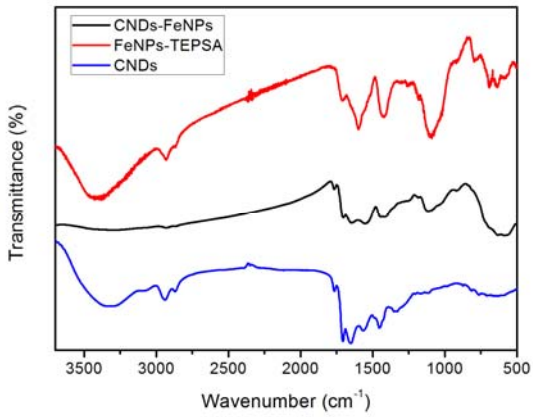

Figure 3.26. FT-IR spectra of CNDs, FeNPs-TEPSA and CNDs-FeNPs hybrid.

The optical properties of the hybrid were studied. The UV-Vis spectra did not display almost any absorption from the system (**Figure 3.27a**). Moreover, the most important feature of CNDs, which is the fluorescence it was quenched. The decrease of the fluorescence could be due to the proximity with the FeNPs and maybe energy transfer process could occur (**Figure 3.27b**).

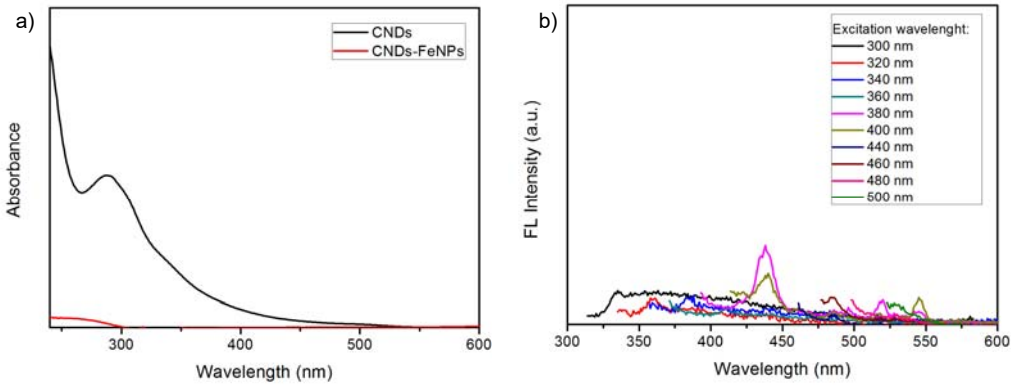

Figure 3.27. a) UV-Vis spectra of CNDs hybrid with FeNPs-TEPSA in water. b) Fluorescence emission spectra at different excitation wavelengths of CNDs hybrid with FeNPs-TEPSA, **16** in water.

Another step within CNDs functionalization with FeNPs was avoid the quenched of the CNDs fluorescence. Due to this, a linker between CNDs and FeNPs was used. Previously, it was synthesized FeNPs-linker, which gave to FeNPs biocompatibility and more solubility. The synthesis of monoprotected amine **19** was prepared following literature procedures and is fully described in the section dedicated to

experimental details.[164] Afterwards, the iron nanoparticles with TEPSA were functionalized with the linker **20** *via* carbodiimide chemistry (**Figure 3.28**).

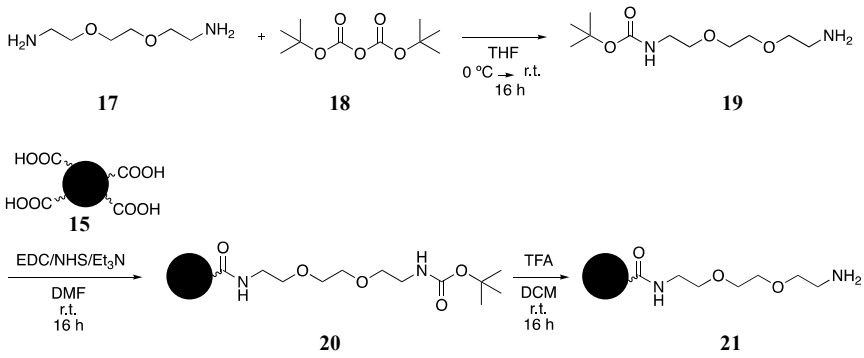

Figure 3.28. Synthesis of the desire linker-FeNPs, **21**.

It was chosen FeNPs-linker with terminal amines in order to attached onto the surface of CNDs *via* cardiimide chemistry, thanks to the acids that CNDs present (see Chapter 2). These functional groups in comparison with amines are minority, due to this we could explored insignificant modifications on the optical properties of CNDs. Even if we have used previously a low amount in the molar ratio between CNDs: FeNPs. As before, the functionalization between CNDs and FeNPs-linker linker was carried out with EDC/NHS as coupling agents. Therefore, several amounts of nanoparticles were used in order to maintain the optical properties of CNDs.

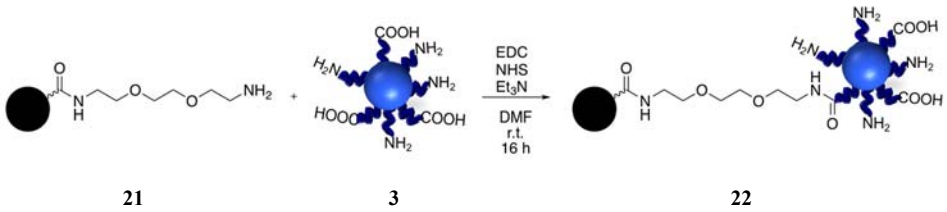

Figure 3.29. Schematic illustration of the functionalization of CNDs with FeNPs-linker.

Figure 3.30 showed the fluorescence spectra of the new hybrid. The intensity of the fluorescence emission was not enough for our applications. These hybrids have potential applications in MRI images and photothermal treatments. However, an increased in the fluorescent intensity is needed and it will be achieved with the used of non-flexible linkers between CNDs and FeNPs.

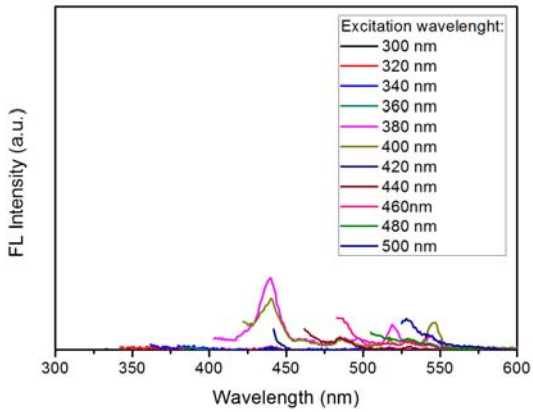

Figure 3.30. The fluorescence emission spectra at different excitation wavelengths of CNDs hybrid with FeNPs-linker, **22**.

3.3.1.2. Drugs

Drug delivery systems based on nanomaterials, could potentially reduce the side effects associated with several antineoplastic drugs, due to the reduction of the drug dose needed to achieve the therapeutic benefit (see Chapter 1 for more details). Moreover, carbon nanomaterials as CNDs due to their excellent properties, such as high water solubility and biocompatibility can enhanced permeation and retention effect of chemotherapeutic agents.[165] Herein in this section, we further apply CNDs as vehicle towards the improvement of solubility and drug delivery of the most common drugs, *via* covalent bond. Most of the drug delivery systems created up to now are based on non-covalent interactions in order to not change the chemical structure of the drugs.[166] Then, we have chosen carefully two drugs that can be covalently modified and the efficacy of the drugs is not changed as Paclitaxel and Chlorambucil.

Paclitaxel (PTX), a diterpenoid plant product extracted from the yew tree, *Taxus brevifolia*, is a microtubule polymerizing agent drug that is approved by the Food and Drug Administration for the treatment of ovarian, breast, and lung cancer, as well as Kaposi's sarcoma.[167] Moreover, PTX is on the World Health Organization's List of Essential Medicines, the most important medication needed in a basic health system for the treatment of many types of cancers and it is recognized as the most cost-effective chemotherapy drug.[168] The therapeutic effect of PTX is reported to be potent. It works through binding to microtubules inducing mitotic arrest, the major cell cycle control mechanism acting during mitosis to prevent chromosome missegregation. Thus, a signal transduction cascade is activated and delays mitotic progression by inhibiting the anaphase.[169,170] The PTX resistance may contribute to the consecutive recurrence and metastasis of cancer, finally causing death.[171] Although many studies have been conducted related to the paclitaxel resistance, the specific mechanisms of action involved are still poorly understood.[172] Nevertheless, there are many limitations due to its low water solubility. With the purpose of

improving aqueous solubility, PTX is formulated in a mixture of Cremophor EL®, polyethoxylated castor oil and dehydrated ethanol (50:50, v/v) in a combination known as Taxol®. However, Taxol® has several side effects related to Cremophor EL® and ethanol. Therefore, there is an urgent need to replace Cremophor EL® to deliver PTX with reduced adverse effects to healthy tissues.

Chlorambucil (CBL) commonly known as Leukeran® is a poor water soluble drug and potent anticancer cytotoxic warhead. Moreover, it is on the World Health Organization's List of Essential Medicines, the most effective and safe medicines needed in a health system.[168] CBL is used for the treatment of chronic lymphocytic leukemia, certain types of non-Hodgkin lymphoma, trophoblastic neoplasm and ovarian carcinoma.[173] This drug is an alkylating agent, a type of nitrogen mustards derived from mustard gas. The nitrogen mustard moiety in CBL is the most attractive part; once it enters in the cells this part becomes activated, and interferes in the replication of deoxyribonucleic acid (DNA), through the alkylation of nucleobases by forming aziridinium ion as an intermediate. Therefore, blocking cell division and resulting in apoptotic cell death.[174] In relation with their limitations as PTX there are many limitations due to its low water solubility. Therefore, there is an urgent need to increase the solubility of these drugs.

3.3.1.2.1. CNDs-PTX

The nanocarrier was obtained through covalent functionalization of CNDs with PTX. Before coupling with CNDs, PTX was modified with succinic anhydride at the 2'-hydroxyl position, to provide an acid group (**Figure 3.31**).[175] The esterification at the 2'-OH position resulted in the loss of binding to microtubules, but it did not affect its cytotoxicity possibly due to the hydrolysis of the ester group by intracellular esterases. Esterification at the 2'-OH position tends to promote water solubility. Due to the higher reactivity of the 2'-OH compared to the 7'-OH group, the product resulted from the 2'-OH derivatization was chosen to be attached onto the surface of the CNDs. The biproduct was removed by crystallization.[175]

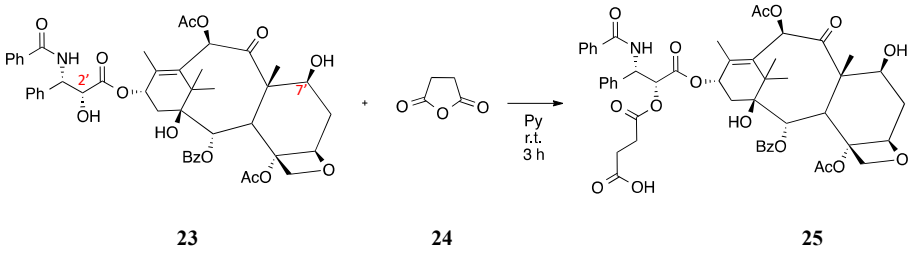

23 **24** **25**

Figure 3.31. Functionalization of PTX.

Afterwards, CNDs amino groups were functionalized with the acid-modified PTX *via* amide formation using EDC/NHS as coupling agents (**Figure 3.32**). The excess of organic molecules and the pristine CNDs were removed by size exclusion

chromatography. The covalent anchoring was validated by ^{1}H NMR, UV-Vis, FL and FT-IR spectroscopy.

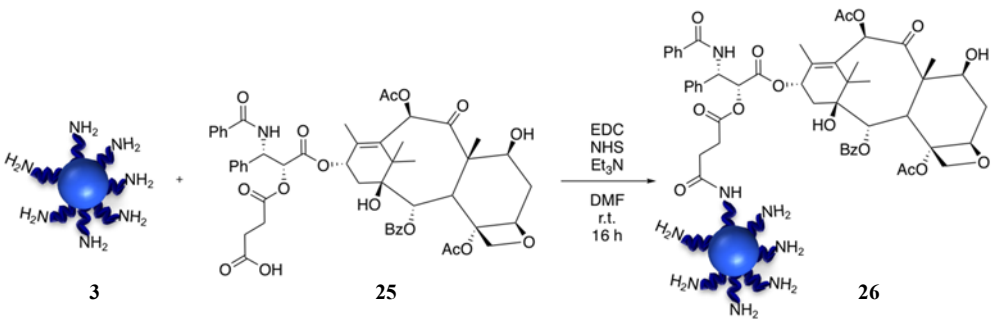

Figure 3.32. Schematic illustration of the functionalization of CNDs with PTX.

The ^{1}H NMR spectrum showed a peak around 5.25 ppm that corresponds to the amide group (**Figure 3.33**) thus confirming the functionalization. Furthermore, the very broad signal did correspond to this kind of groups.

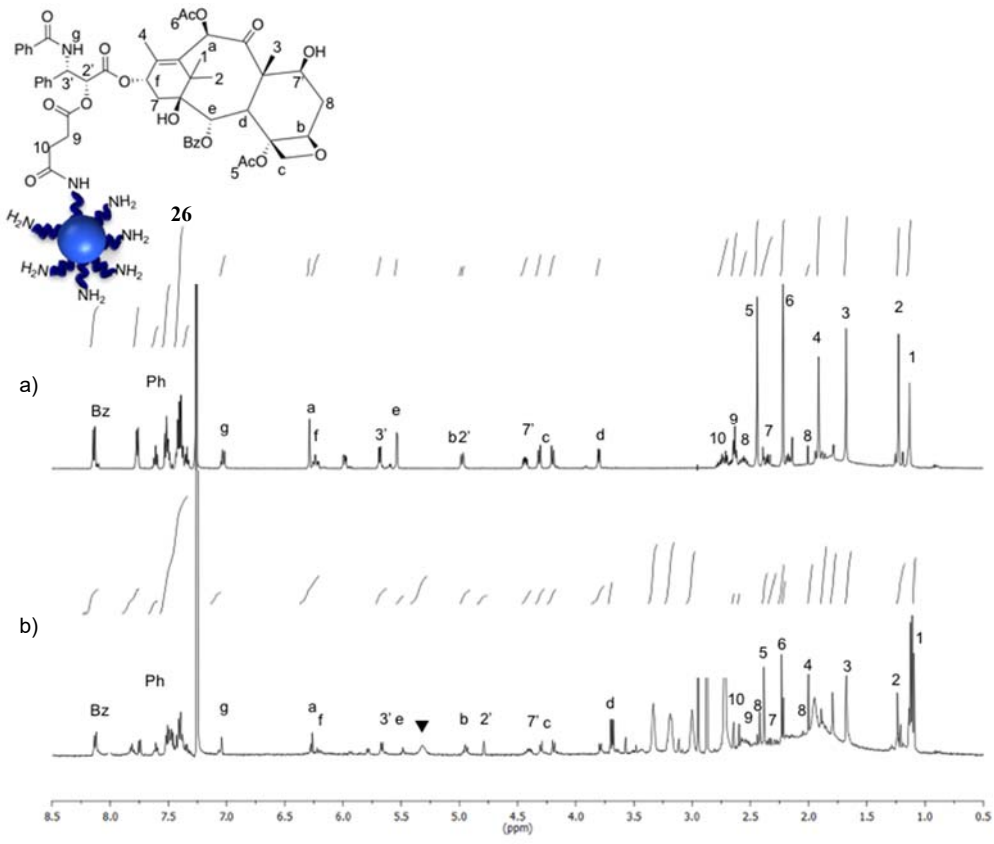

Figure 3.33. ^{1}H NMR of a) functionalized PTX, 25 and b) CNDs-PTX in $CDCl_3$.

The nanocarrier CNDs-PTX was characterized with FT-IR spectroscopy. The spectrum (**Figure 3.34**) showed the typical bands of pristine CNDs (see Chapter 2),[31] broad absorption bands in the range of 3500-3000 cm^{-1} corresponded to O-H and N-H stretching vibrations. The C–H stretching vibration was observed by the peaks at 2946 and 2866 cm^{-1}, while the peak at 1650 cm^{-1} was attributed to –C(O)-NH vibrations. Peaks in the range 1569-1354 cm^{-1} corresponded to a combination of a C–N stretching and N–H bending bands. Moreover, a new absorption peak of C–C stretching was observed from the PTX at 707 cm^{-1}. The presence of the peak at 1024 cm^{-1} further demonstrated that PTX was incorporated onto CNDs nanoparticles successfully. On the other hand, CNDs-PTX showed a decrease of the amino groups by Kaiser test (130 $\mu mol \cdot g^{-1}$) with respect to the pristine CNDs (1053 $\mu mol \cdot g^{-1}$).[41] Thus, indicating that PTX is loaded onto the surface of CNDs.

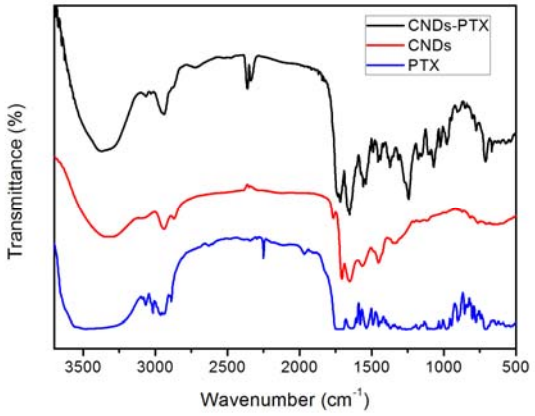

Figure 3.34. FT-IR spectra of CNDs-PTX, CNDs and PTX.

The optical properties were investigated with UV-Vis and FL spectroscopies (**Figure 3.35**). As shown in **Figure 3.35a**, a shift in the UV spectrum of the CNDs-PTX was observed, with respect to the pristine CNDs. The band at 290 nm could be due to the π-π* transition of the aromatic ring structure of the CNDs.[31] Moreover, the fluorescence spectrum of CNDs-PTX (**Figure 3.35b**) showed an excitation wavelength-dependent emission, as the pristine CNDs (see Chapter 2).

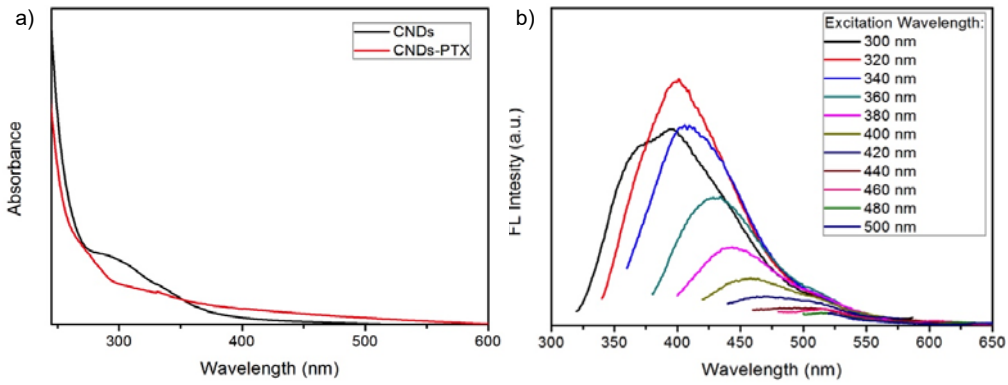

Figure 3.35. a) UV-Vis of CNDs and CNDs-PTX and b) FL spectra at different excitation wavelengths of CNDs-PTX in water.

The spectrum showed the maximum emission intensity at 402 nm, when excited at 320 nm. Furthermore, the emission was changed with respect to pristine CNDs (emission 365 nm, excitation 300 nm), and accompanied by shifts toward higher emission wavelengths, when increasing the excitation wavelength.

In order to determine the size and shape of the CNDs-PTX conjugate, atomic force microscope (AFM) was performed and showed spherical particles with a size distribution in the range between 3 nm and 9 nm, with an average size of 6.0 ± 1.6 nm, as determined by statistical analysis of 100 particles (**Figure 3.36**). It is noteworthy that an increase of the size, with respect to the pristine CNDs 3.7 ± 1.8 nm, was observed. As demonstrated with the aforementioned results, the functionalization of this nanomaterial occurred successfully.

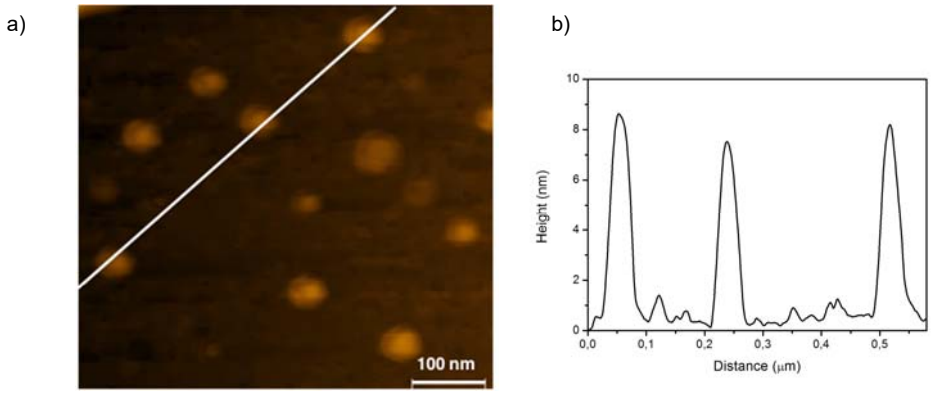

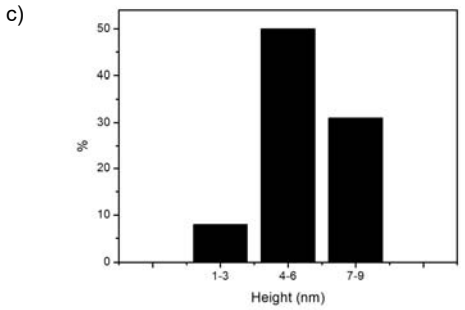

Figure 3.36. a) AFM image and b) height profile of CNDs-PTX nanocarrier and c) size histogram of CNDs-PTX.

A necessary issue to take into account was the amount of PTX loaded onto the CNDs surface. The amount of PTX attached on CNDs was first determined by thermal gravimetric analysis (TGA). It was performed to measure the thermal stability and the weight loss of the components (**Figure 3.37**). As controls, PTX and CNDs were first analyzed to measure the amount of each system before the coupling of the nanocarrier.[176] The weight loss of CNDs-PTX at 506 ºC in N_2 was 81 %, while CNDs and PTX had a 79 % and 82 % weight loss at 506 ºC in N_2, respectively. Thus, CNDs-PTX nanosystem was observed to contain about 34 wt % of CNDs and 66 wt % of PTX according to the following **Equation 3.1**, **3.2** set (x and y are the weight percentage of CNDs and PTX, respectively).

Equation 3.1 $0.79x + 0.82y = 0.81$

Equation 3.2 $x + y = 1$

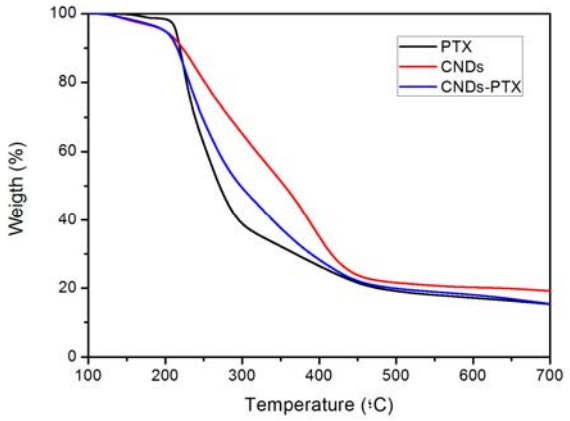

Figure 3.37. TGA of PTX, CNDs, and CNDs-PTX with a heating rate of 10 ºC·min^{-1} in N_2.

Moreover, matrix-assisted laser desorption ionization (MALDI) was used to ascertain the results from TGA. In the nanosystem (CNDs-PTX) the molecular weight of CNDs was 900.5 Da (green line, **Figure 3.38**) and the total weight of the conjugate was 2465.9 Da (blue line, **Figure 3.38**), then the amount of CNDs represented

900.5/2465.9 = 0.4. Accordingly, the molecular weight of CNDs in a mg of nanosystem was 0.4 mg and 0.6 mg of PTX. Thus, CNDs-PTX nanosystem was observed to contain approximately 2 PTX for a single CND. Therefore, MALDI showed that the amount of PTX loaded on CNDs was calculated to be about 0.6 mg per 1.0 mg of sample (**Figure 3.38**). This result is in good accordance with the estimation based on the TGA data.

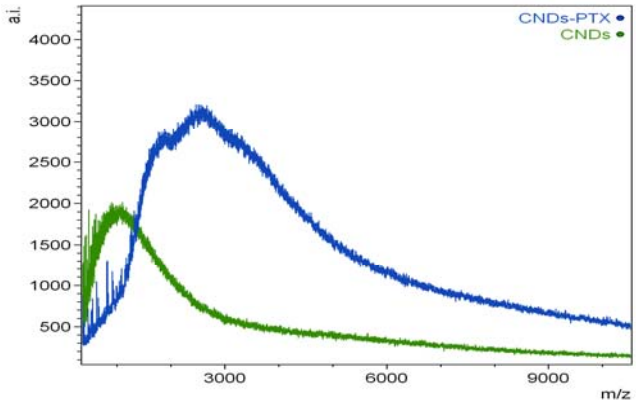

Figure 3.38. MALDI spectra of CNDs and CNDs-PTX.

3.3.1.2.2. CNDs-PTX-Cy5

Previously, it was commented in the section 3.3.1.1 organic molecules; CNDs-Cy5 that CNDs emission overlaps with several dyes that are necessary to measure the cellular apoptosis. Thus, CNDs-Cy5 was synthesized to be the control of non-toxicity and to confirm that CNDs-PTX is responsible for the apoptosis due to the drug attached. Then, Cy5 label was introduced in order to differentiate CNDs-PTX from nuclear counterstains (**Figure 3.39**).

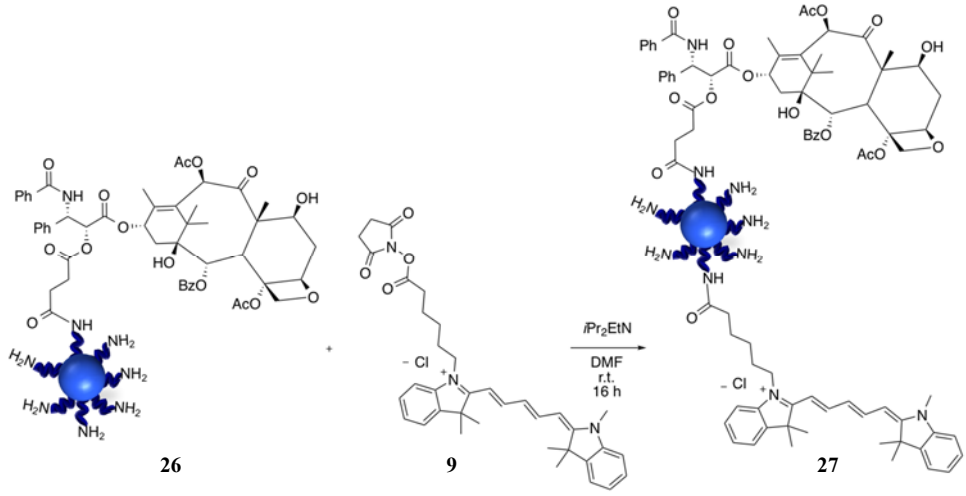

Figure 3.39. Scheme modification of CNDs-PTX with Cy5.

The optical properties were investigated with UV-Vis and FL spectroscopies (**Figure 3.40**). As showed in **Figure 3.40a**, the UV spectrum of the CNDs-PTX-Cy5 is composed by a shoulder in the 250-350 nm range, attributed to CNDs and the 550-680 nm range, from Cy5 dye. Moreover, the fluorescence spectrum of CNDs-PTX-Cy5 plotted in **Figure 3.40b** showed also excitation wavelength-dependent emission as CNDs-PTX (see, **Figure 3.35**) and the emission at 660 nm from Cy5.

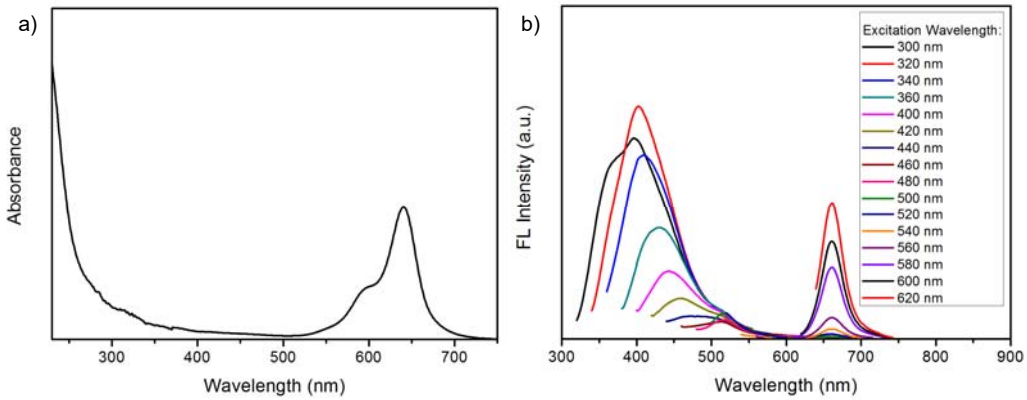

Figure 3.40. a) UV-Vis spectra and b) FL spectra at different excitation wavelengths of CNDs-PTX-Cy5 in water.

The FT-IR spectrum of CNDs-PTX-Cy5 (**Figure 3.41**) showed the characteristic bands of CNDs-PTX, such as O–H or N–H stretching vibrations in the range 3000-3500 cm^{-1} and the absorption peak of C–C stretching from the PTX at 707 cm^{-1} and 1024 cm^{-1} (see, **Figure 3.34**). The C–H stretching vibration was showed by the peaks at 2946 and 2866 cm^{-1}, while the peaks between 1550 and 1750 cm^{-1} were attributed to C=O, C=N and N–H vibrations. Peaks in the range 1330-1480 cm^{-1} corresponded to a combination of a C–N stretching and N–H bending bands.[16,17]. Moreover, the spectrum of CNDs-PTX-Cy5 showed a new band at 977 cm^{-1}, indicating that Cy5 was introduced onto the CNDs-PTX system, given a new system of CNDs-PTX-Cy5 successfully.

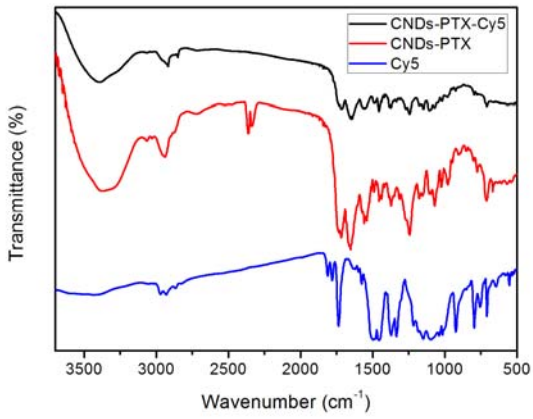

Figure 3.41. FT-IR spectra of CNDs-PTX, Cy5 and CNDs-PTX-Cy5.

AFM images (**Figure 3.42**) did not give more information about the functionalization of the as-prepared system, since the size of the CNDs-PTX-Cy5 it was approximately the same of the as-prepared CNDs-PTX. This could be related to the low amount of Cy5 used in the reaction, as in the CNDs-Cy5 system.

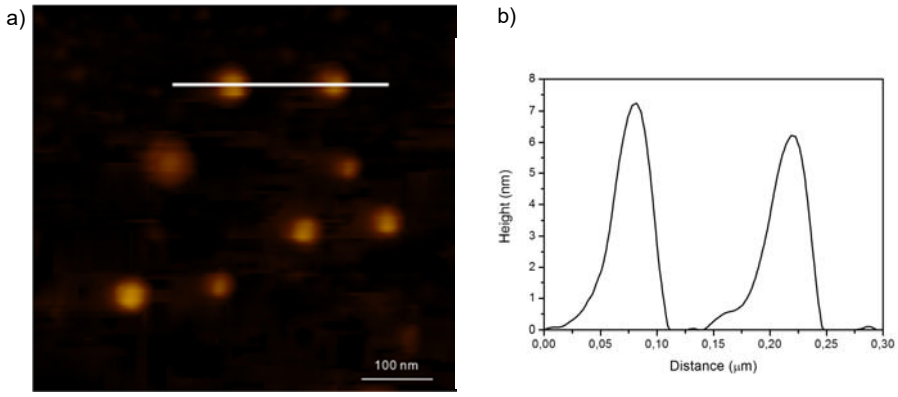

Figure 3.42. a) AFM image and b) height profile along the line of CNDs-PTX-Cy5.

3.3.1.2.3. CNDs-CBL

The nanocarrier was obtained through a covalent amide bond formation between CNDs amino groups and with CBL carboxylic groups (**Figure 3.43**). Size-exclusion chromatography of the nanocarrier-drug was performed in order to separate the system with maximum coverage of CBL onto the CNDs surface.

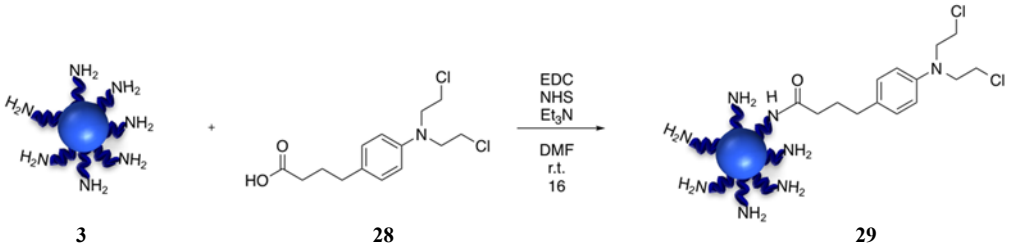

Figure 3.43. Schematic representation of the synthesis of the nanocarrier, CNDs-CBL.

The covalently anchoring was validated by NMR, UV-Vis, FL, FT-IR spectroscopy and XPS. The ^{1}H NMR spectrum showed a peak around 5.6 ppm that corresponds to the amide groups (**Figure 3.44**), thus directly indicating that CBL is loaded on the surface of CNDs. Furthermore, the shape of the signal did correspond to these kinds of group.

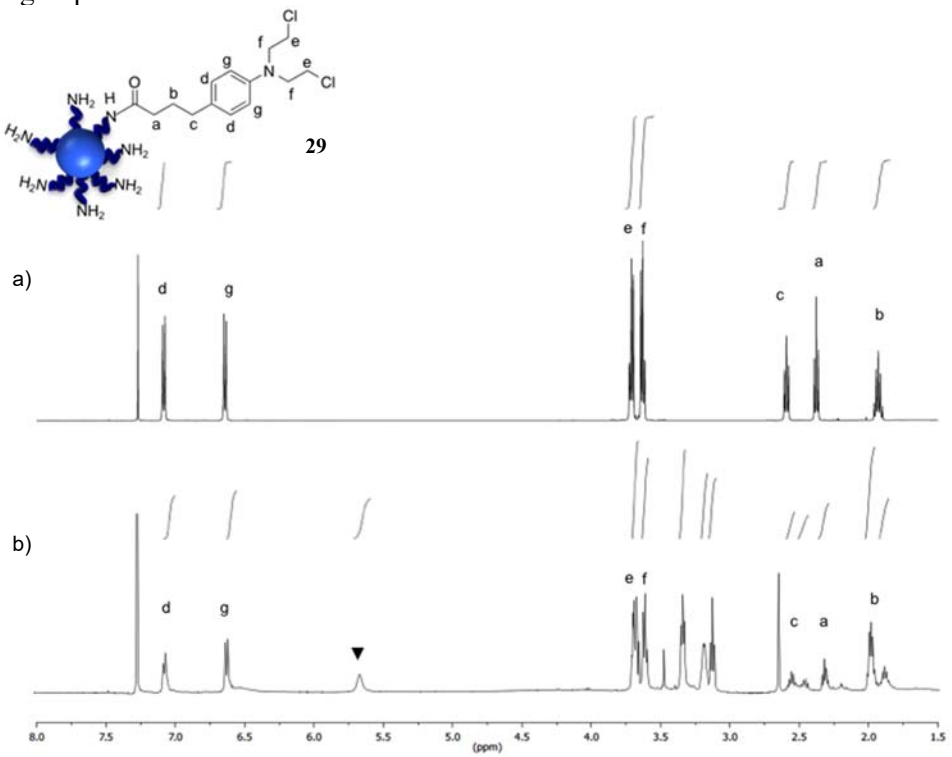

Figure 3.44. ^{1}H NMR of a) CBL and b) CNDs-CBL in $CDCl_3$.

The surface functional groups of the CNDs-CBL nanocarrier were characterized by FT-IR spectroscopy. The spectrum (**Figure 3.45**) exhibited the broad absorption bands of O-H and N-H in the range of 3000-3500 cm^{-1}, C=O, N-H and C=N at 1550-1750 cm^{-1} from CNDs.[177,178] Moreover, a new peak appeared at 2500–2800 cm^{-1} from aromatic C–H stretching bands, indicating that CBL was loaded onto the surface of

CNDs successfully. Furthermore, CNDs-CBL showed a decrease in the intensity of the N-H bending and C-N bands, to 1569 cm^{-1} and 1354 cm^{-1}, respectively, compared to the pristine, as well as an increase in the (O=C-NH) vibration band at 1650 cm^{-1}, thus indicating that CBL is loaded onto the surface of CNDs through amide bonds. In addition, such findings were also supported by KT,[41] which showed a decrease of the amino groups of CNDs-CBL (139 $\mu mol \cdot g^{-1}$) with respect to the pristine CNDs (1023 $\mu mol \cdot g^{-1}$).

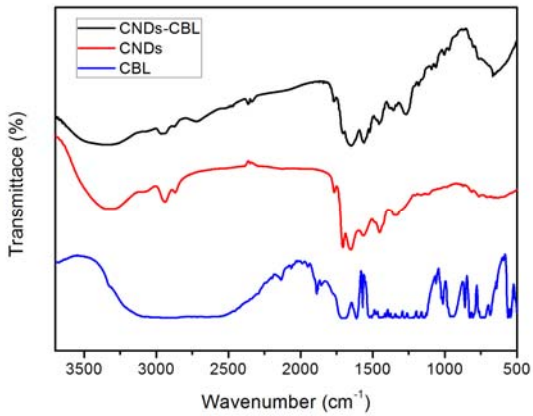

Figure 3.45. FT-IR spectra of the CNDs-CBL, CNDs and CBL.

The optical properties were investigated with UV-Vis and FL techniques. As shown in **Figure 3.46**, a shift in the UV spectrum of the CNDs-CBL in the 290-325 nm range was observed, with respect to the pristine CNDs. CNDs-CBL presented the bands from CBL and a broad absorbance from 325 to 425 nm. Moreover, the fluorescence spectrum of CNDs-CBL was excitation wavelength-dependent, in accordance to the fluorescence properties of pristine CNDs. On the other hand, the maximum excitation wavelength was increased from 300 nm to 320 nm. The photoluminescence quantum yield (QY) exhibited was evaluated as 11%, at 320 nm of excitation.[135]

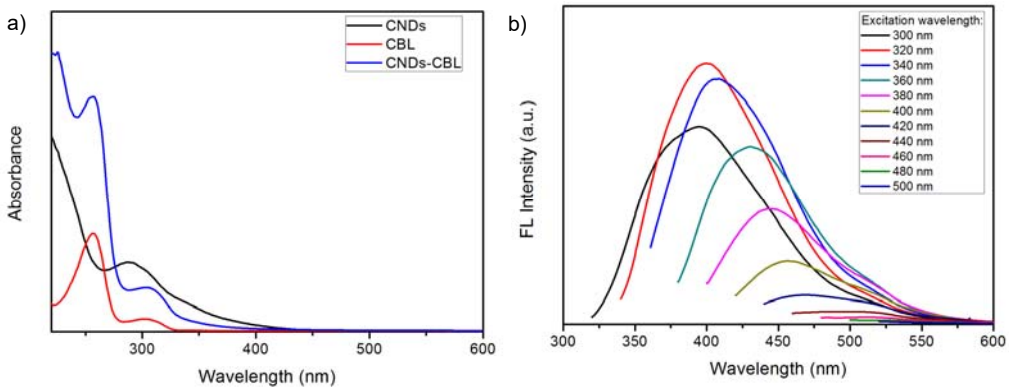

Figure 3.46. a) UV-Vis of CNDs, CBL and CNDs-CBL spectra. b) Fluorescence spectra at different excitation wavelengths of CNDs-CBL nanocarrier in water.

Moreover, the studies carried out by XPS demonstrated that the pristine CNDs contained mainly elemental carbon, nitrogen and oxygen, having 68, 16 and 16 atom %, respectively,[31] whereas the CNDs-CBL displayed also the presence of chlorine (5 %), apart from carbon (74 %), nitrogen (12 %) and oxygen (9 %), as shown in **Figure 3.47**. It is noteworthy that the pristine CNDs did not present chlorine atoms (see, Chapter 2), thus confirming the successful attachment of the drug onto the CNDs surface.

a)

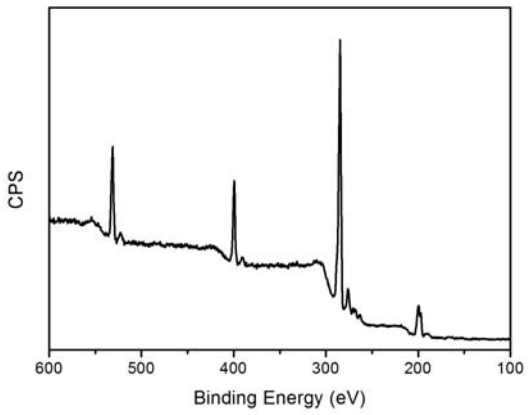

b)

Cl 2p	**200.5 eV**	**5%**
C 1s	**283.4 eV**	**74%**
C-C/C-H	284.8	58.7
C-O/C-N	286.1	30.0
C=N/C=O	287.9	5.4
COOH	288.8	5.9
N 1s	**397.7 eV**	**12 %**
N=C	397.9	4.0
NH_2	399.7	66.4
C-N-C	400.05	18.9
$N-C_3$	401.9	10.7
O 1s	**528 eV**	**9 %**
O=C	531.7	76.9
O-C	533.2	23.1

Figure 3.47. a) XPS survey spectrum of the CNDs-CBL nanocarrier. b) Binding energy and percentage of Cl, C, N, and O atoms in CNDs-CBL as determined by XPS measurements.

In order to determine the size and shape, atomic force microscope (AFM) images revealed that CNDs-CBL were composed of small spherical particles with a size distribution in the range between 3 nm and 9 nm, with an average size of 6.2 ± 1.4 nm, determined by statistical analysis of 100 particles. Interesting, it was found that our nanocarrier had a very strong tendency of self-aggregation during the AFM preparation (**Figure 3.48**).

a)

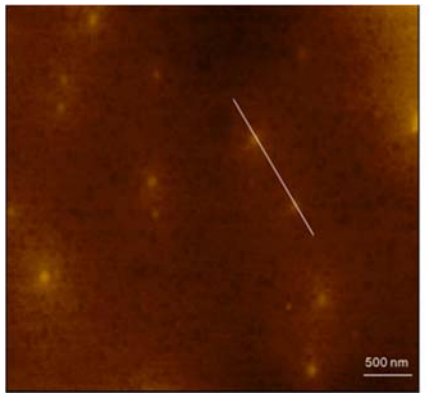

b)

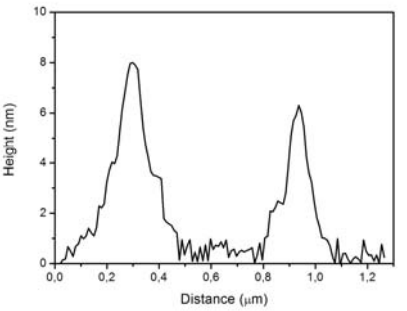

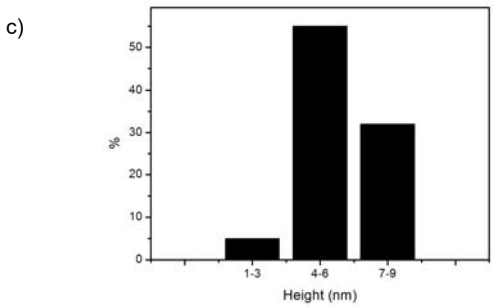

Figure 3.48. a) AFM of CNDs-CBL image. b) Height profile corresponding to the line drawn in a) and c) size histogram of CNDs-CBL.

The quantification of drug loading is crucial to compare the efficiency of the system with the drug alone. The amount of CBL attached on the CNDs was first determined by thermal gravimetric analysis (TGA). The thermal stability and the weight loss of the components were measured (**Figure 3.49**). As controls, CBL and CNDs were first analyzed to measure the amount of each system before the coupling with the nanocarrier.[176] The weight loss of CNDs-CBL at 284 ºC under N_2 was 33 %, while CNDs and CBL had both around 33 % and 32 % weight loss at 284 ºC under N_2. Thus, CNDs-CBL nanocarrier was evaluated to contain about 50 wt % of CNDs and 50 wt % of CBL according to the following **Equation 3.3**, **3.4** set (x and y are the weight percentage of CNDs and CBL, respectively).

Equation 3.3 $0.33x + 0.32y = 0.33$

Equation 3.4 $x + y = 1$

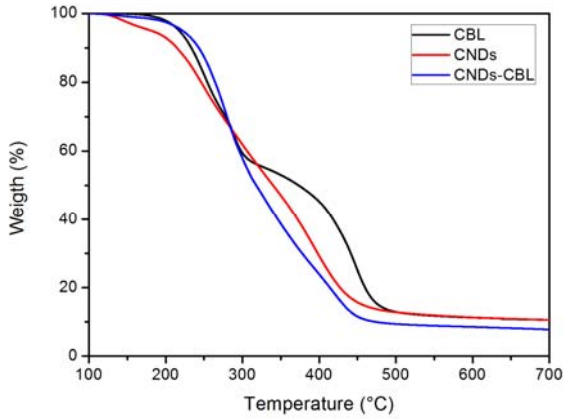

Figure 3.49. TGA curves of the CBL, CNDs and CNDs-CBL samples in N_2 atmosphere.

Moreover, matrix-assisted laser desorption ionization (MALDI) showed that the amount of CBL loaded on the CNDs was 0.50 g per 1 g of sample, approximately (**Figure 3.50**). This result is in good accordance with the estimation based on the

TGA data. In the nanosystem (CNDs-CBL) the molecular weight of CNDs was 900.5 Da (green line, **Figure 3.50**) and the total weight of the conjugate was 1727.1 Da (blue line, **Figure 3.50**), then the amount of CNDs represented 900.5/1727.1 = 0.5. Accordingly, the amount of CNDs in a mg of nanosystem was 0.5 mg and 0.5 mg of CBL. Thus, CNDs-CBL nanosystem was observed to contain approximately 3 CBL for a single CND.

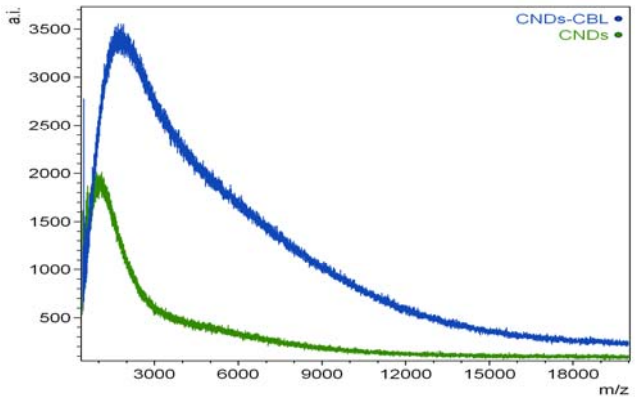

Figure 3.50. MALDI spectra of CNDs and CNDs-CBL.

3.3.2. Non-covalent functionalization

3.3.2.1. Proteins

3.3.2.1.1. CNDs-HSA

Being aware of the promising future of carbon nanodots in biological and biomedical applications, understanding and unrevealing their physiological response when they are in contact to biological fluids, as well as cell culture medium, is a critical issue to address.

Proteins, such as human serum albumin (HSA) present in biological systems can be adsorbed on the surface of the nanoparticles forming the so-called protein corona (PC), which modulates the biologically significant entity and strongly governs the ultimate cell–NP interactions.[179] Therefore, PC has a significant role in cellular response of the nanoparticles. The composition of the protein corona may vary significantly between different nanomaterials and depends on many parameters,[180] a full prediction is not possible yet, even working with nanoparticles belonging to the same family as for example carbon-based nanomaterials (*i.e.* carbon nanotubes, graphene, carbon nanodots). Studies of the effect of fetal bovine serum (FBS)-proteins on the cellular uptake and cytotoxicity of CNTs and graphene oxide (GO) have been reported.[181,182] Nevertheless, the physicochemical properties of CNTs and GO are so different to those of CNDs, not only in size and shape but also in the functional surface groups, that the protein-CNDs and cell-CNDs interactions in the presence or in the absence of a preformed protein corona cannot be predicted in a

straight-forward way, and they should be studied on a case-by-case even for different types of CNDs.

At this point it is where studying the protein corona formation around carbon nanodots (PC-CNDs) comes into play, because this will be the biological entity that cells will "*see*" once that the CNDs are into the bloodstream. To investigate this, the as synthesized CNDs were modified with a natural (see Chapter 4) or an artificial protein corona. The formation of an artificial corona on the CNDs was carried out by coating them with HSA via adsorption (**Figure 3.51**). HSA was selected for the formation of a model protein corona owing to its high abundance in biological fluids such as blood, and therefore trying to mimic the situation which will happen when CNDs are used in real bioapplications. In order to be able to follow the protein corona by fluorescence techniques, HSA was labeled with the fluorescent Cy7 dye before being attached to the dots. Cy7 was the selected dye with the aim of avoiding the spectral overlapping between the CNDs emission and the Cy7 absorption. Thus, energy transfer effects were ruled out and no decrease of the fluorescence of the CNDs after the formation of the HSA-Cy7 protein corona was observed.

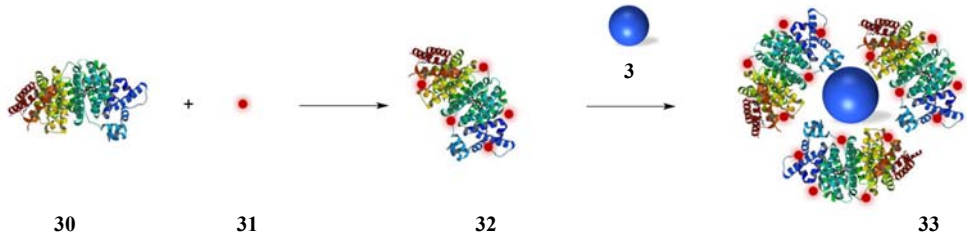

Figure 3.51. Formation of an artificial protein corona with labeled HSA protein (HSA-Cy7@CNDs).

The amount of HSA-Cy7 adsorbed onto the CNDs was optimized to get the maximum coverage while maintaining a good colloidal stability of the resulting complex. The HSA protein bound to the CNDs under optimized conditions and was quantified by the colorimetric Bradford assay, resulting in 280 ± 13 μg of HSA per mg of CNDs. The formation of the protein corona around the CNDs was also confirmed by DLS observing an increase of the hydrodynamic diameter from 8.3 ± 0.7 nm for the pristine CNDs to 17.2 ± 1.1 nm after the coating with the HSA-Cy7. Moreover, AFM revealed that the size of HSA-Cy7@CNDs increased significantly in comparison to the pristine CNDs but maintaining a spherical morphology, obtaining an average diameter of 11.8 ± 2.5 nm (**Figure 3.52**). Such large increase seems to indicate that the protein covers the whole surface of CNDs

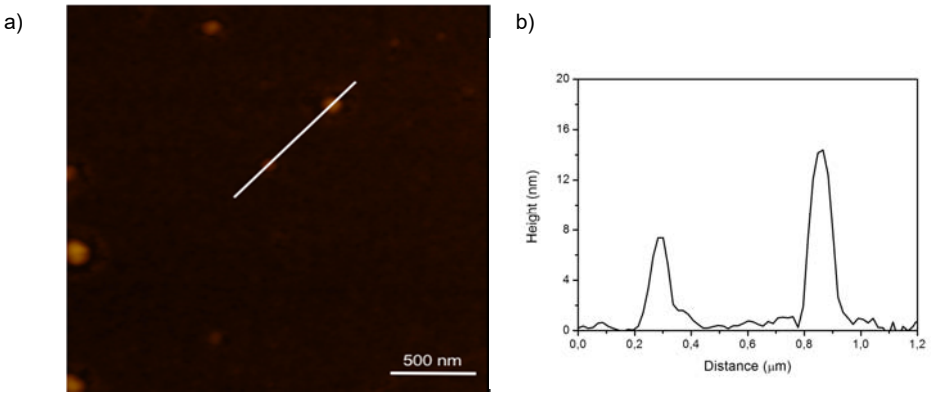

Figure 3.52. a) AFM topography image of HSA-Cy7@CNDs on a mica substrate, and the corresponding b) height-profile analysis along the line.

The zeta potential also changed dramatically at pH 7.4, from a positive surface charge +5.4 ± 1.4 mV to a negative charge -20.2 ± 2.1 mV, due to the fact that the HSA protein has an isoelectric point of 4.8, and therefore, provide a net negative charge at physiological pH (7.4). This change in the surface charge of the CNDs after the HSA-Cy7 protein corona formation was also supported by gel electrophoresis. The **Figure 3.53** upon visible and ultraviolet light illumination of 1.5 % agarose gels was taking after running the CNDs and those coated with the artificial corona (HSA-Cy7@CNDs). CNDs migrated to the negative pole indicating that they were positively charged. Contrarily, HSA-Cy7@CNDs migrated to the positive pole because they had negative charge on their surface

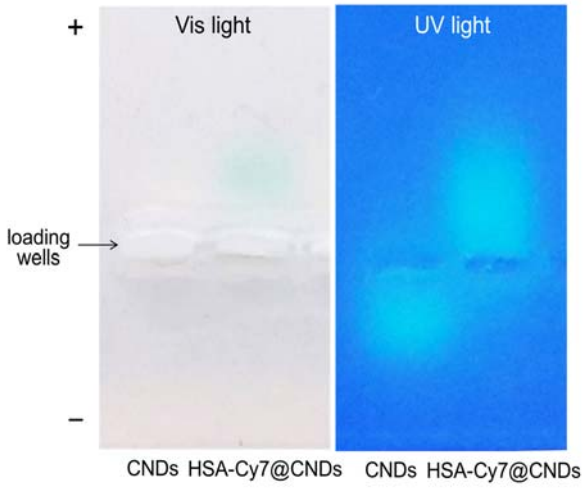

Figure 3.53. Images upon visible (Vis) and ultraviolet (UV) light illumination of 1.5 % agarose gels of CNDS and HSA-Cy7@CNDs.

The nanosystem HSA-Cy7@CNDs was characterized with FT-IR spectroscopy. In FT-IR spectrum appeared new bands, mainly in the range 500-1000 cm^{-1} (**Figure 3.54**), corresponding to the protein, which also confirmed the modification of CNDs after the formation of the protein corona. Moreover, the black spectrum showed the characteristics bands from CNDs (see, Chapter 2).

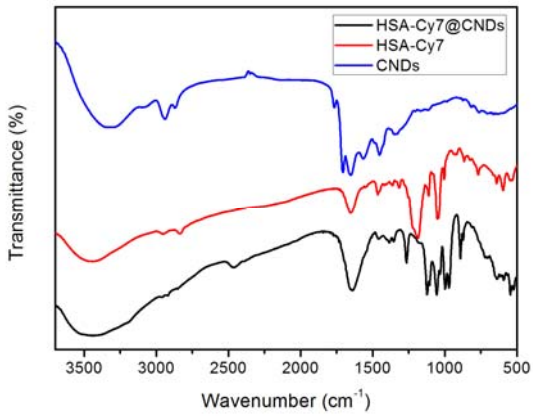

Figure 3.54. FT-IR spectra of HSA-Cy7@CNDs, HSA-Cy7 and CNDs.

The optical properties of the as-prepared HSA-Cy7@CNDs sample were studied. As shown in **Figure 3.55a**, UV-Vis spectrum presented a broad absorption band from 300 to 450 nm from the CNDs but the absorption edge at around 275 nm which was observed in the naked CNDs disappeared, and additionally it appeared the band at 750 nm from the Cy7. Moreover, its fluorescence emission showed also the excitation-dependent behavior due to the CNDs (**Figure 3.55b**).

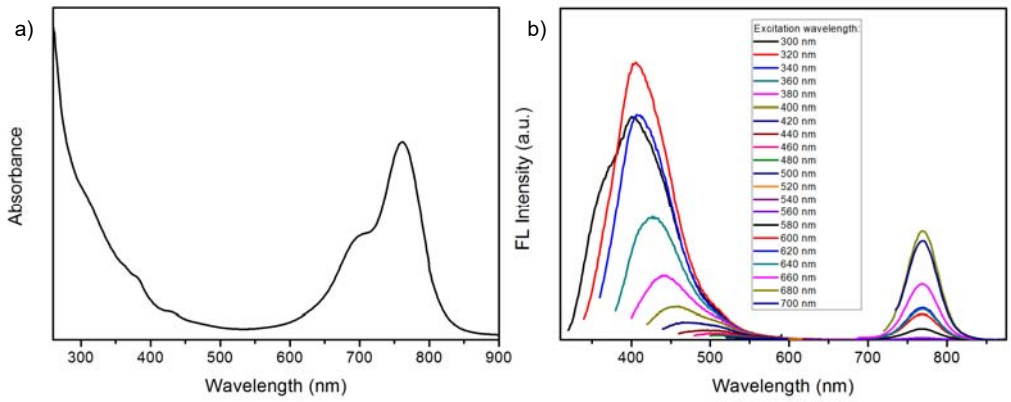

Figure 3.55. a) UV-Vis spectra and b) FL spectra of HSA-Cy7@CNDs in H_2O.

Interestingly, it was observed that the protein corona increased the photostability of the CNDs (**Figure 3.56**). Under continuous UV-irradiation at 300 nm with the excitation lamp, the fluorescence of the naked CNDs decreased steadily caused by a photochemical process as it has been already reported.[183] However, such photobleaching was minimized after coating with the HSA-Cy7, which indicates that the protein corona protected partially the CNDs from photo-oxidation and/or changes in their surface states.

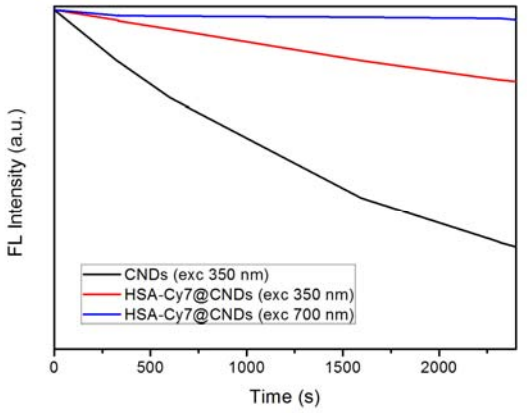

Figure 3.56. Photostability of the fluorescence emission of CNDs, and both emissions from CNDs and Cy7 of the HSA-Cy7@CNDs, under continuous UV-irradiation at 350 and 700 nm with the fluorimeter excitation lamp.

3.4. Conclusions

In the first part of this chapter, the surface modification of CNDs was performed with a DEG derivative and maleimide groups, and a studied of equivalents was done in order to study the behavior of the increased of the equivalent on the CNDs properties. Moreover, different methods of purification were assessed.

Furthermore, the previous study was used to predict the sequential functionalization extend to FeNPs, drugs and proteins, such as increased of the size, decrease of the QY and shifts on their FL properties. Particular attention has been placed on the calculation of the loading of the drugs, by TGA and MALDI techniques. Besides, the quantification of the protein HSA adsorbed onto the surface of CNDs by Bradford assay.

Finally, the hybrid nanomaterials accomplish the requirements for their use in biological applications, such as maintained of the water solubility, attachment of the desire molecules, drugs and proteins. Moreover, it was confirmed that the nature of pristine CNDs was modified in each functionalization.

CHAPTER 4

Bioapplications

CHAPTER 4

Bioapplications

"Biologist must constantly keep in mind that what they see was not designed but rather evolved." Nobel Laureate Dr. Francis Crick

4.1. Introduction

Carbon NanoDots are increasingly considered for biomedical applications such as biosensing,[83] cellular imaging,[84] drug delivery,[85] and theranostics due to their fascinating features such as water solubility, low toxicity,[59,86] biocompatibility, ease of functionalization, chemical stability, and unique photoluminescent properties*, e.g.*, tunable fluorescence emission and excitation-dependent fluorescence emission.[87] Their excitation-dependent fluorescent emission behavior provides a range of possible excitation wavelengths and minimizes the biological background by increasing the Stokes shift. Despite these interesting properties and that diverse studies have attempted to exploit these nanomaterials for bioapplications, the latter are still in their infancy since their physiological response is not well understood or controlled yet. Indeed, there is a gap in the literature regarding the understanding of the interaction of CNDs with biological systems (*e.g.* cells, cellular medium, blood, plasma or serum proteins), although this issue is a key factor for their use in bioapplications both from an efficacy and a safety point of view.[184]

Nowadays, it is well known that proteins present in biological systems can be adsorbed on the nanoparticles (NP) surface forming the so-called protein corona (PC), which becomes a biologically significant entity governing the ultimate cell–NP interactions.[179] It is well recognized that protein corona play a significant role in the cellular response to nanoparticles, and affects not only their cellular uptake but

changes also their trafficking and *in vivo* biodistribution, circulation lifetime, signaling, kinetics, transport, accumulation, and toxicity.[185,186] The composition of the PC is unique to each nanomaterial and depends on many parameters. For that reason, the results obtained for one particular nanoparticle cannot be extrapolated to other nanoparticles, even when working with nanomaterials of the same family as for example carbon-based nanomaterials (*i.e.* carbon nanotubes, graphene, carbon nanodots). Therefore, even if the future of CNDs in the biomedical field is promising in light of the results of the earliest approaches based on CNDs,[52,187,188,189] there is an urgent need of investigating the influence of the protein corona formed around CNDs on their performance as tools for a myriad of potential up-and-coming bioapplications.

CNDs must be studied from the beginning, from the first interaction with cell medium, cell interactions and their behavior until the final bioapplication. This chapter collects all this information, and their use as drug delivery systems, bioimaging agent and nanocarrier to cross the blood brain barrier (BBB).

4.2. Aim of the work

In this chapter, the interaction between cells and CNDs will be described with the help of the model of PC@CND that was described in Chapter 3 (This work was done in collaboration with Dr. Carolina Carrillo Carrion). Moreover, the use of CNDs and the CNDs-drugs, CNDs-PEGs hybrid (whose synthesis and characterization were described in Chapters 2 and 3) for several bioapplications will be discussed.

Figure 4.1 presents the general design followed in this chapter: from the study of the cell interaction with CNDs or PC@CND (as illustrated on the left) and drug delivery and bioimaging applications, followed by the CND capability to act as bionanocarriers and cross the blood brain barrier (as depicted on the right).

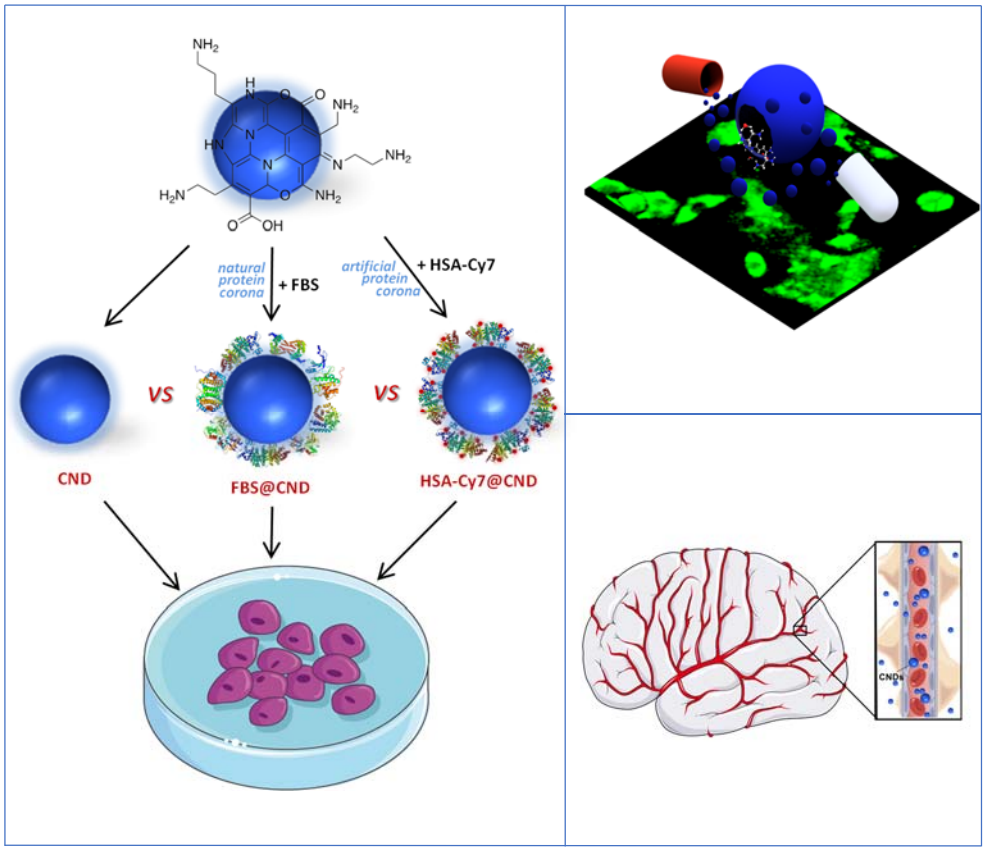

Figure 4.1. General design of cell-CNDs interactions and their use in drug delivery, bioimaging and as bionanocarrier to cross the blood brain barrier.

4.3. Results and discussion

In this section, the potential use of CNDs in biological systems will be described. After the understanding of the CNDs behavior in cells, the CNDs bioapplications will be discussed.

4.3.1. Influence of CNDs on biological systems

In order to assess the possible use of CNDs in bioapplications, their stability under cell growth conditions was tested. CNDs were incubated at 37 ºC and 5 % CO_2 in cell culture dulbecco's modified eagle medium (DMEM) completed with 10 % heat-inactivated fetal calf serum (FBS) for 0 h, 24 h, 48 h and 72 h. The dots were analyzed by UV-Vis measurements in order to ascertain for any significant changes in the absorption spectrum.[190] As reported in **Figure 4.2**, no significant evidences of instability in the cell culture medium were observed.

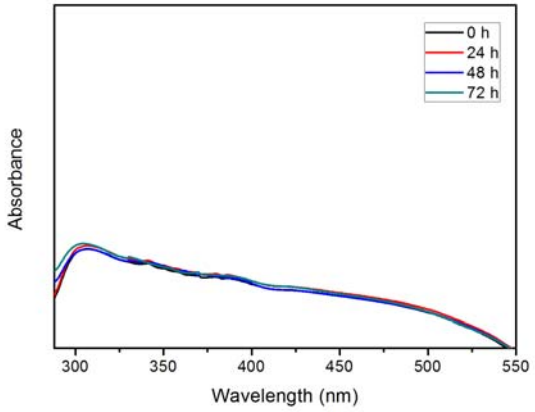

Figure 4.2. UV-Vis spectrum of CNDs incubated in complete DMEM for 0 h, 24 h, 48 h and 72 h at 37 ºC and 5 % CO_2 in a humidified atmosphere.

Moreover, the CNDs biocompatibility was tested by the 3-(4,5-dimethylthiazol-2-yl)-2,5-diphenyltetrazolium bromide (MTT) colorimetric assay.[191] The viability of several cell lines was found to change between 80-100 % after 72 h of incubation by using concentrations of CNDs ranging from 1 $\mu g \cdot mL^{-1}$ to 1 $mg \cdot mL^{-1}$ (**Figure 4.3**). The observed low cytotoxicity is in agreement with previous reported data,[192,193] and represent a fundamental characteristic for the use of CNDs in bioapplications.

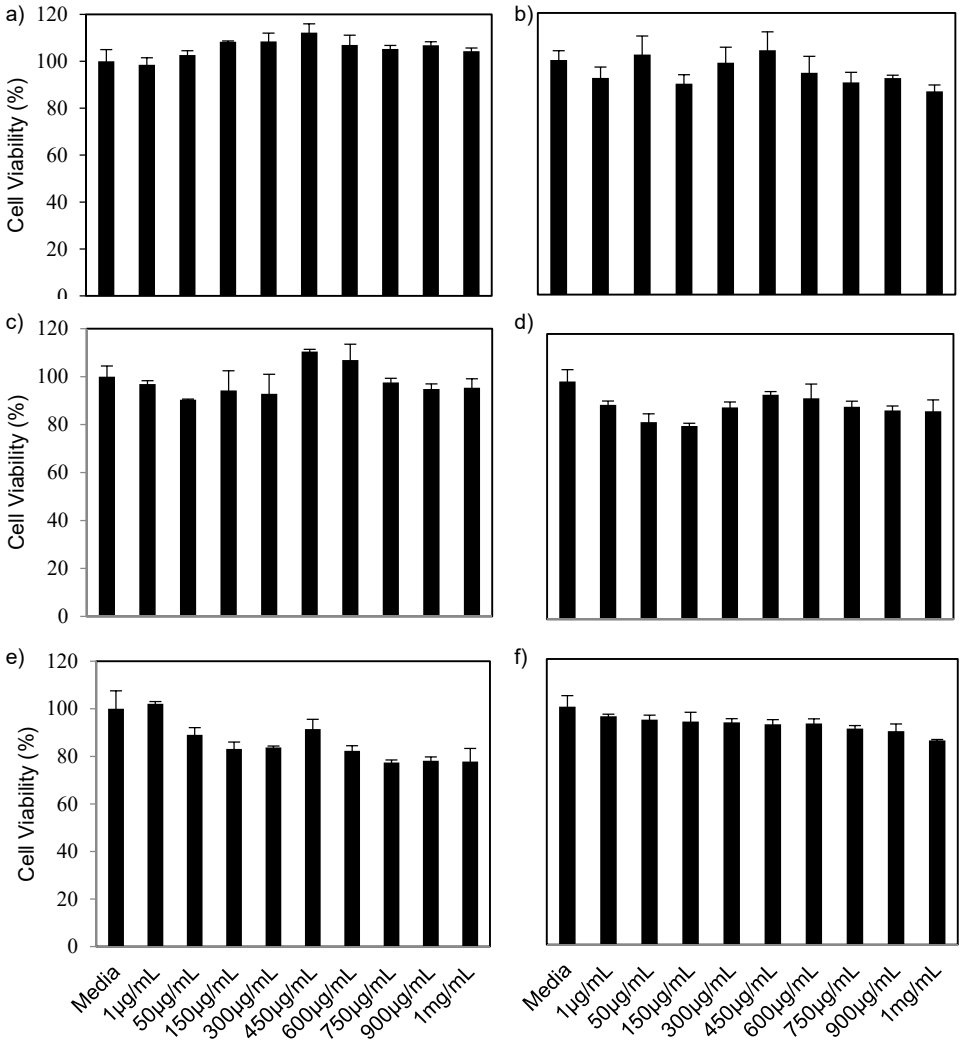

Figure 4.3. Cell viability assays of CNDs at various concentrations (1µg·mL^{-1} to 1 mg·mL^{-1}) with different cell lines at 72 h of incubation, 37 ºC and 5 % CO_2. (a) C33-A, (b) MCF-7, (c) MDA-MB-231, (d) A-549, (e) PC-3, (f) HeLa cancer cell lines. The values are expressed as mean ± standard deviation (SD) (number of experiments per data point n=4).

The internalization of CNDs by the adherent cells *in vitro*, was studied by laser scanning confocal microscopy (LSCM). According to the λ_{ex}-dependent PL behavior of CNDs, the dots emit in the green region under blue illumination. After 24 h of incubation, green emission from the cytoplasm, but not from the nuclei, was observed (**Figure 4.4**).[194] As reported in **Figure 4.4**, the cells were almost or completely viable under the experimental conditions, in agreement with the low concentration of CNDs used, which is unable to cause cell damage.[195,194]

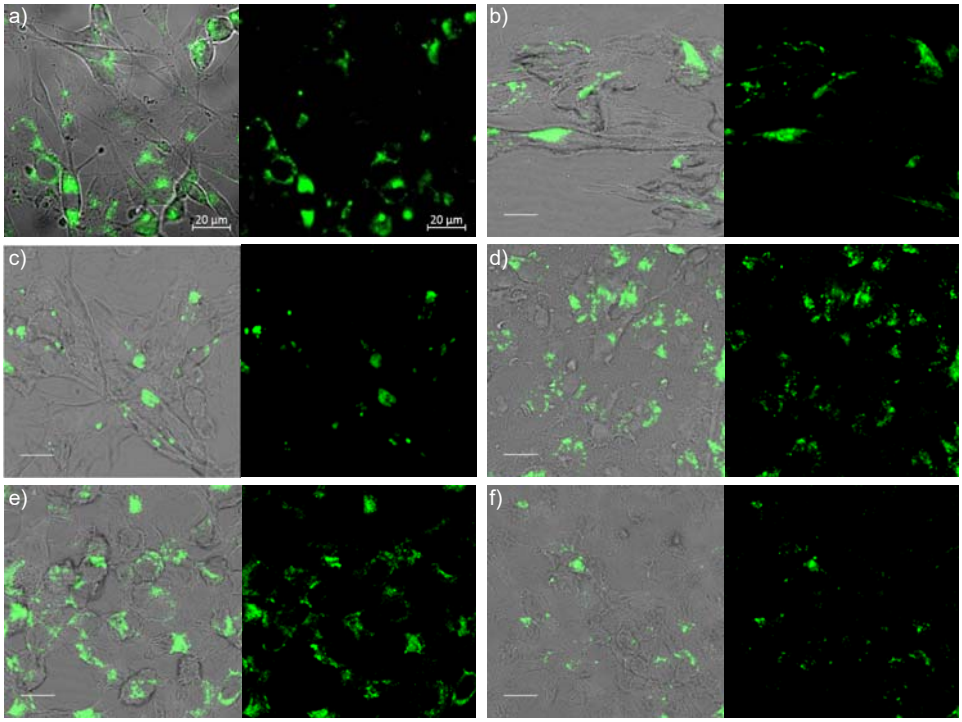

Figure 4.4. Confocal fluorescence images of (a) C33-A, (b) MCF-7, (c) MDA-MB-231, (d) A-549, (e) PC-3, (f) HeLa cancer cell lines after incubation with 300 µg·mL^{-1} CNDs. (left) Merged picture of the fluorescent bright field, and (right) fluorescent image.

The fluorescence intensities of CNDs in the cells grown in suspension were analyzed by flow cytometry measurements. **Figure 4.5** shows the flow cytometry histograms of the cellular uptake of Jurkat and HL60 cells treated with 300 µg·mL^{-1} of CNDs for 24 h or 72 h. Notably, the CNDs displayed an increased cellular uptake along the time and the higher uptake of the dots was observed after 72 h of incubation. The observed behavior can be ascribed to a different cellular uptake mechanism. In previously reported studies, it is demonstrated that the uptake of CNDs occurs through a caveolaeand clathrin-mediated endocytosis as well as passive diffusion.[196,197] Therefore, we suggest that CNDs may interact with the proteins of the cell membrane for the uptake and accumulate in suspended cells. Moreover, the presence of CNDs inside a cell does not induce cytotoxicity. Therefore, our results from flow cytometry are in good agreement with LSCM and cell viability studies, making CNDs a suitable material for drug delivery and imaging purposes.

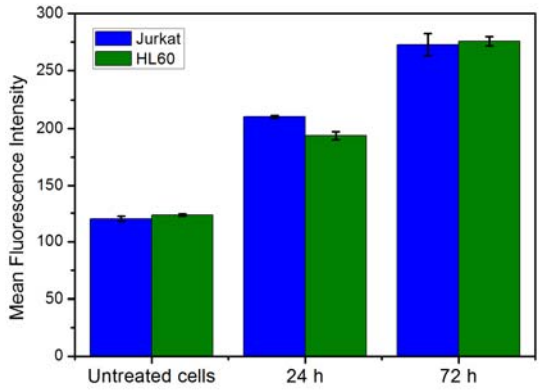

Figure 4.5. Flow cytometry results for Jurkat and HL60 cell lines. Cells incubated in the presence (24 h and 72 h) and in the absence of CNDs (untreated cells). The values are expressed as mean ± SD (n=4).

4.3.1.1. Influence of the protein corona on the CNDs cellular uptake

4.3.1.1.1. Cytotoxicity

Since small structural modifications can influence the cytotoxicity of a nanoparticle,[198] the cell viability should be determined for each specific system and under exactly the same conditions required for its employment. Therefore, MTT assays were performed not only on the naked CNDs but also after their modification with the artificial corona. The cell viability for both CNDs and HSA-Cy7@CNDs was determined under the same experimental conditions employed for the uptake studies by FACS, *i.e.* at a concentration of 300 μg·mL^{-1} and extended up to 72 h. **Figure 4.6** shows that the cell viability decreased after 72 h, but it was higher than 80 % under all the studied conditions.

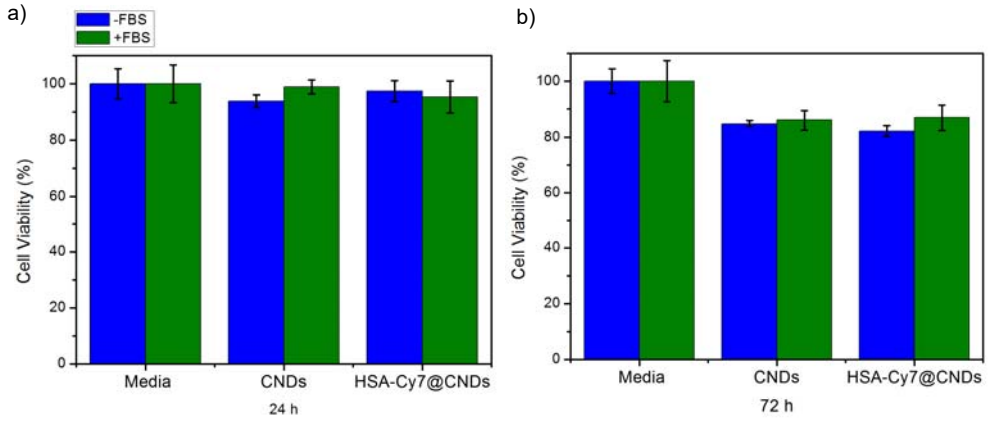

Figure 4.6. Cytotoxicity of CNDs and HSA-Cy7@CNDs (both at 300 μg·mL^{-1}) in PC-3 cells after incubation for 24 h and 72 h as determined by MTT assay.

Interestingly, results pointed out that the cell viability of the CNDs was slightly higher in the presence of serum proteins from the medium (*i.e.* with FBS), in agreement to previously reported studies on other carbon nanomaterials such as carbon nanotubes and graphene oxide.[181,182]

4.3.1.1.2. Quantitative analysis of uptake

The efficiency of the uptake of both CNDs and HSA-Cy7@CNDs by PC-3 cells was quantitatively analyzed using FACS. The mean fluorescence intensity (MFI) was higher when increasing the concentration of CNDs incubated with cells, indicating that the uptake was concentration-dependent following a linear trend. Interestingly, no saturation was observed in the studied range (100-400 $\mu g \cdot mL^{-1}$). In order to use an optimal concentration of CNDs for the following studies, a signal-to-background ratio ≥ 3 (*i.e.* the MFI of cells incubated with nanodots divided by the MFI of negative control cells) was the selected criteria, and this corresponds to a CNDs concentration of 300 $\mu g \cdot mL^{-1}$. The concentration-dependent uptake was also studied for the CNDs coated with the protein corona (HSA-Cy7@CNDs) and a similar trend was observed, but with decreased uptake values (**Figure 4.7**). It is important to note that all these assays were performed using serum-free media in order to avoid disturbance of the artificial protein corona formed onto the CNDs.

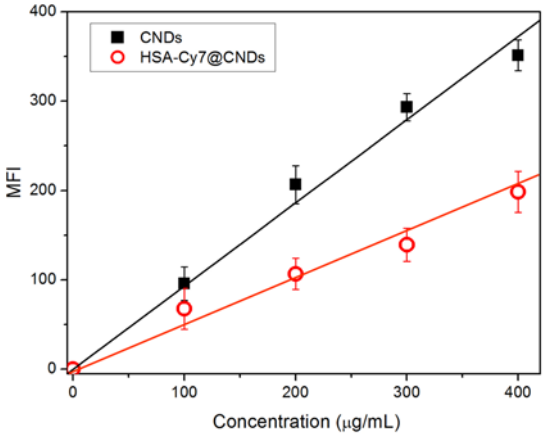

Figure 4.7. Concentration-dependent uptake in serum-free media of CNDs and HSA-Cy7@CNDs after 24 h by PC-3 cells as measured by FACS. The values are expressed as mean ± SD (n=3).

To further study the influence of the protein corona on the cellular uptake, cells were incubated for 24 h with CNDs (300 $\mu g \cdot mL^{-1}$) in both serum-free media (*i.e.* without FBS) and complete culture media (*i.e.* with FBS), and afterwards analyzed by FACS. The presence of FBS in the media, which contains large amount of proteins, leads to the formation of a natural corona around the nanoparticles. The results showed that the presence of FBS inhibits the cellular uptake of CNDs (**Figure 4.8**). In order to

confirm if such inhibitory effect is due to the formation of a protein corona onto the CNDs by the proteins present in the FBS, the uptake extent of the nanoparticles with a previously formed artificial protein corona (*i.e.* HSA-Cy7@CNDs) was also evaluated. It was found that the uptake of HSA-Cy7@CNDs was also lower as compared to the naked CNDs (*i.e.* CNDs in serum-free media), obtaining fluorescence intensity values almost identical in the case of a natural corona onto CNDs (FBS@CNDs) or an artificial one (HSA-Cy7@CNDs). Taking into account that the CNDs became negatively charged after the formation of the corona, *i.e.* zeta potential values of (+5.4 ± 1.4) mV and (-20.2 ± 2.1) mV for naked CNDs and HSA-Cy7@CNDs, respectively, a plausible explanation for the different uptake extent may be related to the electrostatic interactions of CNDs with the cells. Repulsive electrostatic interactions between the HSA-Cy7@CNDs and the negatively charged cell surface may lead to a diminished binding to the cell membrane compared to the naked CNDs, and consequently to a lower internalization. In any case, it seems clear that the degree of CNDs internalization depends strongly on the presence of a corona. Similar results confirming the uptake suppression effect of the protein corona were also reported for gold nanoparticles,[193] silica nanoparticles,[199] quantum dots.[200]

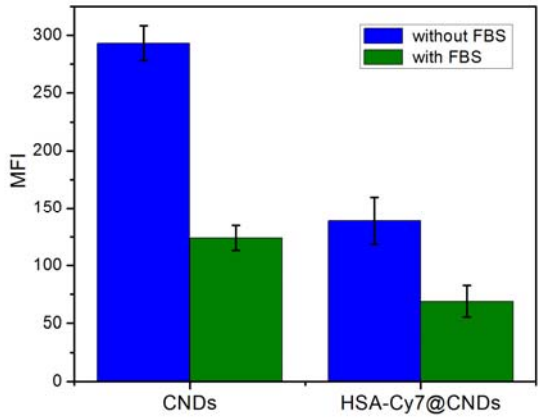

Figure 4.8. Uptake extent in both serum-free media and complete culture media by PC-3 cells, at a concentration of 300 μg·mL^{-1} of CNDs and HSA-Cy7@CNDs after 24 h, as measured by FACS. MFI corresponds to the fluorescence collected in the channel 1, *i.e.* the emission signal from the CNDs. The values are expressed as mean ± SD (n=3).

4.3.1.1.3. Uptake kinetics

To gain insights into the impact of the protein corona on the internalization of CNDs, uptake kinetics studies were carried out. To this end, CNDs and HSA-Cy7@CNDs (300 μg·mL^{-1}) were added with the cells and incubated in serum-free medium for different time periods (3–72 h), and then measuring the amount of internalized particles at each time point. As shown in **Figure 4.9**, the uptake of both naked CNDs and HSA-Cy7@CNDs was time-dependent and their kinetics followed similar trends. Increasing incubation times led to higher uptakes, which followed a linear

correlation, and without observing a plateau value (*i.e.* saturation), under the studied conditions. Despite similar trends, the slower internalization rate for the HSA-Cy7@CNDs is clear, around 3 times slower when compared to the naked CNDs (according to the difference in the slopes of the linear correlation). Looking at shorter incubation periods, an induction time was observed in both cases, without significant differences in the uptake observed up to 12 h of incubation. This finding indicates that a critical local density of CNDs on the cell membrane is required to initiate the active internalization process. In other words, a small NP such as CNDs may not be able to trigger endocytosis by itself because it interacts with an insufficient number of receptors, similar to previously reported small NPs (≤ 10 nm).[201]

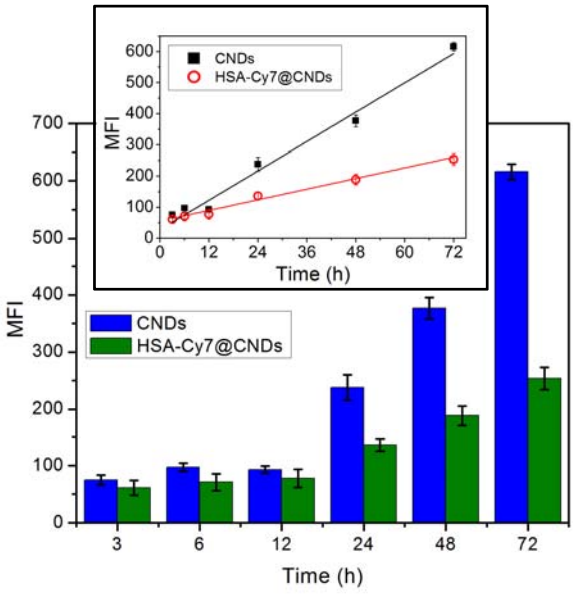

Figure 4.9. Uptake kinetic of CNDs and HSA-Cy7@CNDs (both at 300 μg·mL^{-1}) by PC-3 cells in serum-free medium for different incubation times up to 72 h as measured by FACS. The fluorescence intensity collected in the channel 1 (i.e. emission signal from the CNDs) The values are expressed as mean ± SD (n=3).

Comparing a natural formed protein corona with an artificial one is an important issue for evaluating if a protein corona model system can be used for predicting the NP's behavior in real scenarios. Therefore, kinetic uptake experiments were carried out with the CNDs coated with a natural corona formed by their interaction with FBS (FBS@CNDs) and CNDs coated with an artificial corona (HSA-Cy7@CNDs). While the former one was prepared under incubation in complete medium, the latter one was obtained under incubation in serum-free medium, in order not to cause any modification of the artificial layer of proteins. Interestingly, the obtained results were similar (**Figure 4.10**), which suggests that the artificial corona formed by HSA is able to mimic the behavior of the natural one (*i.e.* note that albumins are the major fraction of proteins present in the FBS). Based on this finding, the proposed protein corona

model on CNDs could be used for further studies, in order to better understand the role of CNDs in biological and biomedical applications.

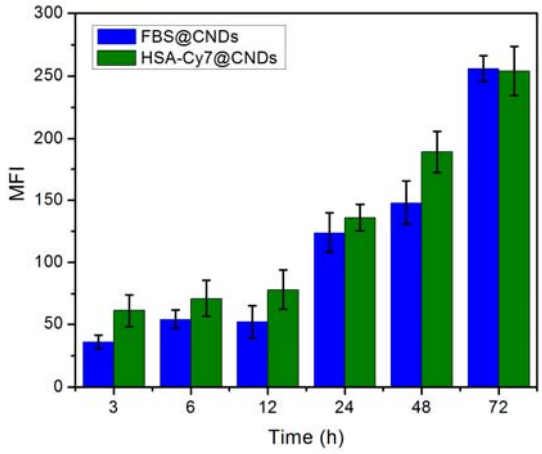

Figure 4.10. Comparison of the uptake kinetics of CNDs coated with a natural protein corona formed in the presence of FBS (FBS@CNDs) and with a corona formed artificially (HSA-Cy7@CNDs) as measured by FACS. MFI corresponds to the fluorescence collected in the channel 1, *i.e.* emission signal from the CNDs. The values are expressed as mean ± SD (n=3).

4.3.1.1.4. Reversibility of protein adsorption

To further study the reversibility of the protein binding onto the CNDs surface, the HSA-Cy7@CNDs were incubated with cells in complete medium (which contain natural proteins from the serum) and then its uptake kinetics were studied. Owing to the fact that the HSA protein was labeled with Cy7, it was possible to measure by FACS the signals coming both from the CNDs and from the HSA-Cy7. The kinetics uptake pattern was quite different for each fluorescence channel (**Figure 4.11b**), which clearly indicates that the protein-CNDs complex does not remain as a "unique entity" in time, or otherwise the evolution of the fluorescence signals from the different parts should be the same. Significant increase of the HSA signal from 6 to 12 h could be explained by desorption of some HSA-Cy7 from the CNDs (probably replaced by the proteins present in the medium) and the free HSA-Cy7 molecules being internalized faster than the HSA-Cy7@CNDs. However, the signal of HSA-Cy7 decreased along the time, while that of CNDs increased continuously, without reaching a plateau. We suggest that this observation could be due to two possible reasons: (*i*) after 48 h of incubation, a large fraction of HSA-Cy7 is replaced by natural non-labeled proteins, before internalization of the HSA-Cy7@CNDs and therefore, once the modified HSA-Cy7@CNDs is internalized, it will give a lower HSA-Cy7 signal because there is lower number of labeled-HSA per CND, and/or (*ii*) the HSA-Cy7@CNDs is partially desorb inside cells and the exocytosis of free HSA-Cy7 is faster than both the exocytosis of free CNDs and the uptake of new HSA-Cy7@CNDs. Nevertheless, these results showed that natural proteins of the serum

are replacing partially some of the HSA-Cy7 which formed the artificial protein corona (**Figure 4.11a**); therefore, the adsorption of HSA onto CNDs is reversible and the protein corona formation in this particular system can be described as a dynamic equilibrium.

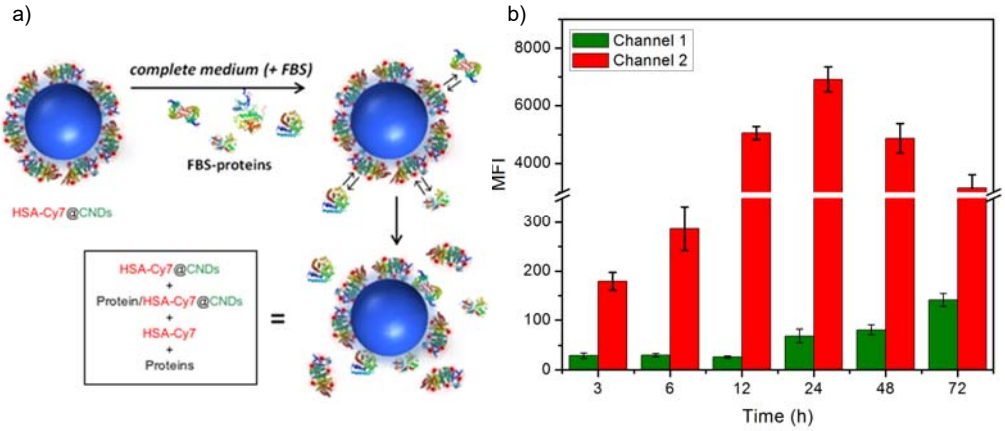

Figure 4.11. (a) Schematic representation of the dynamic equilibrium of the protein corona showing the replacement of initially adsorbed protein onto the CNDs when the particles are placed in culture medium containing serum proteins (FBS-proteins). (b) Uptake kinetics of HSA-Cy7@CNDs (300 μg·mL^{-1}) by PC-3 cells in complete medium as measured by FACS colleting the channel 1 (*i.e.* emission from CNDs) and channel 2 (*i.e.* emission from HSA-Cy7). The values are expressed as mean ± SD (n=3).

4.3.1.1.5. Imaging

By confocal fluorescence microscopy, qualitative data of the impact of the protein corona on the internalization of CNDs was obtained.

Figure 4.12 shows representative images of internalized naked CNDs, CNDs with a natural corona (FBS@CNDs), and CNDs with the artificial protein corona (HSA-Cy7@CNDs) under different incubation times (24 h and 72 h). The CNDs entered into cells without any further functionalization, and the uptake extent was higher at longer incubation times, which confirms the results obtained by FACS. Images also showed that the presence of a protein corona, either natural (FBS@CNDs) or artificial (HSA-Cy7@CNDs), led to a decreased internalization rate. However, no significant differences were observed in the intracellular localization in the presence of the protein corona. All together, confocal microscopy qualitatively supports the quantitative data obtained by FACS.

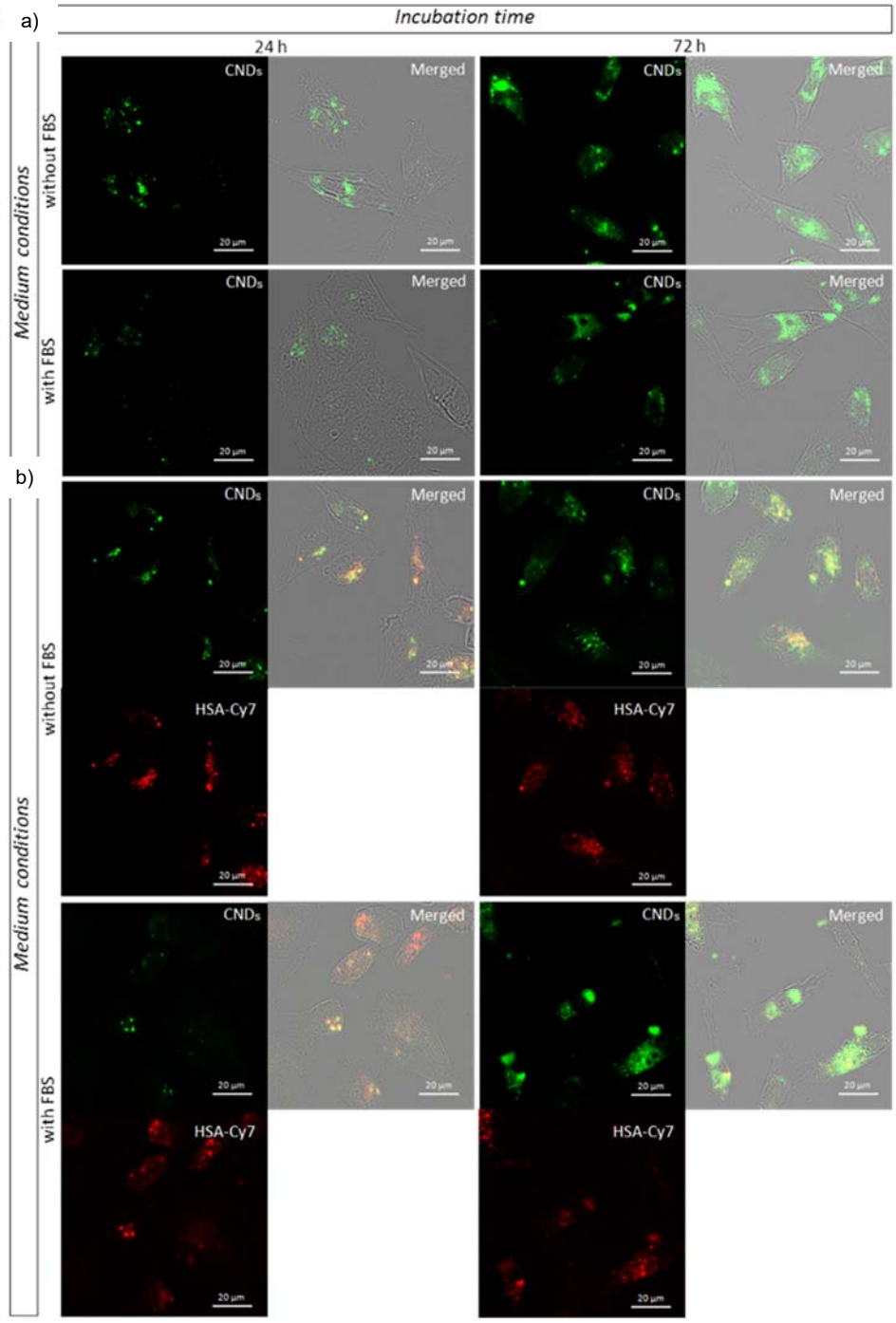

Figure 4.12. PC-3 cells incubated with 300 µg·mL^{-1} (a) CNDs or (b) HSA-Cy7@CNDs for 24 h or 72 h and in two different medium conditions (with and without FBS). The fluorescence of the CNDs is shown in green and that of the HSA-Cy7 in red.

4.3.2. CNDs as drug delivery systems

4.3.2.1. CNDs-PTX

Herein, we apply CNDs as vehicle towards the improvement of solubility and drug delivery of PTX. Thus, we created a multifunctional nanomaterial combining imaging and drug delivery. First of all, the half maximal inhibitory concentration (IC_{50}) was investigated for CNDs-PTX and PTX. Breast (MCF-7 and MDA-MB-231) and lung (A-549) were selected as target human cancer cell lines. The IC_{50} showed attractive results since our nanocarrier was more effective than the free drug (**Table 4.1**). These results encouraged us to expand its use in other different cell lines. Afterwards, CNDs-PTX system was tested in further human cancer cell lines: prostate (PC-3) and cervix (HeLa and C33-A). As collected in **Table 4.1**, only for PC-3 and C33-A cell lines, the results showed better efficiency when CNDs-PTX was used instead of PTX; however, no improvement was observed for HeLa cells. Therefore, it can be concluded that the CNDs can act as a vehicle to improve the efficacy of PTX in solid tumors.

Table 4.1. Concentration of PTX and CNDs-PTX required to kill 50 % of cells, IC_{50}.

Cell line	PTX $ng \cdot mL^{-1}$	CNDs-PTX $ng \cdot mL^{-1}$
MCF-7	81.4 ± 0.1	69.2 ± 0.2
MDA-MB-231	91.0 ± 0.1	65.1 ± 0.1
A-549	34.6 ± 0.1	30.4 ± 0.2
PC3	179.7 ± 0.1	140.8 ± 0.2
HeLa	2.9 ± 0.2	3.4 ± 0.3
C33-A	2820.0 ± 192.0	930.0 ± 179.7

In **Figure 4.13** is observed the Dose-Response diagrams of the cell viability. The fits were calculated based on the logarithm of concentration required to show changes in the cell viability and to calculated the IC_{50}. As it is showed in **Figure 4.13a**, the minimum concentration to observe changes in cervix cells was higher than the other cancer cell lines. Thus, these results suggest that CNDs-PTX showed low efficiency to fight against these kinds of cells. The behavior for others cancer cell lines was the opposite, showed a high efficiency compared with the free drug.

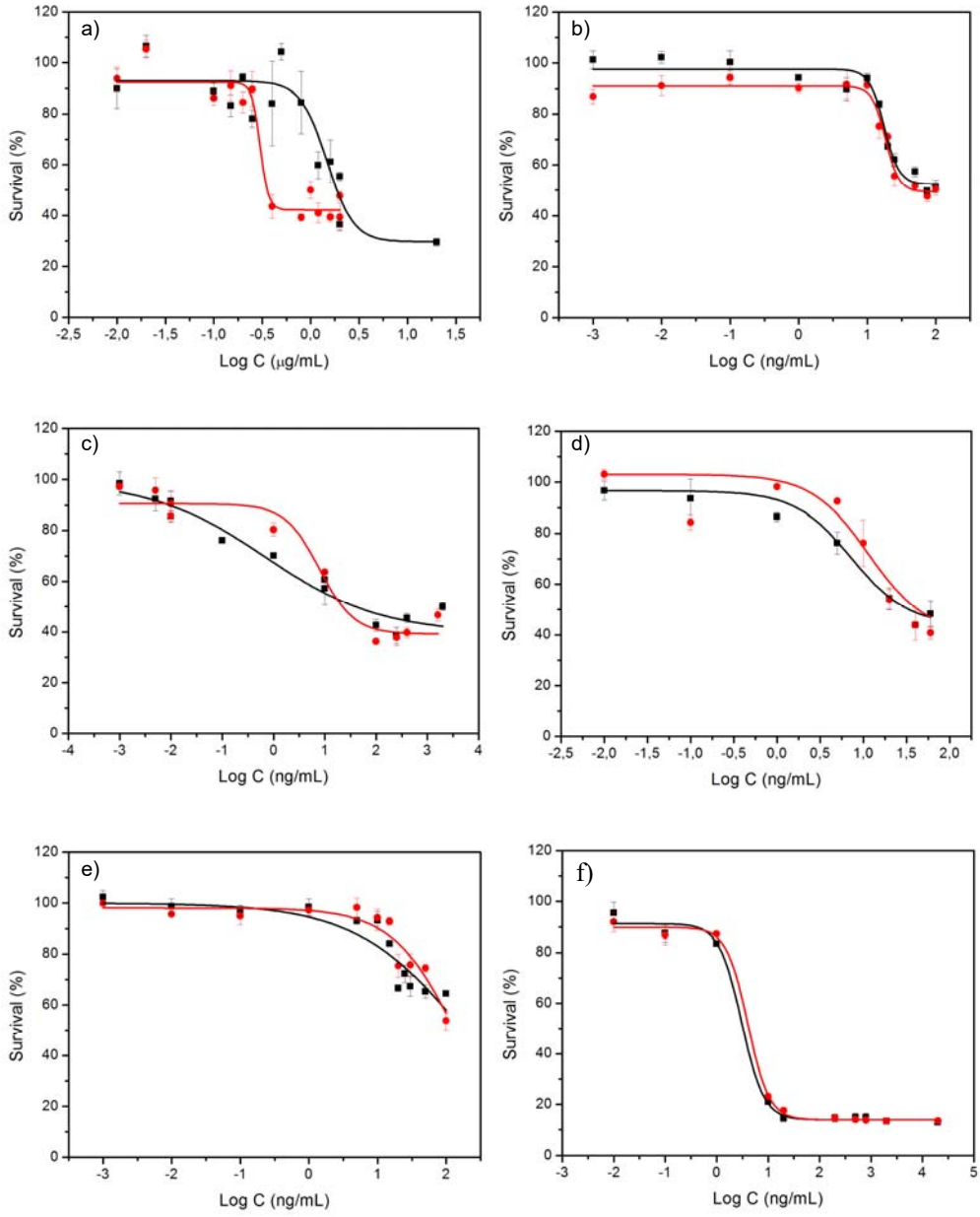

Figure 4.13. Dose-Response diagram of the cell viability of (a) C33-A (b) MCF-7 (c) MDA-MB-231 (d) A-549 (e) PC-3 (f) HeLa cells treated with PTX (black line) and CNDs-PTX (red line). The values are expressed as mean ± SD (n=4).

Moreover, statistical analyses were carried out for each cell line in order to explore if there is a particular concentration that is significantly different from the free drug. The results collected in **Figure 4.14** show the different concentrations of the species used for the cell viability assays for C33-A, MCF-7, MDA-MB-231 and PC-3 that

present a significant improvement of the CNDs-PTX against the free drug. For instance, at the concentration of 0.1 ng·mL^{-1} of PTX and CNDs-PTX in MCF-7 cancer cell line, the efficiency of the second was higher than the former, with a $P < 0.001$ *i.e.* P values of less than 0.05 were considered statistically significant (**Figure 4.14b**).

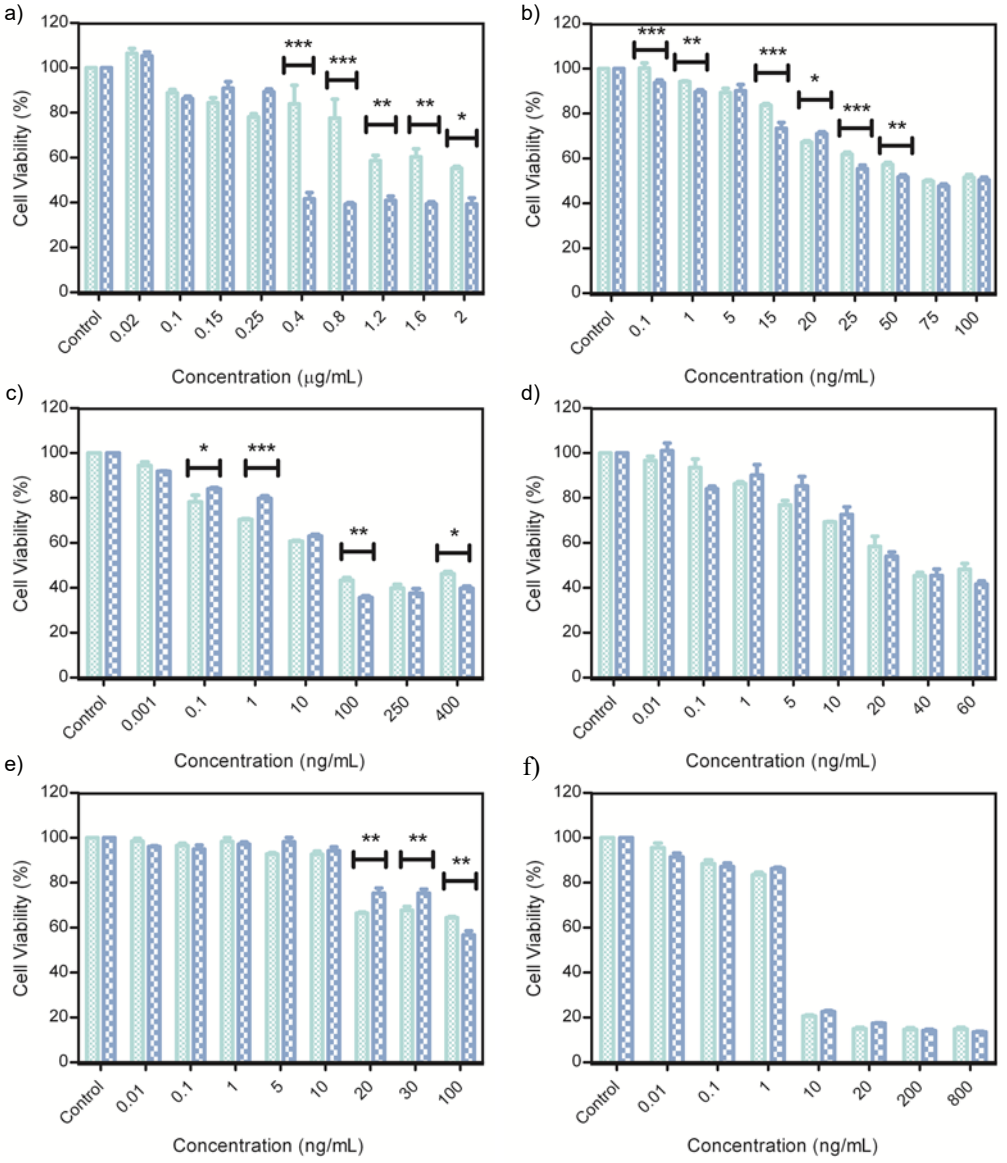

Figure 4.14. Cell viability of CNDs-PTX and PTX in several cancer cell lines at 72 h of incubation. (a) C33-A (b) MCF-7 (c) MDA-MB-231 (d) A-549 (e) PC-3 (f) HeLa cells treated with PTX (green bars) and CNDs-PTX (blue bars). The statistical analyses were performed using two-way ANOVA followed by Bonferroni's test. Data are expressed as mean ± SEM (n = 4). ***P < 0.001, **P < 0.01 and *P < 0.05.

Colorimetric assays are widely used to measure cell viability and cytotoxic effects; some of the most used tests are based on the following substrates: MTT, (3-(4,5-dimethyl-thiazol-2-yl)-5-(3-carbocymethoxyphenyl)-2-(4-sulfophenyl)-2H-tetrazolium (MTS), and 2,3-bis-(2-methoxy-4-nitro-5-sulfophenyl)-2H-tetrazolium-5-carboxanilide (XTT). However, these kinds of assays are single endpoint assays. The xCELLigence system can offer a real-time viable cell electronic sensing and supply the lack of information that provides the traditional experiments.[202] Therefore, xCELLigence was chosen as a platform for the biological study of the cell state. In this way, lung cancer cells were incubated in a complete media and cells responded through changes in their adherence to the conductive substrate, which was registered as a parameter named cell index (**Figure 4.15**). The curves showed a dose dependent cell response to CNDs-PTX. This result is in good accordance with the literature.[203,204] It can be noticed that following 20 h-incubation of A-549 cells with 100 ng·mL^{-1} CNDs-PTX, the cell index showed an initial decline, which corresponded to the morphological changes of the cells as a result of mitotic arrest and cell death. This cytotoxic profile induced by 100 ng·mL^{-1} CNDs-PTX is equivalent to the one registered for the free drug.[203] This information suggests a similar mechanism of action of PTX and CND-PTX, probably due to the PTX release from the surface of the CNDs *via* esterases.[205] Furthermore, Xu *et al.* reported that anti-mitotic compounds with similar mechanisms of action have often similar profiles in this technique.[203]

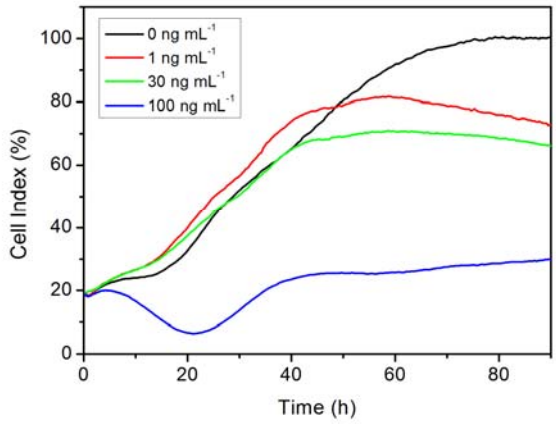

Figure 4.15. Real-Time survival curve of A-549 cancer cell line treated with different concentrations of CNDs-PTX.

PTX, as an anticancer drug, can cause cellular apoptosis by microtubule stabilization.[206] Thus, cellular apoptosis was evaluated with 4',6-diamidino-2-phenylindole (DAPI) as a nuclear counterstain that binds strongly to AT regions of DNA.[156] The nuclear stain was imaged at 405 nm excitation wavelength. As the DAPI and CNDs fluorescence emission spectra overlap, cyanine (Cy5) was used as label for easier discrimination of CNDs from DAPI. A-549 cells were incubated for 24 h with CND-PTX-Cy5 at a concentration of 20 ng·mL^{-1} related to PTX. Imaging of the

cells incubated with CNDs-Cy5 (**Figure 4.16a**) showed a homogeneous cell fluorescence without any presence of condensation, fragmentation of the nuclei nor apoptotic bodies, which are typical features of cellular apoptosis. In contrast, the nuclei of the cells treated with CNDs-PTX showed an apoptosis Stage III, displaying a grape shaped periphery and surrounding protrusions of chromatin, distributed in a few spherical apoptotic bodies (**Figure 4.16b**).[207] The apoptosis-inducing effect, despite the lack of a microtubule staining pattern by CND-PTX, can be explained by the cytosolic esterase effect mentioned above.[205] This result indicates PTX-CNDs keeps the same mechanism of action as PTX alone.

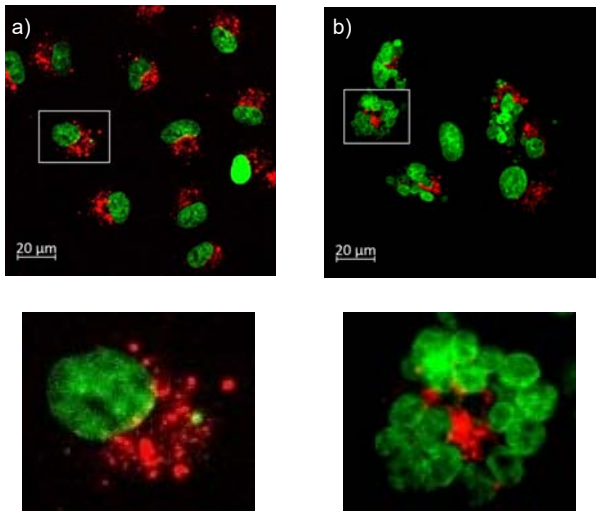

Figure 4.16. Apoptosis detection by confocal imaging of DAPI-nuclear stained (green), and CNDs-Cy5 (red). A-549 cells treated with CNDs-Cy5 (a) and CNDs-PTX-Cy5 (b).

The release of the covalently attached drugs from CNDs generally occurs by hydrolysis.[208] To test the intracellular release of PTX from the CNDs, the acute monocytic leukemia THP-1 cells that grow in suspension, and have a high uptake rate, were firstly incubated with CNDs-PTX for 24 h. Then, they were washed with media to remove the dots not attached to the cells and, finally, cell lysis was performed. Once the membrane-containing fraction was discharged, pristine CNDs were observed by fluorescence spectroscopy in the hydrosoluble fraction (**Figure 4.17**), showing a maximum excitation wavelength of 300 nm as described previously for CNDs (see Chapter 2, maximum emission intensity at 365 nm when excited at 300 nm). Such results indicated that the ester bond between PTX and CNDs was hydrolyzed to release drug, thus leaving CNDs appended with succinic acids (from the succinic anhydride previously attached onto the PTX). The FL spectrum presented for CNDs-succinic acid was approximately the same as pristine CNDs (max emission at 378 nm when excited at 300 nm), since succinic acid did not cause changes on the surface of the nanomaterial.

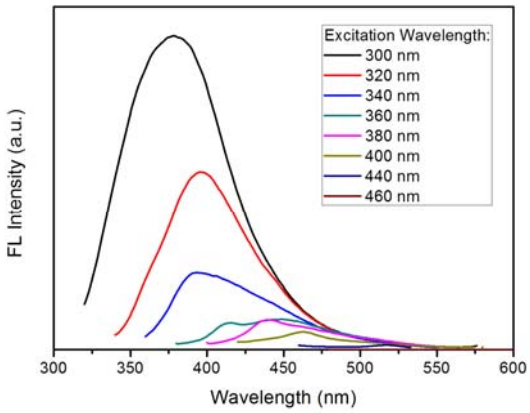

Figure 4.17. Fluorescence spectrum of the hydrosoluble fraction of THP-1 cells pre-incubated with CNDs-PTX that represents the CNDs-succinic acid.

4.3.2.2. CNDs-CBL

After successfully employing CNDs-PTX as a drug delivery nanocarrier, we sought to extend our methodology to another drug, such as CBL. First of all, to applied this system to the use of drug delivery their pharmaceutical activity was evaluated with four cancer cell lines (MDA-MB-231, HeLA, HL60, Jurkat) and one non-cancerous (HDFa), which were treated with different dose of CNDs-CBL and CBL for 72 h. As expected, after 72 h of incubation all kinds of cells treated with free CBL were found to inhibit the cell growth at any concentrations. Moreover, the cell death is increasing with the concentration of the species, as observed in **Figure 4.18**. Interestingly, the results showed a better efficiency when CNDs-CBL was used rather than CBL alone in MDA-MB-231, HeLa and HL60 cell lines; for the Jurkat cell line, the efficiency of both CNDs-CBL and CBL was almost equivalent. In particular, for HL60 cells incubated with CBL and CNDs-CBL at a concentration of 10 $\mu g \cdot mL^{-1}$, 40 % and almost 60 % of the cancer cells, respectively. Thus, our nanocarrier displayed a better efficiency. As previously demonstrated, since CNDs do not affect the cell survival, the toxicity is induced by the loaded CBL drug, which retains its pharmacodynamic activity.

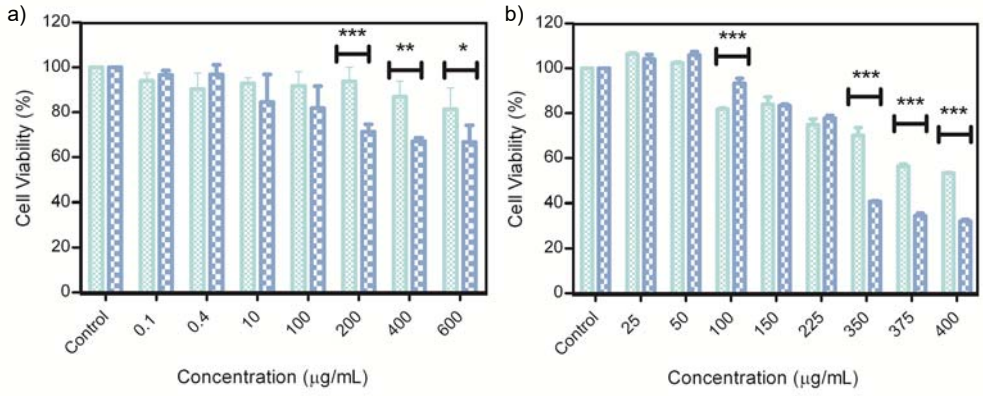

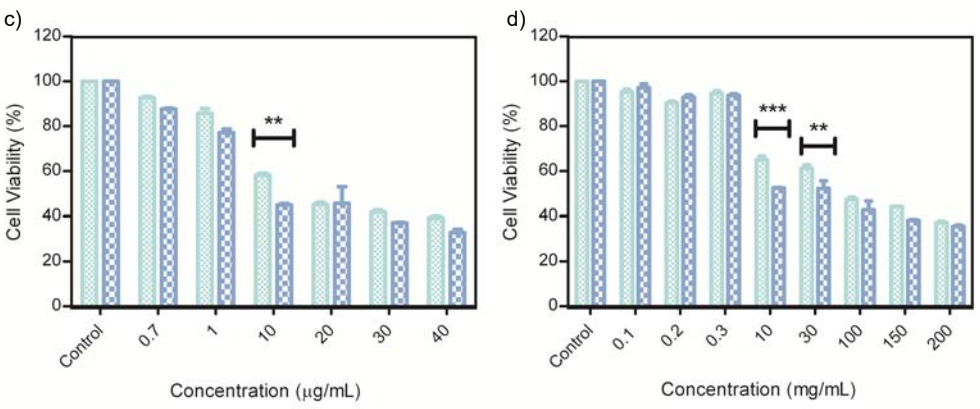

Figure 4.18. *In vitro* antitumor efficacy of CNDs-CBL and CBL in several cancer cell lines at 72 h of incubation. (a) MDA-MB-231, (b) HeLa, (c) HL60 and (d) Jurkat cell lines treated with CBL (green bars) and CNDs-CBL (blue bars). The statistical analyses were performed using two-way ANOVA followed by Bonferroni's test. Data are expressed as mean ± SEM (n=4). ***P < 0.001, **P < 0.01 and *P < 0.05.

We also examined the effect of free CBL and CNDs-CBL on human dermal fibroblasts (HDFa, *i.e.* healthy cells). **Figure 4.19** shows the *in vitro* cell viability using similar doses, after 72 h. It is noteworthy that CBL and CNDs-CBL displayed a similar profile up to 150 $\mu g \cdot mL^{-1}$, then CNDs-CBL induced death at a lower rate than free CBL, indicating that CNDs-CBL exhibit more prohibitive effect on cancer cells compared to the non-cancerous ones. Therefore, it can be concluded that the CNDs improved the effectiveness in cancer cell lines, when compared to CBL alone.

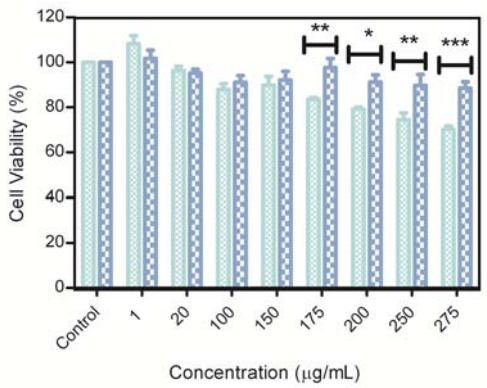

Figure 4.19. *In vitro* antitumor efficacy of CNDs-CBL (blue bars) and CBL (green bars) in human dermal fibroblasts, HDFa cell line after 72 h of incubation. The statistical analyses were performed using two-way ANOVA followed by Bonferroni's test. Data are expressed as mean ± SEM (n = 4). ***P < 0.001, **P < 0.01 and *P < 0.05.

4.3.3. Permeation of CNDs and PEGylated-CNDs through *in vitro* Blood-Brain Barrier

The blood-brain barrier (BBB) plays a critical role in normal physiology of the central nervous system by regulating what reaches the brain from the periphery. Nowadays, it is of great interest the study of the permeability and delivery through the BBB of therapeutic agents, for the treatment of the most brain disorders. However, being unable to perform real-time studies of BBB function in 3D models has been the liming factor. Thus, the xCELLigence system can offer a real-time cell electronic sensing and supply the lack of information that provides the traditional experiments.[202] Herein, we evaluated the permeability of CNDs and carbon nanodots modified with PEGylated chains (CNDs-DEGd and CNDs-PEG_{400}) trough an *in vitro* 3D inverted BBB model using real time xCELLigence system to study the cell state (**Figure 4.20**).

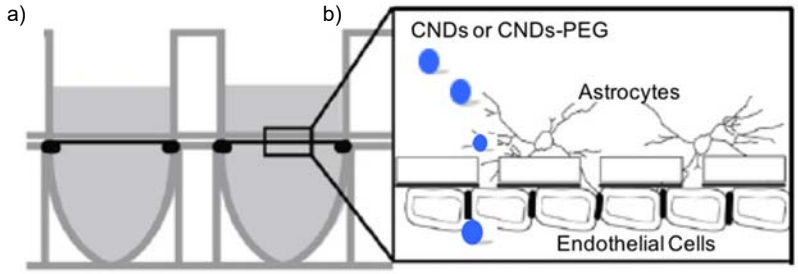

Figure 4.20. (a) Representation of the xCELLigence cell migration plate, (b) the 3D inverted BBB model. Adapted from MacLean *et al*. 2014.[209]

We have cultured an inverted BBB model with human umbilical vein endothelial cells (HUVEC) on electrodes, which are on the lower surface of xCELLingence cell invasion migration plates, as it is showed in **Figure 4.20**.[209] Then, the cell invasion migration plates were incubated at 37 ºC and 5 % of CO_2. The cell response, named cell index, followed the changes in HUVEC cells and was registered due to the conductive substrate.[203] The cell index showed an initial increase, which corresponded to the morphological changes of the cells. When HUVEC cells reached a plateau, around 70 h, astrocytes were seeded into the basal wells (**Figure 4.21**). Afterwards, the BBB model was followed using the xCELLigence software to monitor the effects of astrocyte processes on electrical resistance of the HUVEC cells. Following this, the cell invasion migration plates were incubated at 37 ºC and 5 % of CO_2.

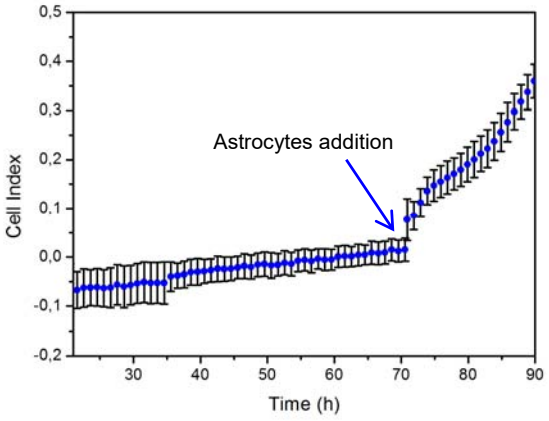

Figure 4.21. Real-Time monitoring of endothelial cells.

We incubated propidium iodide as positive control (crosses the membrane) and FITC-Dextran 10KDa as negative control (does not cross the membrane) in order to confirm the permeability of the 3D BBB model. To assess the barrier permeability, we measured the rate of diffusion across the membrane (**Equation 4.1**), commonly known as permeability coefficient (P_{app}):[210]

Equation 4.1

$$P_{app} = \frac{V}{A \times [C]_{apical}} \times \frac{\Delta[C]_{basolateral}}{\Delta t}$$

To assess the permeability of CNDs and their derivatives, we incubated 500 μg·mL^{-1} of each sample onto the basal side of the BBB model. We carried out the measurements at the end of each assay; we collected the medium from both the lower surface and basal sides of the cell invasion migration plates of the BBB model, after 24 h. Then, we measured the concentration of the controls and the CNDs in the medium of both sides by determining the absorbance intensity, based on the analytical curves of each sample measured with a microplate reader. We evaluated the permeability of CNDs and derivatives through an inverted BBB using a real-time cell response. Therefore, we can confirm that our nanomaterials were able to cross the BBB model (**Figure 4.22**), as the P_{app} of the CNDs was higher that the positive control.

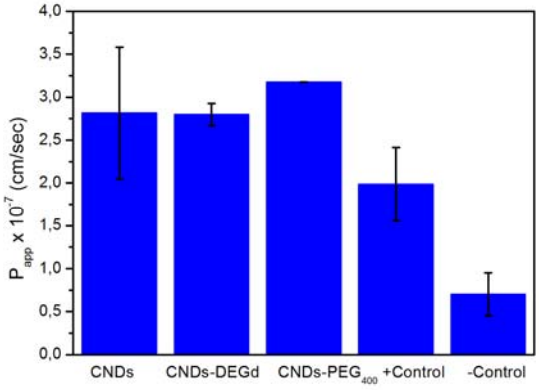

Figure 4.22. Permeability of CNDs, CNDs-DEGd, CNDs-PEG_{400}, propidium iodide (+Control) and FITC-Dextran 10KDa (-Control) through a 3D inverted BBB model. The values are expressed as mean ± SD (n=4).

4.4. Conclusions

In the first part of this chapter, the viability of CNDs in biological and biomedical applications was assessed by preparing new hybrid materials with protein corona. Particular attention has been placed in the quantitative analysis of the uptake, the kinetics and the reversibility of the protein adsorption. We observed a significant decrease in the extent of internalization and a slow-down in the uptake kinetics of the CNDs by the cells. In addition, we have designed a model of labeled artificial corona, which was shown to mimic the behavior of the natural corona formed spontaneously in the presence of serum proteins.

Furthermore, the most impressive results obtained in this chapter were the high efficiencies shown by our nanocarriers CNDs-PTX and CNDs-CBL, in terms of the pharmacological activity in tumor models. Moreover, the ability of the CNDs-CBL to discern between cancer cell lines and non-cancerous cells was also observed. Thereby, such findings indicate that the nanocarrier approach is as a very promising candidate for highly efficacious drug delivery, commonly used in cancer therapy.

Finally, we evaluated the *in vitro* permeability of CNDs and their derivatives through an inverted BBB using a real-time cell response. The resulting nanomaterials were able to cross the BBB model.

CHAPTER 5

General Conclusions and Future Perspectives

CHAPTER 5

General Conclusions and Future Perspectives

"You can only analyze the data you have. Be strategic about what to gather and how to store it" Marie Skłodowska Curie

Herein, the general conclusions of the research studies presented on this dissertation are summarized.

In the first Chapter of this thesis an introduction about C-Dots was described. A critical classification of the different types of C-Dots was reported. Moreover, the production methods, properties and applications (especially bioapplications) were also discussed.

The synthesis, purification and characterization of nitrogen-doped CNDs were presented in Chapter 2. It was employed a simple, controllable and fast microwave-assisted hydrothermal synthesis for CNDs that holds promise for bioapplications. The obtained material was characterized by employing UV-Vis, FL, FT-IR, AFM, TEM, DLS and XPS techniques. CNDs showed tunable fluorescence emission, with sizes around 3 nm, excellent solubility in water and several functional groups onto their surface.

In Chapter 3, the functionalization of CNDs with different molecules by using several approaches was described. In the first part of this chapter, the surface modification of CNDs was performed with a DEG derivative and maleimide groups. Moreover, different methods of purification were assessed. Furthermore, CNDs were functionalized with FeNPs, drugs and proteins. The as-prepared nanomaterials were characterized by employing UV-Vis, FL, FT-IR, AFM, TEM, DLS and XPS

techniques. The loading of the drugs was calculated through TGA and MALDI techniques, while for the quantification of the protein HSA adsorbed onto the surface of the CNDs it was used the Bradford assay.

In the final chapter, the as-prepared nanosystems were investigated as drug delivery systems and nanocarriers. Firstly, the cell viability of CNDs in several cancer cell lines was assessed by MTT assay. The CNDs resulted to be no toxic up to high concentrations. Then the hybrids discussed in chapter 3 were studied. Particular attention has been placed in the quantitative analysis of the uptake, the kinetics and the reversibility of the protein adsorption in the CNDs-HSA system. A significant decrease in the extent of internalization and a slow-down in the uptake kinetics of the CNDs by the cells were observed. In addition, we have designed a model of labeled artificial corona, which was shown to mimic the behavior of the natural corona that is formed spontaneously in the presence of serum proteins. In the third part of the chapter, promising results in terms of the pharmacological activity in tumor models were observed for the nanocarriers CNDs-PTX and CNDs-CBL. Moreover, the ability of the CNDs-CBL to discern between cancer cell lines and non-cancerous cells was also observed. Our results indicate that the use of CNDs as nanocarrier result in promising drug delivery systems. Finally, it was evaluated the *in vitro* permeability of CNDs and their derivatives through an inverted BBB using a real-time cell response. The resulting nanomaterials were able to cross the BBB model.

As a future perspective, an optimization of the FeNPs functionalized with a rigid linker onto the surface of the CNDs will be studied. In addition, in order to validate the final nanosystem, further experiments will be addressed, such as studying the magnetic properties.

Subsequently, as a promising goal, the use of CNDs-Maleimide for the construction of the target biomolecule will be addressed. In order to achieve this future goal, the covalent functionalization of CNDs-Maleimide with –SH peptides will be exploited, searching a maximum coverage while maintaining a good colloidal stability of the resulting complex. In addition, the final nanosystem will be characterized.

Finally, CNDs derivatives with PEGylated chains have showed potential to cross the BBB; therefore, a drug to target the brain will be attached onto the nanosystem. At this point, a comparison of the different derivatives CNDs-PEGylated to cross the BBB will be carried out.

In summary, in this doctoral thesis, interesting and novel hybrid materials based on CNDs were designed, prepared and studied as drug delivery systems, bioimaging agents and drug nanocarriers.

Appendix

Experimental Section

Appendix

Experimental Section

I. Experimental details

II. Reagents and materials

L-Arginine (Arg), ethylenediamine (EDA), [2-(2-Methoxyethoxy)ethoxy]acetyl acid, N-(3-Dimethylaminopropyl)-N′-ethylcarbodiimide hydrochloride (EDC), N-Hydroxysuccinimide, $FeCl_2$, $FeCl_3$, paclitaxel, succinic anhydride, N,N-dimethylformamide, human serum albumin, pyridine, Kaiser test kit and sephadex LH-20 were purchased from Sigma-Aldrich without further purifications. Cyanine5 NHS ester and sulfo-Cyanine7 NHS ester (Cy7) were purchased from Lumiprobe. All the reagents were used as supplied without further purifications. Dialysis membrane tubes with a cutoff 0.5-1 kDa and 1-3 kDa were supplied by Spectrum Labs. PD-10 desalting column packed with sephadex G-25 resin were obtained from GE Healthcare while amicon ultra-15 centrifugal filter units with a cut-off 30 kDa were supplied by Millipore. Bradford reagent was obtained from AppliChem (Germany). The solvents used were purchased from Carlo Ebra.

For cell culture, 75 cc T-flask (T75) and 48 well-plates were obtained from Nunc. Dulbecco's modified Eagle's medium (DMEM), fetal bovine serum (FBS), and L-glutamine were purchased from Gibco. Penicillin and streptomycin were purchased from Hyclone. Hanks′ Balanced Salt solution and Trypan Blue solution were supplied by Sigma-Aldrich. Cell Proliferation kit I based on 3(4,5-Dimethylthiazol-2-yl)-2,5-diphenyltetrazolium bromide (MTT assay) was purchased from Roche. 8-well glass Millicell EZ slide was supplied by Millipore and mounting media by Dako. Ultrapure water (18.2 MΩ cm @25 °C) used in all the experiments was produced using a Milli-Q water system.

III. Apparatus

UV-Vis absorption spectra were recorded on a V-630 Bio spectrophotometer Jasco Analytical Instruments. Fluorescence spectra were measured on a LS55 Perkin Elmer fluorimeter. All the spectra were recorded at room temperature using 10 mm path-length cuvettes. Fourier-transform infrared (FT-IR) spectroscopy was performed on a Nicolet 5700 spectrometer from Thermo Electron for KBr pellets. Thermogravimetric analysis (TGA) were run on a TA Instruments Discovery system under N_2 purge with a heating rate of 10 °C·min^{-1}. XPS experiments were performed in a SPECS Sage HR 100 spectrometer with a non-monochromatic X-ray source of Magnesium with a Kα line of 1253.6 eV energy and 250 W. The samples were placed perpendicular to the analyzer axis and calibrated using the 3d5/2 line of Ag with a full width at half maximum (FWHM) of 1.1 eV. An electron flood gun was used to compensate for charging during XPS data acquisition. The selected resolution was 30 and 15 eV of Pass Energy and 0.5 and 0.15 eV/step for the survey and high-resolution spectra, respectively. Measurements were made in an ultra-high vacuum (UHV) chamber at a pressure below $8 \cdot 10^{8}$ mbar. Fitting of the XPS data were done using Casa XPS 2.3.16 PR 1.6 software. For our data, the Shirley-type background subtraction was used and all curves were defined as 30% Lorentzian, 70% Gaussian. Atomic ratios were computed from experimental intensity ratios and normalized by atomic sensitivity factors. A Malvern Zetasizer, equipped with a 10 mW He–Ne laser operating at a wavelength of 633 nm, was used to measure the hydrodynamic diameter d_h (with dynamic light scattering, DLS) and the zeta-potential (with laser Doppler anemometry, LDA) of the samples. Atomic force microscopy (AFM) images were obtained with a Nanoscope IIIa, VEECO Instruments. As a general procedure to perform AFM analyses, tapping mode with a HQ:NSC19/ALBS probe (80 kHz; 0.6 N/m) (MikroMasch). The obtained AFM-images were analyzed in Gwyddion 2.41. Transmission electron microscopy (TEM) images were acquired in JEOL JEM 2100F microscope. Sample was prepared on glow discharged carbon film 400 copper mesh grids from Electron Microscopy Sciences (Hatfield, USA) and uranyl acetate purchased from Electron Microscopy Science was used for the negative staining of the sample. Image J software was used for the analysis of the images. NMR spectra were obtained on a Varian Inova spectrometer (500 MHz ^{1}H and 125 MHz ^{13}C) or on a JEOL Eclipse 400FT (400 MHz ^{1}H). Chemical shifts are reported in ppm using the solvent residual signal as an internal reference ($CDCl_3$: δ_H = 7.26 ppm). The resonance multiplicity is described as *s* (singlet), *d* (doublet), *t* (triplet), *q* (quartet), *m* (multiplet). MALDI-Tof mass analyses were performed on an Ultraflextreme III time-of-flight mass spectrometer equipped with a pulsed Nd:YAG laser (355 nm) and controlled by FlexControl 3.3 and FlexImaging 2.1 softwares (Bruker Daltonics, Bremen, Germany). Absorbance of MTT product was detected in a micro plate reader GENios Pro, TECAN. The normalized cell index at real time was measured on a xCelligence Real-Time Cell Analysis (RTCA). Fluorescence images were taken in a confocal microscope (lsm 500 meta, Zeiss) with laser 488 nm, 505 LP filter and 20X magnification objective with differential interference contrast for transmitted light. Flow Cytometry measurements were carried out using a 3-laser BD FACS Canto™ II system and data analysis was performed with FACSDiva software.

IV. Synthesis and methods

i. Synthesis

CNDs (**3**)[31]

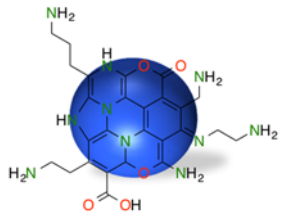

3

Briefly, 87 mg of L-Arginine and 33 µL of ethylenendiamine (1:1 mol) were dissolved in 100 µL of water and placed into a microwave reactor. The mixture was heated at 240 °C and 200 W for 180 s. During the microwave heating, the solution changed color from transparent to brown as a result of the formation of CNDs. The solution was then diluted with water and filtered through a 0.1 µm microporous membrane separating a deep yellow solution that was dialyzed against pure water for 2 days by using a dialysis membrane (cut-off 0.5-1 KDa). The aqueous solution of CNDs was lyophilized giving 27.0 mg of a yellowish solid which was stored in dry form at darkness until use.

CNDs-DEGd (**5**)

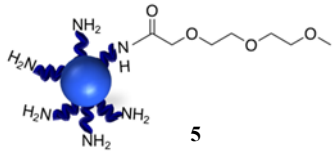

5

To a solution of 2.0 mg (0.01 mmol) of [2-(2-Methoxyethoxy)ethoxy]acetyl acid in 5.0 mL of DMF, 3.2 mg (0.01 mmol) of EDC, and 2.0 mg (0.01 mmol) of NHS were added. The mixture was stirred at 0 ºC for 1 h. CNDs 5.0 mg were added and the resulting mixture was stirred at r.t. overnight. The solvent was removed under reduce pressure re-suspended in milli-Q water and filtered through a 0.1 µm microporous membrane. The solution was dialyzed against milliQ water for 24 h. The aqueous solution of CNDs-DEGd was lyophilized giving a yellowish solid which was stored in dry form at darkness until use. This gave 7.8 mg of CNDs-DEGd yellowish powder.

[2-(2-Methoxyethoxy)ethoxy]acetyl chloride (**6**)[155]

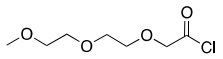

6

The acid [2-(2-Methoxyethoxy) ethoxy]acetyl acid 1.0 g (5.6 mmol) was slowly dropped in a round bottomed flask containing thionyl chloride 1.2 mL (17.0 mmol) in dichloromethane (2.5 ml). The resulting clear solution was stirred at room temperature for 15 min, then refluxed for 1 h. Thionyl chloride and volatiles were removed by vacuum obtaining the acid chloride in quantitative yield as a liquid (639 mg, 58 %). **^{1}H-NMR** (400 MHz, $CDCl_3$) δ: 5.14 (m, 1H), 3.60 (s, 4H), 3.55-3.49 (m, 4H), 3.30 (m, 2H), 2.86 (t, *J* = 5.2 Hz, 2H), 1.43 (s, 9H), 1.29 (m, 2H) ppm.

CNDs-PEG_{400} (**5'**)

5'

To a solution of 40.0 mg (0.04 mmol) of CNDs in 5.0 mL of ethanol, 32.0 mg of tosyl chloride precursor of PEG_{400} was added. The mixture was stirred at reflux overnight. The solvent was removed under reduce pressure re-suspended in milli-Q water and filtered through a 0.1 µm microporous membrane. The solution was evaporated again and the crude was chromatographed by size exclusion chromatography 100% MeOH. The obtaining aqueous fractions of CNDs-PEG_{400} were lyophilized giving a yellowish oil which was stored at darkness until use. This gave 62.5 mg of CNDs-PEG_{400}.

CNDs-Maleimide (**8**)

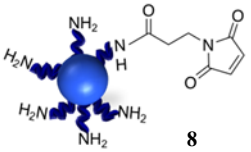

8

To a solution of 3.0 mg (0.01 mmol) of N-succinimidyl 3-maleimidopropionate in 5.0 mL of DMF, 6 µl mg *i*$PrEt_3N$ and 5.0 mg (0.01 mmol) of CNDs were added. The mixture was stirred at r.t. at r.t. overnight. The solvent was removed under reduce pressure re-suspended in milli-Q water and filtered through a 0.1 µm microporous membrane. The solution was dialyzed against milli-Q water for 24 h. The aqueous solution of CNDs-Maleimide was lyophilized giving a yellowish solid which was

stored in dry form at darkness until use. This gave 6.3 mg of CNDs-Maleimide yellowish powder.

CNDs-Cy5 (**10**)

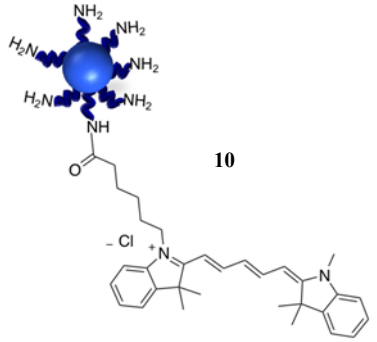

10

A solution of 40.0 mg of CNDs and 2.5 mg of cyanime5 NHS in 5.0 mL of DMF was stirred at r.t. overnight. The solvent was removed under reduce pressure. The crude was diluted with water and was filtered through a 0.1 μm microporous membrane separating a blue solution that was dialyzed against pure water through a dialysis membrane for 1 day. The aqueous solution of CNDs-Cy5 was lyophilized giving 38.0 mg of a blue solid.

Fe_3O_4 nanoparticles FeNPs (**13**)[160]

13

The iron nanoparticles were synthesized under a nitrogen atmosphere, it was used a 1:2 mol ratio of Fe^{2+} and Fe^{3+} respectively. Each iron salt was weighed out and subsequently dissolved in 50 mL DI water. Both iron salt solutions were combined in a 3-necked flask and heated to 70 ºC under vigorous mechanical stirring. Ammonium hydroxide was added drop-wise until a uniform black solution (at a pH of 10 – 11) had precipitated and was then left for 1 h at 70 ºC. After that, the Fe_3O_4 nanoparticles were magnetically separated and then washed three times with DI water and another three times with dichloromethane. The washed Fe_3O_4 nanoparticles were kept it in solution until used.

FeNPs-TEPSA (**15**)[161]

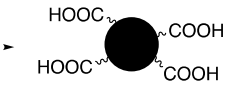

15

The as-obtained suspension of FeNPs 20 ml was diluted with dimethylformamide (50 ml) and water was eliminated under reduced pressure. TEPSA 7.1 ml (25 mmol) was then slowly added to the nanoparticle dispersion in DMF; 4.3 ml of water was then added, followed by an aqueous solution of TMAOH 2.5 ml (1 M; 2.5 mmol) at room temperature and under stirring. The solution was heated to 100 ºC for 24 h under continuous stirring. The magnetic nanoparticles were collected and dissolved with acetone diethylether mixture and then magnetic decantation was carried out. After washing with acetone, the black precipitate was dispersed in water and magnetically separated again. The amount of carboxylic groups was estimated as a molar ratio of 0,65 mmol·g^{-1} acidic functions compared to the total iron content.

CNDs-FeNPs (**16**)

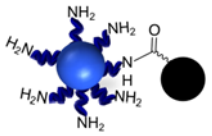

16

To a solution of 4.4 mg (0.003 mmol) of FeNPs-TEPSA in 5.0 mL of DMF, 1.0 mg (0.005 mmol) of EDC, 0.6 mg (0.005 mmol) of NHS and 2 µl Et_3N were added. The mixture was stirred at 0 ºC for 1 h. CNDs 2.0 mg were added and the resulting mixture was stirred at r.t. overnight. The magnetic decantation was performed and washes with DI water, methanol and diethyl ether were performed. This gave 5.0 mg of CNDs-FeNPs-TEPSA as a brown solid.

tert-butyl (2-(2-(2-aminoethoxy)ethoxy)ethyl)carbamate (**19**)[164]

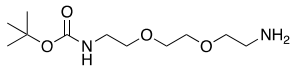

19

Synthesis of tert-butyl (2-(2-(2-aminoethoxy)ethoxy)ethyl)carbamate.[164] A solution of di-*tert*-butyl dicarbonate 22.5 g (101 mmol) in THF (150 mL) was added dropwise to a solution of 2,2′-(Ethylenedioxy)bis(ethylamine) 30 mL (202 mmol) in THF (150 mL) at 0 ºC. After the addition, the mixture was allowed to reach r.t. and was stirred overnight. The solvents were removed under reduced pressure, the resulting crude

was redisolved in DI water and filtered on celite. The aqueous phase was washed with PET (3 x 150 mL), then the product was extracted with AcOEt (3 x 150 mL), the combined organic layer was dried with dry Na_2SO_4 and filtered. The solvents were removed under reduced pressure, yielding the product as a yellow liquid (12.3 g, 49 %). **^{1}H-NMR** (400 MHz, $CDCl_3$) δ: 5.14 (m, 1H), 3.60 (s, 4H), 3.55-3.49 (m, 4H), 3.30 (m, 2H), 2.86 (t, *J* = 5.2 Hz, 2H), 1.43 (s, 9H), 1.29 (m, 2H) ppm.

Linker-FeNPs (**21**)

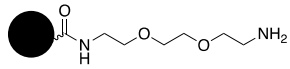

21

To a solution of 500.0 mg (0.4 mmol) of FeNPs-TEPSA in 20.0 mL of DMF, 191.7 mg (0.6 mmol) of EDC, 68.2 mg (0.6 mmol) of NHS and 174 µl Et_3N were added. The mixture was stirred at 0 ºC for 1 h. Then, tert-butyl (2-(2-(2-aminoethoxy)ethoxy)ethyl)carbamate 147 mg were added and the resulting mixture was stirred at r.t. overnight. The magnetic decantation was performed and washes with DI water, methanol and diethyl ether were performed. This gave 289.0 mg of CNDs-FeNPs-TEPSA as a brown solid. Afterwards, trifluoroacetic acid (TFA, 25 mL) was added to a solution of **21** (25.0 mg in CH_2Cl_2 (25 mL). The mixture was stirred at r.t. overnight. Then, toluene (50 mL) was added and the solvents were removed with reduced pressure, obtaining a brown solid. After, the magnetic decantation was performed and washes with DI water, methanol and diethyl ether were performed. This gave 15.0 mg of Linker-FeNPs-TEPSA as a brown solid.

CNDs-Linker-FeNPs (**22**)

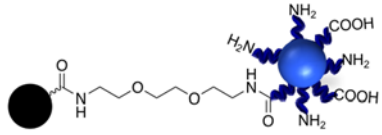

22

To a solution of 20.0 mg (0.003 mmol) of Linker-FeNPs in 5.0 mL of DMF, 0.8 mg (0.004 mmol) of EDC, 0.5 mg (0.004 mmol) of NHS and 20 µl Et_3N were added. The mixture was stirred at 0 ºC for 1 h. CNDs 3.4 mg were added and the resulting mixture was stirred at r.t. overnight. The magnetic decantation was performed and washes with DI water, methanol and diethyl ether were performed. This gave 26.0 mg of CNDs-Linker-FeNPs-TEPSA as a brown solid.

2'-Succinyltaxol (**25**)

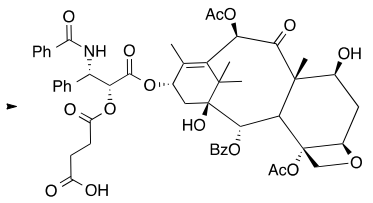

25

Synthesis of 2'-Succinyltaxol.[175] A solution of 100.0 mg (0.1 mmol) of taxol, 152.0 mg (1.5 mmol) of succinic anhydride in 2.4 mL of pyridine was stirred for 3 h at room temperature. The mixture of pyridine was evaporated to dry in vacuum. The residue was treated with 20.0 mL of water, stirred for 20 min, and filtered. The precipitate was dissolved in acetone, water was slowly added, and the tine crystals were collected. This gave 67.0 mg (59%) of white crystals.**^{1}H-NMR** ($CDCl_3$), δ: 1.13 (s, 3H), 1.22 (s, 3H), 1.67 (s, 3H), 1.91 (s, 3H), 2.21 (s, 3H), 2.60 (m, 4H), 3.80 (d, J = 7.2 Hz, 1H), 4.19 (d, J = 8.8 Hz, 1H), 4.30 (d, J = 8.4 Hz, 1H), 4.42 (dd, J = 4.4, 10.8 Hz, 1H), 4.97 (d, J = 8.0 Hz, 1H), 5.53 (d, J = 3.6 Hz, 1H), 5.68 (d, J = 7.2 Hz, 1H), 5.97 (dd, J = 3.2, 9.2 Hz, 1H), 6.23 (t, J = 10.0 Hz, 1H), 6.29 (s, 1H), 7.02 (d, J = 8.8 Hz, 1H), 7.35 (m, 1H), 7.40 (m, 2H), 7.42 (m, 2H), 7.48 (m, 2H), 7.49 (m, 1H), 7.51 (m, 2H), 7.61 (m, 1H), 7.74 (dd, J = 1.2, 8.3 Hz, 2H), 8.13 (dd, 2H). MS (IE^+), *m/z*: 953.3 (M^+).

CNDs-PTX (**26**)

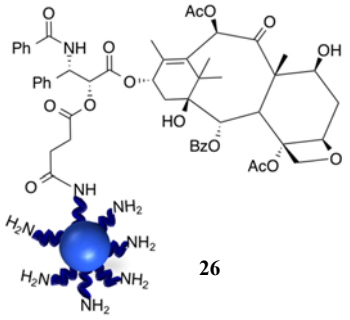

26

Synthesis of CNDs-PTX. To a solution of 100.0 mg (0.1 mmol) of 2'-succinyltaxol in 5.0 mL of DMF, 30.0 mg (0.2 mmol) of EDC, and 18.0 mg (0.2 mmol) of NHS were added. The mixture was stirred at 0 ºC for 1 h. CNDs 40.0 mg were added and the resulting mixture was stirred at r.t. overnight. The solvent was removed under reduce pressure. The crude product was isolated and chromatographed by size exclusion chromatography 100% MeOH. This gave 90.0 mg of CNDs-PTX yellow powder.

CNDs-PTX-Cy5 (**27**)

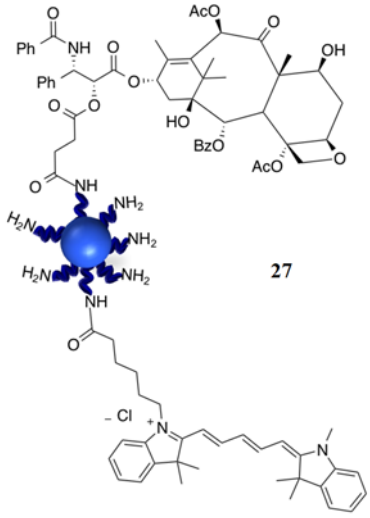

27

Synthesis of CNDs-PTX-Cy5. A solution of 50.0 mg of CNDs-PTX and 2.5 mg of cyanime5 NHS in 5.0 mL of DMF was stirred at r.t. overnight. The solvent was removed under reduce pressure. The crude was diluted with water and was filtered through a 0.1 μm microporous membrane separating a blue solution that was dialyzed against pure water through a dialysis membrane for 1 day. The aqueous solution of CNDs-PTX-Cy5 was lyophilized giving 14.0 mg of a bluish solid.

CNDs-CBL (**29**)

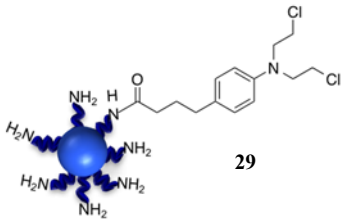

29

Synthesis of CNDs-CBL. To a solution of 32.0 mg (0.1 mmol) of chlorambucil in 5.0 mL of DMF, 30.0 mg (0.2 mmol) of EDC, and 18.0 mg (0.2 mmol) of NHS were added. The mixture was stirred at 0 ºC for 1 h. CNDs 40.0 mg were added and the resulting mixture was stirred at r.t. overnight. The solvent was removed under reduce pressure. The crude product was isolated and chromatographed by size exclusion chromatography 100% MeOH. This gave 60.0 mg of CNDs-CBL yellowish powder.

Labeling HSA-Cy7 (**32**)

32

Labeling of HSA with Cy7 (HSA-Cy7). The labeling procedure was carried out following the protocol recommended by the supplier. The dye dissolved in DMF at 10 $mg \cdot mL^{-1}$ was added to the HSA protein previously dissolved in sodium bicarbonate buffer (100 mM, pH=8.5) at 10 $mg \cdot mL^{-1}$, and the mixture was incubated at 25 °C under gentle stirring for 5 h. After that, unreacted Cy7 dye was separated from labelled HSA by size exclusion chromatography on Sephadex G-25 using a PD-10 column and using HEPES buffer (100 mM, pH=8.5) for the elution of the HSA-Cy7 fraction. This fraction was then washed with HEPES buffer by using amicon filters (30 kDa cutoff) to remove remaining free Cy7 molecules, until no free Cy7 was found in the filtrates, as checked by UV-Vis spectroscopy. Finally, the purified HSA-Cy7 solution was stored at 4 °C until use. By absorption spectroscopy the degree of labelling (DOL), that is the average number of fluorophore molecules linked to a protein molecule, was determined to be ca. 1.2.

HSA-Cy7@CNDs (**33**)

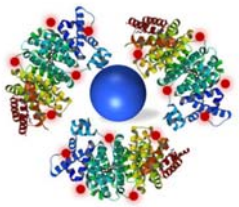

33

Coating of CNDs with HSA-Cy7. The labelled protein HSA-Cy7 was attached to the surface of the CNDs through natural adsorption, just by mixing the protein solution with the CNDs solution and leave them to interact overnight under gentle stirring at room temperature. In order to get a full corona of HSA-Cy7 proteins around the CNDs, that is for achieving the maximum coverage of the CNDs surface, several samples were prepared with increasing amounts of HSA-Cy7 while maintaining constant the concentration of CNDs (100 µL-aliquots of a CNDs solution at 5 $mg \cdot mL^{-1}$). The range studied was 0.01, 0.05, 0.1, 0.5, 1.0, and 5.0 nmol of protein per mg of CNDs. After incubation overnight, all the samples were purified by a PD-10 column to remove the excess of HSA-Cy7 non-adsorbed strongly on the CNDs surface. UV-Vis spectra of the samples were measured observing an increase of the band of Cy7 at 750 nm for the samples with higher amount of HSA-Cy7 adsorbed. However, the last two samples presented almost identical spectra which indicated that we reached the saturation point of the CND surface at 1.0 nmol HSA per mg CNDs. This value was selected as the optimum for the maximum coverage and a larger sample was then

prepared under this condition. The purified HSA-Cy7@CNDs sample was kept at 4 °C until use.

ii. Methods

Procedure of Kaiser test.[41] The free amino groups of the CNDs were determined using a commercially kit of Kaiser test, which is based on the intensive blue colour is generated by reaction of ninhydrin with free primary amines generating an intense blue color that is measured spectrophotometrically. 0.3 mg of CNDs were weight and the following solution reagents were added: 75 µL of solution 1 (80 g of phenol in 20 mL of ethanol), 100 µL of solution of 2 (2 mL of KCN 1 mM in water in 98 mL of pyridine), and 75 µL of solution 3 (1 g of ninhydrin in 20 mL of ethanol). Then, the mixture was heated at 120 ºC for 10 min, and finally diluted with ethanol 60 % in water up to a final volume of 3 mL. For the quantitative determination of the free amino groups on the surface of the nanoparticles the absorbance was recorded at 570 nm (A_{570}), setting the zero on the blank without sample. The following equation (**Equation 1**) gives the ratio between the moles of the amine moiety and the weight of the sample:

Equation 1
$$\mu mol/g = \frac{A_{570} \cdot V \cdot 10^6}{\varepsilon \cdot m}$$

where A_{570} is the absorbance at 570 nm, V the final volume after dilution (3 mL), ε is the molar extinction coefficient (15000 $M^{-1}cm^{-1}$), m is the exact mass of CNDs weighted and 10^6 is the correction factor to obtain the grade of amines in $\mu mol \cdot g^{-1}$.

Procedure of FL Quantum yield.[135] The quantum yield of the as-synthesized CNDs was determined by a comparative method using quinine sulfate in 0.1 M H_2SO_4 (QY= 54 %) as reference standard. To calculate relative values of QY five concentrations of CNDs in milli-Q water and quinine in 0.1 M H_2S0_4 were prepared. Afterwards, absorbance values at 300 nm were measured and the fluorescence intensity of each sample at an excitation wavelength of 300 nm was recorded. The integrated area under the PL curve in the wavelength range from 310 nm to 552 nm was calculated. Then, the QY was calculated using the following equation (**Equation 2**).

Equation 2
$$. \Phi_{f,s} = \Phi_{f,st} \cdot \frac{F_s}{F_{st}} \cdot \frac{f_{st}}{f_s} \cdot \frac{n_s^2}{n_{st}^2}$$

where the subscripts S and ST denote sample and standard, Φ is the fluorescence quantum yield, *F* is the integral PL, *f* is the absorption factor (f=1-$10^{-A(\square ex)}$, and *n* is the refractive index of the solvent (n = 1.33).

Procedure of conductimetric titration.[163] A solution of 0.01M NaOH was prepared and 27 mg of FeNPs-TEPSA were weighted in a beaker. The sample was titrated with a 0.01–0.05 M NaOH solution with continuous stirring with a magnetic stirrer and the conductometry was measured along the titration. Then, it was plotted the curve

of the conductimetric titration and the amount of COOH groups on the surface was calculated from the break in the curve with the following equation (**Equation 3**).

Equation 3 $$\text{COOH mol/g} = \frac{\text{N} \cdot \text{V}}{W}$$

Where N and V are the concentration and volume of NaOH titrant, respectively, and *W* is the solid content weight of the magnetic nanoparticles.

Procedure of Bradford assay. The amount of HSA protein bound to the CNDs was quantified by the colorimetric Bradford assay, which is based on the interaction between Coomassie brilliant blue and the arginine and aromatic residues in the protein. The calibration curve was carried out using standards of HSA (0, 2.5, 5, 10, 15, and 20 μg). The protocol used for the assay was the following: 150 μL of standards and HSA-Cy7@CNDs sample was placed into the wells of a 96-well plate, and 150 μL of Bradford reagent solution was added to each well. After 2 min the absorbance at 595 was recorded and the analytical signal (A_{595}) was calculated as the absorbance value of the standard or sample minus the absorbance of the zero standard. All the measurements were carried out in triplicate. It must be noted that the absorbance of both the CNDs and Cy7 is negligible at 595 nm, and therefore they do not interfere in the assay. The obtained calibration curve (A_{595} versus concentration of standards) was fitted to a linear equation, and the interpolation of the A_{595} signal of the sample from the calibration curve gave the concentration of HSA in $\mu g \cdot mL^{-1}$, which resulted to be (280 ± 13) μg of HSA per mg of CNDs.

Gel electrophoresis. To confirm changes on the charge after the formation of the protein corona, samples were subjected to gel electrophoresis (1.5 % agarose in 0.5x Tris-Borate-EDTA buffer). Samples mixed with 20% of a solution of TBE buffer containing 40% of glycerol were loaded into the wells of the gel. An electric field of 10 V/cm was applied for 15 min causing the migration of the nanoparticles towards the positive or negative pole depending of the NP charge. Images of the gel were taken under visible and UV light to visualize the position of the bands corresponding to the naked or protein corona-coated CNDs.

Particle stability. CNDs were incubated in Dulbecco's modified Eagle's *medium* (DMEM) medium completed with 10% heat-inactivated fetal calf serum (FBS), 2 mM L-glutamine(Gibco), 100 $U \cdot mL^{-1}$penicillin and 100 $\mu g \cdot mL^{-1}$ streptomycin (Gibco). The incubation was performed at 37 ºC and 5 % CO_2 in a humidified atmosphere at 0 h, 24 h, 48 h and 72 h to assess stability. The particles were subsequently re-analyzed by UV-Vis absorption spectra.

Cell culture and counting. Human umbilical vein endothelial cells (HUVEC, AIDS reagents NIH) were cultured in F12K media supplemented with 0.1 $mg \cdot mL^{-1}$ heparin (sigma) and 30 $\mu g \cdot mL^{-1}$ endothelial cell growth supplement (sigma). The rest of the

cells were cultured in DMEM media supplemented with 1mM sodium pyruvate at 37 ºC and 5 % CO_2 in tissue culture-treated 75 cm_2-flasks from Nunc. For cell passage, adherent cells were lifted from the flasks by incubation at 37 ºC with trypsin-EDTA solution 1x (2.5 g porcine trypsin and 0.2 g EDTA (por) 4 Na per liter of Hanks' Balanced Salt from Sigma), span at 1000 g for 5 min and the pellet re-suspended in 1 ml media. For cell counting, the cell suspension was serially diluted 1:10 in PBS and 1:2 in the exclusion dye Trypan Blue solution (0.4 % in 0.8 % sodium chloride and 0.1 % potassium phosphate, dibasic from Sigma Aldrich), 10 µL of the diluted cell suspension was counted in a hemocytometer chamber under transmitted light in an inverted microscope (DMIL, Leica).

Cell viability Assay. Cell viability of adherent human cell lines was measured with the colorimetric MTT assay. 4 x 10^3 PC3 (prostate cancer), 4x10^3 A-549 (small cell lung carcinoma), 2.5 x 10^3 C33-A (cervix carcinoma), 2.5 x 10^3 HeLa (cervix carcinoma), 4 x 10^3MDA-MB-231 (breast adenocarcinoma), 10 x 10^3MCF-7 (breast adenocarcinoma) cells were seeded in 200µL media per well in 96-well plates and cultured for 24 h at 37 ºC and 5 % CO_2. Then, they were incubated for 72 h with CNDs-PTX at the concentrations of 1 µg·mL^{-1}, 10 µg·mL^{-1}, 25 µg·mL^{-1}, 50 µg·mL^{-1}, 150 µg·mL^{-1}, 300 µg·mL^{-1}, 450 µg·mL^{-1}, 600 µg·mL^{-1}, 750 µg·mL^{-1}, 900 µg·mL^{-1}, 1 mg·mL^{-1} in 100 µL media at 37 ºC and 5 % CO_2 in a humidified atmosphere. Cells were washed twice with 100 µL incomplete media and incubated for 30-60 min at 37 ºC and 5 % CO_2 with 100 µL media containing MTT at the dilution of 1:20. The formazan crystals produced by the mitochondrial processing of MTT were dissolved in 100 µL DMSO. Absorbance of MTT product was detected in a micro plate reader (Genios Pro, TECAN) at 550 nm. Data are expressed as a percentage of absorbance of treated cells related to the untreated control cells and represented as means of quadruplicates ± SD.

Flow cytometry. Cells cultured in the presence of serum keeps proliferating while in the absence of serum they stop proliferating, therefore, the protocol was slightly different in the case of the study of the uptake kinetic in the presence or the absence of FBS. In the presence of FBS, 4.5 × 10^4 PC-3 cells were seeded in 48-well plates and cultured in complete medium for 6 days. In order to reach the same cell number independently of the studied incubation time (3 h, 6 h, 12 h, 24 h, 48 h and 72 h) and carry out the FACS measurements of all the samples at the same day, at specific times the medium was replaced by 200 µL of complete medium containing 300 µg·mL^{-1} CND or HSA-Cy7@CND, and cells were incubated at 37 ºC and 5 % CO_2. For the uptake kinetic study in the absence of FBS, 1.8 × 10^5 cells were seeded in 48-well plates and cultured in complete medium for 1 day. Afterwards, complete medium was aspirated, wells were washed twice with 500 µL serum-free medium and then 200 µL of complete medium containing 300 µg·mL^{-1} CND or HSA-Cy7@CND were added. Cells were incubated at 37 ºC and 5 % CO_2 for 3 h, 6 h, 12 h, 24 h, 48 h and 72 h. Triplicates were done per each condition. In both cases, after finishing the incubation time cells were washed carefully with PBS. Then, cells were lifted by trypsinization at 37 ºC, transferred to a 96-well round bottom plate, span at 1,500 x g for 5 min and

washed once with PBS. Finally, cells were resuspended in 200 µL of PBS with 0.09 % of sodium azide, put in ice and measured immediately. For the measurements, 10,000 cells were analyzed by the flow cytometer collecting two channels. The channel 1 (laser line: 405 nm, band pass filter: 450/50) for measuring the fluorescent signal from the CNDs, and the channel 2 (laser line: 633 nm, long pass filter: 735LP, band pass filter: 780/60) for collecting the fluorescence from the labeled protein Cy7-HSA. Prior to any sample analysis the manufacturer's quality control (QC) checks and calibration using CS&T™ beads (BD Biosciences) were performed, in order to evaluate the system performance and adjust the settings against the baseline values.

Real-time Cell Electronic Sensing (RT-CES).[203] For time-dependent cell response profiling, 100 µl of media was added to the 16 well-electronic plates (E-Plates). Following the baseline reading 100 µl of cell suspension was added to the wells and allowed to incubate firstly at room temperature for 30 min and then, inserted on the RT-CES for continuous recording of impedance as reflected by the cell index. All the measurements by the RT-CES were performed inside an incubator at 37 ºC, 5 % CO_2 and humidified atmosphere. After 24 hours of incubation the cells were treated with different concentrations of CNDs-PTX. Data was collected every five minutes for the duration of 8 hours after compound addition to capture the short-term response, followed by measurements every 30 min for 72 h and every 15 min for 24 h in order to capture the long-term response. To quantify cell status based on the measured cell-electrode impedance, a parameter termed Cell Index is derived, according to the following **Equation 4**:

Equation 4
$$CI = max\left(\frac{Rcell(fi)}{Rb(fi)} - 1\right)$$

Where Rb(f) and Rcell(f) are the frequency dependent electrode resistances (a component of impedance) without cells or with cell present, respectively. N is the number of the frequency points at which the impedance is measured. Thus, Cell Index is a quantitative measure of the status of the cells in an electrode-containing well. Under the same physiological conditions, more cells attached on to the electrodes leads to larger Rcell(f) value, leading to a larger value for Cell Index. Furthermore, for the same number of cells present in the well, a change in the cell status such as morphology will lead to a change in the Cell Index. A "Normalized Cell Index" at a given time point is calculated by dividing the Cell Index at the time point by the Cell Index at a reference time point. Thus, the Normalized Cell Index is 1 at the reference time point.

Cell uptake. The human breast carcinoma MDA-MB-231cells were seeded in 96-well plates with a density of 1 x 10^4 cells per well, and cultured for 72 h at 37 ºC and 5 % CO_2. The original medium was removed and replaced with media containing CNDs with a concentration of 100 µg·mL^{-1}. After incubation for, 1 h, 2 h, 4 h, and 24 h, the cells were washed twice with 100 µL media. The cell fluorescence was measured by excitation at 340 nm and emission at 448/5 nmin a Genios Pro Tecan plate reader to

assess the cellular uptake of the CNDs. Untreated cells served as a control. Each sample was tested in triplicate wells.

Statistical analyses. Comparison of two-variable data were performed using two-way ANOVA with Bonferroni adjustment. P values of less than 0.05 were considered statistically significant. GraphPad Prism, GraphPad Software, La Jolla, CA.

Microscopy. 2 x 10^4 C33-A cells per well were seeded in an 8-well chamber slide (Millicell EZslide, Millipore) and cultured for 1 day. Supernatants were replaced by 200 µL media alone or media containing 300 $\mu g \cdot ml^{-1}$, of CNDs, then incubated for 24 h at 37 ºC and 5 % CO_2. Cells were washed twice with sterile PBS prior to fixation with sterile PBS containing 4% paraformaldehyde for 15min at room temperature. Wells were disassembled, cells were washed twice with PBS and, the slide was mounted with 1 drop mounting media (DAKO) and a 1.5 coverslip (24x60mm). For morphological studies of apoptosis, 5 x 10^3 A-549 cells per well were seeded onto sterile 1.5 round coverslips in a 48-well plate, cultured for 3 days and incubated with media alone or media containing 20 $ng \cdot ml^{-1}$ CNDs-Cy5-PTX, or CNDs-Cy5 for 24 h at 37 ºC and 5 % CO_2. Cells were washed and fixed as described above. After PBS washing, nuclei were stained by incubation with 125 $ng \cdot mL^{-1}$ DAPI (4',6-diamidino-2-phenylindole.in PBS for 10 min at room temperature. Cells were washed again and the round coverslip was mounted onto a slide with 1 drop mounting media (DAKO). The mounted slides were let to harden overnight at 4 ºC. Images were taken in a confocal microscope (LSM 500 meta, Zeiss), plan-Apochromat 63x/1.40 Oil DIC M27 objective and with laser 405 nm/BP 420-605 nm filter, or laser 633 nm/BP 650-755 filter.

In vitro drug Release. The THP-1 cells were seeded in 24-well plates with a density of 1.6 x 10^6 cells per well, which were cultured for 24 h at 37 ºC in a 5 % CO_2 air atmosphere in a humidified incubator. Afterwards, the original medium was replaced with medium containing CNDs-PTX with a concentration of 1 $mg \cdot mL^{-1}$. After incubation for 24 h, the cells were washed twice and re-suspended in PBS. Then the cell suspensions were lysed by three freeze/unfreeze cycles in liquid nitrogen and 15 min of sonication. The resulted lysate was passed through a centrifuge 3 KDa Amicon® filter, and the collected fraction was analyzed by fluorescence spectroscopy. Untreated cells served as control and blank simple.

Inverted BBB model. The electrode-filter side of wells were coated with 30 µL vitronectin (10 $\mu g \cdot mL^{-1}$) in sterile PBS by incubation for 2 h at 37 ºC in a humidified chamber and removed by washings with 50 µL PBS twice. Then we followed the protocol described previously.[209] Monodispersed HUVEC were seeded in the lower well at 22.5 x 10^3 cells in 150 µL complete media per well. The 2 halves of the plates were assembled according to the manufacturer's instructions and connected to the xCELLigence DP system to produce a time zero control for each plate and well. The

plates were then removed and inverted for 30 min at room temperature to prevent edge effects.[211] Following this, the CIM plates were incubated (still inverted) at 37 ºC overnight. Then, the plates were returned to the upright position and media added to the upper well. At this time, the plates were returned to the xCELLigence DP system (inside the incubator) and monitored for 3 days using the installed software. Data are expressed as an average ± SD (n=16). For the induction of tight junctions, when the signal reached a plateau at 70 h after plating, monodispersed C8-D1A (mouse astrocytes) were seeded in the upper well at 22.5 x 10^3 cells in 180 µL complete HUVEC media per well. Traces were followed automatically using the installed software to monitor the effects of astrocyte processed on electrical resistance of HUVEC monolayer for 24 h at 37 ºC and 5 % CO_2.

BBB model permeability assay. The CIM plate was removed from the xCELLigence DP system. 100 µL HUVEC complete media containing 500 $\mu g \cdot mL^{-1}$ CNDs, CNDs-DEGd, CNDs-PEG_{400}, Propidium iodide (+Control) and FITC-Dextran 10KDa (-Control) were added to the upper chamber of duplicate wells. Following 24 h-incubation at 37 ºC and 5 % CO_2, the contents of the upper and lower chamber were collected and the fluorescence was measured in a plate spectrophotometer.

References

(1) Hong, G.; Diao, S.; Antaris, A. L.; Dai, H. Carbon Nanomaterials for Biological Imaging and Nanomedicinal Therapy. *Chem. Rev.* **2015**, *115* (19), 10816–10906.

(2) Buzea, C.; Pacheco, I. I.; Robbie, K. Nanomaterials and Nanoparticles: Sources and Toxicity. *Biointerphases* **2007**, *2* (4), 17–71.

(3) Kroto, H. W.; Heath, J. R.; O'Brien, S. C.; Curl, R. F.; Smalley, R. E. C 60: Buckminsterfullerene. *Nature* **1985**, *318*, 162–163.

(4) Iijima, S. Helical Microtubules of Graphitic Carbon. *Nature* **1991**, *354*, 56–58.

(5) Novoselov, K. S.; Geim, A. K.; Morozov, S. V.; Jiang, D.; Zhang, Y.; Dubonos, S. V.; Grigorieva, I. V.; Firsov, A. A. Electric Field Effect in Atomically Thin Carbon Films. *Science (80-.).* **2004**, *306*, 666–669.

(6) Osswald, S.; Yushin, G.; Mochalin, V.; Kucheyev, S. O. Control of Sp 2 / Sp 3 Carbon Ratio and Surface Chemistry of Nanodiamond Powders by Selective Oxidation in Air. *J. am. Chem. Soc.* **2006**, *128* (10), 11635–11642.

(7) Braun, K.; Dunsch, L.; Pipkorn, R.; Bock, M.; Baeuerle, T.; Yang, S.; Waldeck, W.; Wiessler, M. Gain of a 500-Fold Sensitivity on an Intravital MR Contrast Agent Based on an Endohedral Gadolinium-Cluster-Fullerene-Conjugate: A New Chance in Cancer Diagnostics. *Int. J. Med. Sci.* **2010**, *7* (3), 136–146.

(8) X. Xu, R. Ray, Y. Gu, H.J. Ploehn, L. Gearheart, K. Raker, W. A. Scrivens. Electrophoretic Analysis and Purification of Fluorescent Single-Walled Carbon Nanotube Fragments. *J. Am. Chem. Soc.* **2004**, *126* (40), 12736–12737.

(9) Reed, M. A., Randall, J. N., Aggarwal, R. J., Matyi, T. M., Moore, T. M. and Wetsel, A. E. Observation of Discrete Electronic States in a Zero-Dimensional Semiconductor Nanostructure. *Phys. Rev. Lett.* **1988**, *60* (June), 535–537.

(10) Brus, L. E. Electron–electron and Electron-hole Interactions in Small Semiconductor Crystallites: The Size Dependence of the Lowest Excited Electronic State. *J. Chem. Phys.* **1984**, *80* (9), 4403–4409.

(11) A. Cayuela, M. L. Soriano, C. Cariilo-Carrion, M. V. Semiconductor and Carbon-Based Fluorescent. *Chem. Commun.* **2016**, *52* (7), 1311–1326.

(12) Lingling Li, Gehui Wu, Guohai Yang, Juan Peng, J. Z. and J.-J. Z. Focusing on Luminescent Graphene Quantum Dots: Current Status and Future Perspectives. *Nanoscale* **2013**, *5* (10), 4015–4039.

(13) Namdari, P.; Negahdari, B.; Eatemadi, A. Synthesis, Properties and Biomedical Applications of Carbon-Based Quantum Dots: An Updated Review. *Biomed. Pharmacother.* **2017**, *87* (88), 209–222.

(14) Wei, J.; Qiu, J. Unveil the Fluorescence of Carbon Quantum Dots. *Adv. Eng. Mater.* **2014**, *17*, 138–142.

(15) Sun, Y. P.; Zhou, B.; Lin, Y.; Wang, W.; Fernando, K. a S.; Pathak, P.; Meziani, M. J.; Harruff, B. a.; Wang, X.; Wang, H.; et al. Quantum-Sized Carbon Dots for Bright and Colorful Photoluminescence. *J. Am. Chem. Soc.* **2006**, *128* (24), 7756–7757.

(16) Song, Y.; Zhu, S.; Zhang, S.; Fu, Y.; Wang, L.; Zhao, X.; Yang, B. Investigation from Chemical Structure to Photoluminescent Mechanism: A Type of Carbon Dots from the Pyrolysis of Citric Acid and an Amine. *J. Mater. Chem. C* **2015**, *3* (23), 5976–5984.

(17) Yu, C.; Xuan, T.; Chen, Y.; Zhao, Z.; Sun, Z.; Li, H. A Facile, Green Synthesis of Highly Fluorescent Carbon Nanoparticles from Oatmeal for Cell Imaging. *J. Mater. Chem. C* **2015**, *3* (37), 9514–9518.

(18) Krysmann, M. J.; Kelarakis, A.; Dallas, P.; Giannelis, E. P. Formation Mechanism of Carbogenic Nanoparticles with Dual Photoluminescence Emission. *J. Am. Chem. Soc.* **2012**, *134* (2), 747–750.

(19) Yan, J. J.; Wang, Z. K.; Lin, X. S.; Hong, C. Y.; Liang, H. J.; Pan, C. Y.; You, Y. Z. Polymerizing Nonfluorescent Monomers without Incorporating Any Fluorescent Agent Produces Strong Fluorescent Polymers. *Adv. Mater.* **2012**, *24* (41), 5617–5624.

(20) Semaltianos, N. G. Nanoparticles by Laser Ablation. *Crit. Rev. Solid State Mater. Sci.* **2010**, *35* (2), 105–124.

(21) Geusic, J. E.; Marcos, H. M.; Van Uitert, L. G. Laser Oscillations in Nd-Doped Yttrium Aluminum, Yttrium Gallium and Gadolinium Garnets. *Appl. Phys. Lett.* **1964**, *4* (10), 182–184.

(22) Reyes, D.; Camacho, M.; Camacho, M.; Mayorga, M.; Weathers, D.; Salamo, G.; Wang, Z.; Neogi, A. Laser Ablated Carbon Nanodots for Light Emission. *Nanoscale Res. Lett.* **2016**, *11* (1), 424.

(23) Zhao, Q.-L.; Zhang, Z.-L.; Huang, B.-H.; Peng, J.; Zhang, M.; Pang, D.-W. Facile Preparation of Low Cytotoxicity Fluorescent Carbon Nanocrystals by Electrooxidation of Graphite. *Chem. Commun.* **2008**, No. 41, 5116.

(24) Xu, Y.; Liu, J.; Zhang, J.; Zong, X.; Jia, X.; Li, D.; Wang, E. Chip-Based Generation of Carbon Nanodots via Electrochemical Oxidation of Screen Printed Carbon Electrodes and the Applications for Efficient Cell Imaging and Electrochemiluminescence Enhancement. *Nanoscale* **2015**, *7* (21), 9421–9426.

(25) Liu, M.; Xu, Y.; Niu, F.; Gooding, J. J.; Liu, J. Carbon Quantum Dots Directly Generated from Electrochemical Oxidation of Graphite Electrodes in Alkaline Alcohols and the Applications for Specific Ferric Ion Detection and Cell Imaging. *Analyst* **2016**, *141* (9), 2657–2664.

(26) Liu, H.; Ye, T.; Mao, C. Fluorescent Carbon Nanoparticles Derived from Candle Soot. *Angew. Chemie - Int. Ed.* **2007**, *46* (34), 6473–6475.

(27) Yang, S.; Sun, J.; Li, X.; Zhou, W.; Wang, Z.; He, P.; Ding, G.; Xie, X.; Kang, Z.; Jiang, M. Large-Scale Fabrication of Heavy Doped Carbon Quantum Dots with Tunable-Photoluminescence and Sensitive Fluorescence Detection. *J. Mater. Chem. A* **2014**, *2* (23), 8660.

(28) Li, H.; He, X.; Liu, Y.; Huang, H.; Lian, S.; Lee, S. T.; Kang, Z. One-Step Ultrasonic Synthesis of Water-Soluble Carbon Nanoparticles with Excellent Photoluminescent Properties. *Carbon N. Y.* **2011**, *49* (2), 605–609.

(29) Zhu, H.; Wang, X.; Li, Y.; Wang, Z.; Yang, F.; Yang, X. Microwave Synthesis of Fluorescent Carbon Nanoparticles with Electrochemiluminescence Properties. *Chem. Commun.* **2009**, No. 34, 5118.

(30) Choi, Y.; Jo, S.; Chae, A.; Kim, Y. K.; Park, J. E.; Lim, D.; Park, S. Y.; In, I. Simple Microwave-Assisted Synthesis of Amphiphilic Carbon Quantum Dots from A3/B2 Polyamidation Monomer Set. *ACS Appl. Mater. Interfaces* **2017**, *9*, 27883–27893.

(31) Arcudi, F.; Dordevic, L.; Prato, M. Synthesis, Separation, and Characterization of Small and Highly Fluorescent Nitrogen-Doped Carbon Nanodots. *Angew. Chemie - Int. Ed.* **2016**, *55* (6), 2107–2112.

(32) Martindale, B. C. M.; Hutton, G. A. M.; Caputo, C. A.; Reisner, E. Solar Hydrogen Production Using Carbon Quantum Dots and a Molecular Nickel Catalyst. *J. Am. Chem. Soc.* **2015**, *137* (18), 6018–6025.

(33) Tyagi, A.; Tripathi, K. M.; Singh, N.; Choudhary, S.; Gupta, R. K. Green Synthesis of Carbon Quantum Dots from Lemon Peel Waste: Applications in Sensing and Photocatalysis. *RSC Adv.* **2016**, *6* (76), 72423–72432.

(34) Tang, L.; Ji, R.; Cao, X.; Lin, J.; Jiang, H.; Li, X.; Teng, K. S. Deep Ultraviolet Photoluminescence Graphene Quantum Dots. *ACS Nano* **2012**, *6* (6), 5102–5110.

(35) Lin, P. C.; Lin, S.; Wang, P. C.; Sridhar, R. Techniques for Physicochemical Characterization of Nanomaterials. *Biotechnol. Adv.* **2014**, *32* (4), 711–726.

(36) Vyazovkin, S. Thermogravimetric Analysis. *Charact. Mater.* **2012**, *1* (906).

(37) Mertens, G.; Elsen, J.; Veiga, M. R.; Aguiar, J.; Silva, A. S.; Carvalho, F.; Moropoulou, A.; Bakolas, A.; Bisbikou, K.; Goins, E. S.; et al. *Physical Principles of Electron Microscopy*; 2006; Vol. 36.

(38) Thomson, G. P.; Reid, A. Diffraction of Cathode Rays by a Thin Film. *Nature*. 1927, pp 890–890.

(39) McNeil, S. E. *Characterization of Nanoparticles Intended for Drug Delivery*; 2011; Vol. 79.

(40) Hillenkamp, F.; Karas, M. Matrix-Assisted Laser Desorption/ionization Mass Spectrometry of Biopolymers. *Anal. Chem.* **1991**, *63* (24), 1193–1203.

(41) Kaiser, E.; Colescot, R.; Bossinge, C.; Cook, P. Color Test for Dectection of Free Terminal Amino Groups in the Solid-Phase Synthesis of Peptides. *Anal. Biochem.* **1970**, *34*, 595–598.

(42) Baker, S. N.; Baker, G. A. Luminescent Carbon Nanodots: Emergent Nanolights. *Angew. Chemie Int. Ed.* **2010**, *49* (38), 6726–6744.

(43) Arcudi, F.; Đorđević, L.; Prato, M. Synthesis, Separation, and Characterization of Small and Highly Fluorescent Nitrogen-Doped Carbon NanoDots. *Angew. Chem. Int. Ed. Engl.* **2016**, *55* (6), 2107–2112.

(44) Travlou, N. A.; Secor, J.; Bandosz, T. J. Highly Luminescent S-Doped Carbon Dots for the Selective Detection of Ammonia. *Carbon N. Y.* **2017**, *114*, 544–556.

(45) Zheng, X. T.; Ananthanarayanan, A.; Luo, K. Q.; Chen, P. Glowing Graphene Quantum Dots and Carbon Dots: Properties, Syntheses, and Biological Applications. *Small* **2015**, *11* (14), 1620–1636.

(46) Lim, S. Y.; Shen, W.; Gao, Z. Carbon Quantum Dots and Their Applications. *Chem. Soc. Rev.* **2014**, *44* (1), 362–381.

(47) Ehrat, F.; Bhattacharyya, S.; Schneider, J.; Löf, A.; Wyrwich, R.; Rogach, A. L.; Stolarczyk, J. K.; Urban, A. S.; Feldmann, J. Tracking the Source of Carbon Dot Photoluminescence: Aromatic Domains versus Molecular Fluorophores. *Nano Lett.* **2017**, *17* (12), 7710–7716.

(48) Liu, R.; Wu, D.; Liu, S.; Koynov, K.; Knoll, W.; Li, Q. An Aqueous Route to Multicolor Photoluminescent Carbon Dots Using Silica Spheres as Carriers. *Angew. Chemie - Int. Ed.* **2009**, *48* (25), 4598–4601.

(49) Li, X.; Wang, H.; Shimizu, Y.; Pyatenko, A.; Kawaguchi, K.; Koshizaki, N. Preparation of Carbon Quantum Dots with Tunable Photoluminescence by Rapid Laser Passivation in Ordinary Organic Solvents. *Chem. Commun.* **2011**, *47* (3), 932–934.

(50) Hu, S.-L.; Niu, K.-Y.; Sun, J.; Yang, J.; Zhao, N.-Q.; Du, X.-W. One-Step Synthesis of Fluorescent Carbon Nanoparticles by Laser Irradiation. *J. Mater. Chem.* **2009**, *19* (4), 484–488.

(51) Haase, M.; Schäfer, H. Upconverting Nanoparticles. *Angew. Chemie - Int. Ed.* **2011**, *50* (26), 5808–5829.

(52) Cao, L.; Wang, X.; Meziani, M. J.; Lu, F.; Wang, H.; Luo, P. G.; Lin, Y.; Harruff, B. A.; Veca, L. M.; Murray, D.; et al. Carbon Dots for Multiphoton Bioimaging. *J. Am. Chem. Soc.* **2007**, *129* (37), 11318–11319.

(53) Barati, A.; Shamsipur, M.; Abdollahi, H. A Misunderstanding about Upconversion Luminescence of Carbon Quantum Dots. *J. Iran. Chem. Soc.* **2015**, *12* (3), 441–446.

(54) De, B.; Karak, N. Recent Progress in Carbon Dot–metal Based Nanohybrids for Photochemical and Electrochemical Applications. *J. Mater. Chem. A* **2017**, *5* (5), 1826–1859.

(55) Ambrosi, A.; Chua, C. K.; Bonanni, A.; Pumera, M. Electrochemistry of Graphene and Related Materials. *Chem. Rev.* **2014**, *114* (14), 7150–7188.

(56) Zhao, J.; Chen, G.; Zhu, L.; Li, G. Graphene Quantum Dots-Based Platform for the Fabrication of Electrochemical Biosensors. *Electrochem. commun.* **2011**, *13* (1), 31–33.

(57) Yang, S. T.; Wang, X.; Wang, H.; Lu, F.; Luo, P. G.; Cao, L.; Meziani, M. J.; Liu, J. H.; Liu, Y.; Chen, M.; et al. Carbon Dots as Nontoxic and High-Performance Fluorescence Imaging Agents. *J. Phys. Chem. C* **2009**, *113* (42), 18110–18114.

(58) Yang, S.-T.; Cao, L.; Luo, P. G.; Lu, F.; Wang, X.; Wang, H.; Meziani, M. J.; Liu, Y.; Qi, G.; Sun, Y.-P. Carbon Dots for Optical Imaging in Vivo. *J. Am. Chem. Soc.* **2009**, *131* (32), 11308–11309.

(59) Choi, Y.; Kim, S.; Choi, M. H.; Ryoo, S. R.; Park, J.; Min, D. H.; Kim, B. S. Highly Biocompatible Carbon Nanodots for Simultaneous Bioimaging and Targeted Photodynamic Therapy in Vitro and in Vivo. *Adv. Funct. Mater.* **2014**, *24* (37), 5781–5789.

(60) Tsoi, K. I. M. M.; Dai, Q. I. N.; Alman, B. A.; Chan, W. C. W. Are Quantum Dots Toxic? Exploring the Discrepancy Between Cell Culture and Animal Studies. *Acc. Chem. Res.* **2012**.

(61) Murphy, C. J.; Gole, A. M.; Stone, J. W.; Sisco, P. N.; Alkilany, A. M.; Goldsmith, E. C.; Baxter, S. C. Gold Nanoparticles in Biology: Beyond Toxicity to Cellular Imaging. *Acc. Chem. Res.* **2008**, *41* (12), 1721–1730.

(62) Mironava, T.; Hadjiargyrou, M.; Simon, M.; Jurukovski, V.; Rafailovich, M. H. Gold Nanoparticles Cellular Toxicity and Recovery: Effect of Size, Concentration and Exposure Time. *Nanotoxicology* **2010**, *4* (1), 120–137.

(63) Sung, J. H.; Lee, E. J.; Lee, J. H.; Yu, I. J. Lung Function Changes in Sprague-Dawley Rats After Prolonged Inhalation Exposure to Silver Nanoparticles. *Inhal. Toxicol.* **2008**, *20* (6), 567–574.

(64) Liu, Z.; Tabakman, S. M.; Chen, Z.; Dai, H. Preparation of Carbon Nanotube Bioconjugates for Biomedical Applications. *Nat. Protoc.* **2009**, *4* (9), 1372–1381.

(65) Jeong, K.; Kim, Y.; Kang, C. S.; Cho, H.-J.; Lee, Y.-D.; Kwon, I. C.; Kim, S. Nanoprobes for Optical Bioimaging. *Opt. Mater. Express* **2016**, *6* (4), 1262.

(66) Hasegawa, U.; Nomura, S. I. M.; Kaul, S. C.; Hirano, T.; Akiyoshi, K. Nanogel-Quantum Dot Hybrid Nanoparticles for Live Cell Imaging. *Biochem. Biophys. Res. Commun.* **2005**, *331* (4), 917–921.

(67) Dykman, L. A.; Khlebtsov, N. G. Gold Nanoparticles in Biology and Medicine: Recent Advances and Prospects. *Acta Naturae* **2011**, *3* (2), 34–55.

(68) Bajaj, P.; Mikoryak, C.; Wang, R.; Bushdiecker II, D. K.; Memon, P.; Draper, R. K.; Dieckmann, G. R.; Pantano, P.; Musselman, I. H. A Carbon Nanotube-Based Raman-Imaging Immunoassay for Evaluating Tumor Targeting Ligands. *Analyst* **2014**, *139* (12), 3069–3076.

(69) Chen, W.; Yi, P.; Zhang, Y.; Zhang, L.; Deng, Z.; Zhang, Z. Composites of Aminodextran-Coated Fe 3 O 4 Nanoparticles and Graphene Oxide for Cellular Magnetic Resonance Imaging. *ACS Appl. Mater. Interfaces* **2011**, *3* (10), 4085–4091.

(70) Georgakilas, V.; Tagmatarchis, N.; Pantarotto, D.; Bianco, A.; Briand, J.-P.; Prato, M. Amino Acid Functionalisation of Water Soluble Carbon Nanotubes. *Chem. Commun.* **2002**, No. 24, 3050–3051.

(71) Liu, W.; Wei, J.; Chen, Y.; Huo, P.; Wei, Y. Electrospinning of poly(L-Lactide) Nanofibers Encapsulated with Water-Soluble Fullerenes for Bioimaging Application. *ACS Appl. Mater. Interfaces* **2013**, *5* (3), 680–685.

(72) Chen, Y. H.; Tsai, C. Y.; Huang, P. Y.; Chang, M. Y.; Cheng, P. C.; Chou, C. H.; Chen, D. H.; Wang, C. R.; Shiau, A. L.; Wu, C. L. Methotrexate Conjugated to Gold Nanoparticles Inhibits Tumor Growth in a Syngeneic Lung Tumor Model. *Mol. Pharm.* **2007**, *4* (5), 713–722.

(73) Wang, F.; Wang, Y.; Dou, S.; Xiong, M.; Sun, T.; Wang, J.; Al, W. E. T. Doxorubicin-Tethered Responsive Gold Nanoparticles Facilitate Intracellular Drug Delivery for Overcoming Multidrug Resistance in Cancer Cells. *ACS Nano* **2011**, *5* (5), 3679–3692.

(74) Shenoy, D.; Fu, W.; Li, J.; Crasto, C.; Jones, G.; DiMarzio, C.; Sridhar, S.; Amiji, M. Surface Functionalization of Gold Nanoparticles Using Hetero-Bifunctional Poly(ethylene Glycol) Spacer for Intracellular Tracking and Delivery. *Int. J. Nanomedicine* **2006**, *1* (1), 51–57.

(75) Olerile, L. D.; Liu, Y.; Zhang, B.; Wang, T.; Mu, S.; Zhang, J.; Selotlegeng, L.; Zhang, N. Near-Infrared Mediated Quantum Dots and Paclitaxel Co-Loaded Nanostructured Lipid Carriers for Cancer Theragnostic. *Colloids Surfaces B Biointerfaces* **2017**, *150*, 121–130.

(76) Liu, Z.; Chen, K.; Davis, C.; Sherlock, S.; Cao, Q.; Chen, X.; Dai, H. Drug Delivery with Carbon Nanotubes for in Vivo Cancer Treatment. *Cancer Res.* **2008**, *68* (16), 6652–6660.

(77) Yan, L.; Zhao, F.; Li, S.; Hu, Z.; Zhao, Y. Low-Toxic and Safe Nanomaterials by Surface-Chemical Design, Carbon Nanotubes, Fullerenes, Metallofullerenes, and Graphenes. *Nanoscale* **2011**, *3* (2), 362–382.

(78) Zhu, Y.; Murali, S.; Cai, W.; Li, X.; Suk, J. W.; Potts, J. R.; Ruoff, R. S. Graphene and Graphene Oxide: Synthesis, Properties, and Applications. *Adv. Mater.* **2010**, *22* (35), 3906–3924.

(79) Yang, X.; Zhang, X.; Liu, Z.; Ma, Y.; Huang, Y.; Chen, Y. High-Efficiency Loading and Controlled Release of Doxorubicin Hydrochloride on Graphene Oxide. *J. Phys. Chem. C* **2008**, *112* (45), 17554–17558.

(80) Zakharian, T. Y.; Seryshev, A.; Sitharaman, B.; Gilbert, B. E.; Knight, V.; Wilson, L. J. A Fullerene - Paclitaxel Chemotherapeutic : Synthesis , Characterization , and Study of Biological Activity in Tissue Culture. *J. am. Chem. Soc.* **2005**, *127*, 12508–12509.

(81) Lockman, P. R.; Mumper, R. J.; Khan, M. A.; Allen, D. D. Nanoparticle Technology for Drug Delivery Across the Blood-Brain Barrier. *Drug Dev. Ind. Pharm.* **2002**, *28* (1), 1–13.

(82) Saraiva, C.; Praça, C.; Ferreira, R.; Santos, T.; Ferreira, L.; Bernardino, L. Nanoparticle-Mediated Brain Drug Delivery: Overcoming Blood-Brain Barrier to Treat Neurodegenerative Diseases. *J. Control. Release* **2016**, *235*, 34–47.

(83) Geng, Z.; Zhang, H.; Xiong, Q.; Zhang, Y.; Zhao, H.; Wang, G. A Fluorescent Chitosan Hydrogel Detection Platform for the Sensitive and Selective Determination of Trace Mercury(ii) in Water. *J. Mater. Chem. A Mater. energy Sustain.* **2015**, *3*, 19455–19460.

(84) Cao, L.; Wang, X.; Meziani, M. J.; Lu, F.; Wang, H.; Luo, P. G.; Harruff, B. A.; Veca, L. M.; Murray, D.; Xie, S.; et al. Carbon Dots for Multiphoton Bioimaging. *J. am. Chem. Soc.* **2007**, *129* (37), 9–11.

(85) Ray Chowdhuri, A.; Tripathy, S.; Haldar, C.; Roy, S.; Sahu, S. K. Single Step Synthesis of Carbon Dot Embedded Chitosan Nanoparticles for Cell Imaging and Hydrophobic Drug Delivery. *J. Mater. Chem. B* **2015**, *3* (47), 9122–9131.

(86) Feng, T.; Ai, X.; An, G.; Yang, P.; Zhao, Y. Charge-Convertible Carbon Dots for Imaging-Guided Drug Delivery with Enhanced in Vivo Cancer Therapeutic Efficiency. *ACS Nano* **2016**, *10* (4), 4410–4420.

(87) Kang, Z.; Liu, Y.; Lee, S.; Chem, J. M. Carbon Nanodots: Synthesis, Properties and Applications. *J. Mater. Chem.* **2012**, *22* (46), 24230–24253.

(88) Gao, X.; Yang, L.; Petros, J. A.; Marshall, F. F.; Simons, J. W.; Nie, S. In Vivo Molecular and Cellular Imaging with Quantum Dots. *Curr. Opin. Biotechnol.* **2005**, *16* (1), 63–72.

(89) Sharma, P.; Brown, S.; Walter, G.; Santra, S.; Moudgil, B. Nanoparticles for Bioimaging. *Adv. Colloid Interface Sci.* **2006**, *123–126* (1), 471–485.

(90) Xu, Y.; Wu, M.; Liu, Y.; Feng, X. Z.; Yin, X. B.; He, X. W.; Zhang, Y. K. Nitrogen-Doped Carbon Dots: A Facile and General Preparation Method, Photoluminescence Investigation, and Imaging Applications. *Chem. - A Eur. J.* **2013**, *19* (7), 2276–2283.

(91) Wu, Z. L.; Zhang, P.; Gao, M. X.; Liu, C. F.; Wang, W.; Leng, F.; Huang, C. Z. One-Pot Hydrothermal Synthesis of Highly Luminescent Nitrogen-Doped Amphoteric Carbon Dots for Bioimaging from Bombyx Mori Silk – Natural Proteins. *J. Mater. Chem. B* **2013**, *1* (22), 2868.

(92) Yang, L.; Jiang, W.; Qiu, L.; Jiang, X.; Zuo, D.; Wang, D.; Yang, L. One Pot Synthesis of Highly Luminescent Polyethylene Glycol Anchored Carbon Dots Functionalized with a Nuclear Localization Signal Peptide for Cell Nucleus Imaging. *Nanoscale* **2015**, *7* (14), 6104–6113.

(93) Suri, S.; Fenniri, H.; Singh, B. Nanotechnology-Based Drug Delivery Systems. *J. Occup. Med. Toxicol.* **2007**, *2* (1), 16.

(94) Haley, B.; Frenkel, E. Nanoparticles for Drug Delivery in Cancer Treatment. *Urol. Oncol. Semin. Orig. Investig.* **2008**, *26* (1), 57–64.

(95) Bitar, A.; Ahmad, N. M.; Fessi, H.; Elaissari, A. Silica-Based Nanoparticles for Biomedical Applications. *Drug Discov. Today* **2012**, *17* (19–20), 1147–1154.

(96) Zhang, X. Gold Nanoparticles: Recent Advances in the Biomedical Applications. *Cell Biochem. Biophys.* **2015**, 771–775.

(97) Ge, L.; Li, Q.; Wang, M.; Ouyang, J.; Li, X.; Xing, M. M. Q. Nanosilver Particles in Medical Applications: Synthesis, Performance, and Toxicity. *Int. J. Nanomedicine* **2014**, *9* (1), 2399–2407.

(98) Jamieson, T.; Bakhshi, R.; Petrova, D.; Pocock, R.; Imani, M.; Seifalian, A. M. Biological Applications of Quantum Dots. *Biomaterials* **2007**, *28* (31), 4717–4732.

(99) Taghavi Pourianazar, N.; Mutlu, P.; Gunduz, U. Bioapplications of Poly(amidoamine) (PAMAM) Dendrimers in Nanomedicine. *J. Nanoparticle Res.* **2014**, *16* (4), 1–38.

(100) Alshehri, R.; Ilyas, A. M.; Hasan, A.; Arnaout, A.; Ahmed, F.; Memic, A. Carbon Nanotubes in Biomedical Applications: Factors, Mechanisms, and Remedies of Toxicity. *J. Med. Chem.* **2016**, *59* (18), 8149–8167.

(101) Tan, A.; de la Peña, H.; Seifalian, A. M. The Application of Exosomes as a Nanoscale Cancer Vaccine. *Int. J. Nanomedicine* **2010**, *5* (1), 889–900.

(102) Karthik, S.; Saha, B.; Ghosh, S. K.; Pradeep Singh, N. D. Photoresponsive Quinoline Tethered Fluorescent Carbon Dots for Regulated Anticancer Drug Delivery. *Chem. Commun.* **2013**, *49* (89), 10471–10473.

(103) Wang, H.-J.; He, X.; Luo, T.-Y.; Zhang, J.; Liu, Y.-H.; Yu, X.-Q.; Yang, L.; Zhang, L.; Hu, C.; Gu, F.; et al. Amphiphilic Carbon Dots as Versatile Vectors for Nucleic Acid and Drug Delivery. *Nanoscale* **2017**, *7*, 6104–6113.

(104) Ballabh, P.; Braun, A.; Nedergaard, M. The Blood-Brain Barrier: An Overview: Structure, Regulation, and Clinical Implications. *Neurobiol. Dis.* **2004**, *16* (1), 1–13.

(105) Xu, Hana; Zhifeng, Jingb; Wei, Wuc; Bing, Zouc; Zhili , Penga; Pengyu, Renb; Athula, Wikramanayakec; Zhongmin, Luc; Roger M., L. Biocompatible and Blood-Brain Barrier Permeable Carbon Dots for Inhibition of Aβ Fibrillation and Toxicity, and BACE1 Activity. *ACS Nano* **2017**, *9*, 12862–12866.

(106) Xu, B.; Zhao, C.; Wei, W.; Ren, J.; Miyoshi, D.; Sugimoto, N.; Qu, X. Aptamer Carbon Nanodot Sandwich Used for Fluorescent Detection of Protein. *Analyst* **2012**, *137* (23), 5483–5486.

(107) Jiang, Y.; Wang, Y.; Meng, F.; Wang, B.; Cheng, Y.; Zhu, C. N-Doped Carbon Dots Synthesized by Rapid Microwave Irradiation as Highly Fluorescent Probes for Pb 2+ Detection. *New J. Chem.* **2015**, *39* (5), 3357–3360.

(108) Bui, T. T.; Park, S.-Y. A Carbon Dot–hemoglobin Complex-Based Biosensor for Cholesterol Detection. *Green Chem.* **2016**, *18* (15), 4245–4253.

(109) Nie, H.; Li, M.; Li, Q.; Liang, S.; Tan, Y.; Sheng, L.; Shi, W.; Zhang, S. X. A. Carbon Dots with Continuously Tunable Full-Color Emission and Their Application in Ratiometric pH Sensing. *Chem. Mater.* **2014**, *26* (10), 3104–3112.

(110) Posthuma-Trumpie, G. A.; Wichers, J. H.; Koets, M.; Berendsen, L. B. J. M.; Van Amerongen, A. Amorphous Carbon Nanoparticles: A Versatile Label for Rapid Diagnostic (Immuno)assays. *Anal. Bioanal. Chem.* **2012**, *402* (2), 593–600.

(111) Yang, M.; Li, H.; Liu, J.; Kong, W.; Zhao, S.; Li, C.; Huang, H.; Liu, Y.; Kang, Z. Convenient and Sensitive Detection of Norfloxacin with Fluorescent Carbon Dots. *J. Mater. Chem. B* **2014**, *2* (45), 7964–7970.

(112) Bai, W.; Zheng, H.; Long, Y.; Mao, X.; Gao, M.; Zhang, L. A Carbon Dots-Based Fluorescence Turn-on Method for DNA Determination. *Anal. Sci.* **2011**, *27* (3), 243–246.

(113) Wang, Y.; Zhang, L.; Liang, R. P.; Bai, J. M.; Qiu, J. D. Using Graphene Quantum Dots as Photoluminescent Probes for Protein Kinase Sensing. *Anal. Chem.* **2013**, *85* (19), 9148–9155.

(114) Mohapatra, S.; Sahu, S.; Nayak, S.; Ghosh, S. K. Design of Fe3O4@SiO2@Carbon Quantum Dot Based Nanostructure for Fluorescence Sensing, Magnetic Separation, and Live Cell Imaging of Fluoride Ion. *Langmuir* **2015**, *31* (29), 8111–8120.

(115) Wang, Z.; Long, P.; Feng, Y.; Qin, C.; Feng, W. Surface Passivation of Carbon Dots with Ethylene Glycol and Their High-Sensitivity to Fe^{3+}. *RSC Adv.* **2017**, *7* (5), 2810–2816.

(116) Yang, S.; Feng, X.; Wang, X.; Müllen, K. Graphene-Based Carbon Nitride Nanosheets as Efficient Metal-Free Electrocatalysts for Oxygen Reduction Reactions. *Angew. Chemie - Int. Ed.* **2011**, *50* (23), 5339–5343.

(117) Hu, C.; Yu, C.; Li, M.; Wang, X.; Dong, Q.; Wang, G.; Qiu, J. Nitrogen-Doped Carbon Dots Decorated on Graphene: A Novel All-Carbon Hybrid Electrocatalyst for Enhanced Oxygen Reduction Reaction. *Chem. Commun.* **2015**, *51* (16), 3419–3422.

(118) Wang, F.; Chen, Y.; Liu, C.; Ma, D. White Light-Emitting Devices Based on Carbon Dots' Electroluminescence. *Chem. Commun.* **2011**, *47* (12), 3502–3504.

(119) Liu, S.-S.; Wang, C.-F.; Li, C.-X.; Wang, J.; Mao, L.-H.; Chen, S. Hair-Derived Carbon Dots toward Versatile Multidimensional Fluorescent Materials. *J. Mater. Chem. C* **2014**, *2* (32), 6477–6483.

(120) Xu, H.; Yang, X.; Li, G.; Zhao, C.; Liao, X. Supporting Information: Green Synthesis of Fluorescent Carbon Dots for Selective Detection of Tartrazine in Food Samples. *J. Agric. Food Chem.* **2015**, *63* (30), 6707–6714.

(121) Arcudi, F.; Strauss, V.; Dordevic, L.; Cadranel, A.; Guldi, D.; Prato, M. Porphyrin Antennas on Carbon Nanodots: Excited State Energy and Electron Transduction. *Angew. Chemie Int. Ed.* **2017**, *56* (40), 12097–12101.

(122) Park, Y.; Yoo, J.; Lim, B.; Kwon, W.; Rhee, S.-W. Improving the Functionality of Carbon Nanodots: Doping and Surface Functionalization. *J. Mater. Chem. A* **2016**, *4* (30), 11582–11603.

(123) Qian, Z.; Ma, J.; Shan, X.; Feng, H.; Shao, L.; Chen, J. Highly Luminescent N-Doped Carbon Quantum Dots as an Effective Multifunctional Fluorescence Sensing Platform. *Chem. Eur. J.* **2014**, *20* (8), 2254–2263.

(124) Zheng, M.; Xie, Z.; Qu, D.; Li, D.; Du, P.; Jing, X.; Sun, Z. On-off-on Fluorescent Carbon Dot Nanosensor for Recognition of chromium(VI) and Ascorbic Acid Based on the Inner Filter Effect. *ACS Appl. Mater. Interfaces* **2013**, *5* (24), 13242–13247.

(125) Qu, D.; Zheng, M.; Du, P.; Zhou, Y.; Zhang, L.; Li, D.; Tan, H.; Zhao, Z.; Xie, Z.; Sun, Z. Highly Luminescent S, N Co-Doped Graphene Quantum Dots with Broad Visible Absorption Bands for Visible Light Photocatalysts. *Nanoscale* **2013**, *5* (24), 12272–12277.

(126) Liu, Y.; Zhou, L.; Li, Y.; Deng, R.; Zhang, H. Highly Fluorescent Nitrogen-Doped Carbon Dots with Excellent Thermal and Photo Stability Applied as Invisible Ink for Loading Important Information and Anti-Counterfeiting. *Nanoscale* **2017**, *9* (2), 491–496.

(127) He, G.; Shu, M.; Yang, Z.; Ma, Y.; Huang, D.; Xu, S.; Wang, Y.; Hu, N.; Zhang, Y.; Xu, L. Microwave Formation and Photoluminescence Mechanisms of Multi-States Nitrogen Doped Carbon Dots. *Appl. Surf. Sci.* **2017**, *422*, 257–265.

(128) Shi, L.; Zhao, B.; Li, X.; Zhang, G.; Zhang, Y.; Dong, C.; Shuang, S. Eco-Friendly Synthesis of Nitrogen-Doped Carbon Nanodots from Wool for Multicolor Cell Imaging, Patterning, and Biosensing. *Sensors Actuators, B Chem.* **2016**, *235*, 316–324.

(129) Nagavarma, B. V. N.; Yadav, H. K. S.; Ayaz, A.; Vasudha, L. S.; Shivakumar, H. G. Different Techniques for Preparation of Polymeric Nanoparticles- A Review. *Asian J. Pharm. Clin. Res.* **2012**, *5* (3), 16–23.

(130) Du, F.; Zeng, F.; Ming, Y.; Wu, S. Carbon Dots-Based Fluorescent Probes for Sensitive and Selective Detection of Iodide. *Microchim. Acta* **2013**, *180*, 453–460.

(131) Qu, D.; Zheng, M.; Zhang, L.; Zhao, H.; Xie, Z.; Jing, X.; Haddad, R. E. Formation Mechanism and Optimization of Highly Luminescent N-Doped Graphene. *Sci. Rep.* **2014**, *4*, 1–9.

(132) Wang, Y.; Zhu, Y.; Yu, S.; Jiang, C. RSC Advances Optical Properties and Analytical Applications. *RSC Adv.* **2017**, *7*, 40973–40989.

(133) Wang, Y.; Hu, A. Carbon Quantum Dots: Synthesis, Properties and Applications. *J. Mater. Chem. C* **2014**, *2* (34), 6921–6939.

(134) Cayuela, A.; Soriano, M. L.; Carrillo-Carrión, C.; Valcárcel, M. Semiconductor and Carbon-Based Fluorescent Nanodots: The Need for Consistency. *Chem. Commun.* **2016**, *52* (7), 1311–1326.

(135) Würth, C.; Grabolle, M.; Pauli, J.; Spieles, M.; Resch-genger, U. Relative and Absolute Determination of Fluorescence Quantum Yields of Transparent Samples. *Nat. Protoc.* **2013**, *8* (8), 1535–1550.

(136) Brenner, S.; Horne, R. W. A Negative Staining Method for High Resolution Electron Microscopy of Viruses. *Biochim. Biophys. Acta* **1959**, *34*, 103–110.

(137) Mout, R.; Moyano, D. F.; Rana, S.; Rotello, V. M. Surface Functionalization of Nanoparticles for Nanomedicine. *Chem. Soc. Rev.* **2012**, *41* (7), 2539–2544.

(138) Liu, W.; Li, C.; Ren, Y.; Sun, X.; Pan, W.; Li, Y.; Wang, J.; Wang, W. Carbon Dots: Surface Engineering and Applications. *J. Mater. Chem. B* **2016**, *4* (35), 5772–5788.

(139) Dimos, K. Carbon Quantum Dots: Surface Passivation and Functionalization. *Curr. Org. Chem.* **2016**, *20*, 682–695.

(140) Williams, A.; Ibrahim, I. T. Carbodiimide Chemistry: Recent Advances. *Chem. Rev.* **1981**, *81* (6), 589–636.

(141) Huang, P.; Lin, J.; Wang, X.; Wang, Z.; Zhang, C.; He, M.; Wang, K.; Chen, F.; Li, Z.; Shen, G.; et al. Light-Triggered Theranostics Based on Photosensitizer-Conjugated Carbon Dots for Simultaneous Enhanced-Fluorescence Imaging and Photodynamic Therapy. *Adv. Mater.* **2012**, *24* (37), 5104–5110.

(142) Shi, W.; Li, X.; Ma, H. A Tunable Ratiometric Ph Sensor Based on Carbon Nanodots for the Quantitative Measurement of the Intracellular pH of Whole Cells. *Angew. Chemie - Int. Ed.* **2012**, *51* (26), 6432–6435.

(143) Du, F.; Ming, Y.; Zeng, F.; Yu, C.; Wu, S. A Low Cytotoxic and Ratiometric Fluorescent Nanosensor Based on Carbon-Dots for Intracellular pH Sensing and Mapping. *Nanotechnology* **2013**, *24* (36), 365101.

(144) Matyjaszewski, K.; Xia, J. Atom Transfer Radical Polymerization. *Chem. Rev.* **2001**, *101* (9), 2921–2990.

(145) Nurettin Sahiner, and S. B. S. Functionalization of Carbon Particles by Atom Transfer Radical Polymerization. *MRS Adv.* **2017**, 1–8.

(146) Ye, J.; Narain, R. Water-Assisted Atom Transfer Radical Polymerization of N-Isopropylacrylamide: Nature of Solvent and Temperature. *J. Phys. Chem. B* **2009**, *113* (3), 676–681.

(147) Cheng, L.; Li, Y.; Zhai, X.; Xu, B.; Cao, Z.; Liu, W. Polycation-B-Polyzwitterion Copolymer Grafted Luminescent Carbon Dots as a Multifunctional Platform for Serum-Resistant Gene Delivery and Bioimaging. *ACS Appl. Mater. Interfaces* **2014**, *6* (22), 20487–20497.

(148) Zhang, J.; Zheng, M.; Xie, Z. Co-Assembled Hybrids of Proteins and Carbon Dots for Intracellular Protein Delivery. *J. Mater. Chem. B* **2016**, *4* (34), 5659–5663.

(149) Kudr, J.; Richtera, L.; Xhaxhiu, K.; Hynek, D.; Heger, Z.; Zitka, O.; Adam, V. Carbon Dots Based FRET for the Detection of DNA Damage. *Biosens. Bioelectron.* **2017**, *92*, 133–139.

(150) Lei, D.; Yang, W.; Gong, Y.; Jing, J.; Nie, H.; Yu, B.; Zhang, X. Non-Covalent Decoration of Carbon Dots with Folic Acid via a Polymer-Assisted Strategy for Fast and Targeted Cancer Cell Fluorescence Imaging. *Sensors Actuators, B Chem.* **2016**, *230*, 714–720.

(151) Wu, Y.-F.; Wu, H.-C.; Kuan, C.-H.; Lin, C.-J.; Wang, L.-W.; Chang, C.-W.; Wang, T.-W. Multi-Functionalized Carbon Dots as Theranostic Nanoagent for Gene Delivery in Lung Cancer Therapy. *Sci. Rep.* **2016**, *6* (1), 21170–21182.

(152) Datta, K. K. R.; Kozák, O.; Ranc, V.; Havrdová, M.; Bourlinos, a B.; Šafářová, K.; Holá, K.; Tománková, K.; Zoppellaro, G.; Otyepka, M.; et al. Quaternized Carbon Dot-Modified Graphene Oxide for Selective Cell Labelling – Controlled Nucleus and Cytoplasm Imaging. *Chem. Commun.* **2014**, *50* (74), 10782–10785.

(153) Liu, Q.; Xu, S.; Niu, C.; Li, M.; He, D.; Lu, Z.; Ma, L.; Na, N.; Huang, F.; Jiang, H.; et al. Distinguish Cancer Cells Based on Targeting Turn-on Fluorescence Imaging by Folate Functionalized Green Emitting Carbon Dots. *Biosens. Bioelectron.* **2014**, *64*, 119–125.

(154) Salmaso, S.; Caliceti, P. Stealth Properties to Improve Therapeutic Efficacy of Drug Nanocarriers. *J. Drug Deliv.* **2013**, *2013*, 1–19.

(155) Zuffanti, S. Preparation of Acyl Chlorides with Thionyl Chloride. *J. Chem. Educ.* **1948**, *25* (9), 481.

(156) Kapuscinski, J. DAPI: A DNA-Specific Fluorescent Probe. *Biotech. Histochem.* **1995**, *70* (5), 220–233.

(157) Plank, C.; Schillinger, U.; Scherer, F.; Bergemann, C.; Remy, J. S.; Krotz, F.; Anton, M.; Lausier, J.; Rosenecker, J. The Magnetofection Method: Using Magnetic Force to Enhance Gene Delivery. *Biol. Chem.* **2003**, *384* (5), 737–747.

(158) Vegerhof, A.; Motei, M.; Rudinzky, A.; Malka, D.; Popovtzer, R.; Zalevsky, Z. Thermal Therapy with Magnetic Nanoparticles for Cell Destruction. *Biomed. Opt. Express* **2016**, *7* (11), 4581–4494.

(159) Tripathi, K. M.; Tran, T. S.; Tung, T. T.; Losic, D.; Kim, T. Water Soluble Fluorescent Carbon Nanodots from Biosource for Cells Imaging. *J. Nanomater.* **2017**, *2017*, 1–10.

(160) Askar, F. W. Synthesis and Characterization of New. *Macromolecules* **2013**, *52* (1), 453–465.

(161) Stanicki, D.; Boutry, S.; Laurent, S.; Wacheul, L.; Nicolas, E.; Crombez, D.; Vander Elst, L.; Lafontaine, D. L. J.; Muller, R. N. Carboxy-Silane Coated Iron Oxide Nanoparticles: A Convenient Platform for Cellular and Small Animal Imaging. *J. Mater. Chem. B* **2014**, *2* (4), 387–397.

(162) Bruce, I. J.; Sen, T. Surface Modification of Magnetic Nanoparticles with Alkoxysilanes and Their Application in Magnetic Bioseparations. *Langmuir* **2005**, *21* (15), 7029–7035.

(163) Zaitsev, V. N.; Kobylinskaya, N. G.; Kostenko, L. S.; Gerda, V. I. Conductometric Determination of the Concentration of Acid Centers on Functionalized Materials. *J. Anal. Chem.* **2008**, *63* (8), 779–786.

(164) Pastorin, G.; Wu, W.; Wieckowski, S.; Briand, J.-P.; Kostarelos, K.; Prato, M.; Bianco, A. Double Functionalisation of Carbon Nanotubes for Multimodal Drug Delivery. *Chem. Commun.* **2006**, *1* (11), 1182–1184.

(165) Yuan, Y.; Guo, B.; Hao, L.; Liu, N.; Lin, Y.; Guo, W.; Li, X.; Gu, B. Doxorubicin-Loaded Environmentally Friendly Carbon Dots as a Novel Drug Delivery System for Nucleus Targeted Cancer Therapy. *Colloids Surfaces B Biointerfaces* **2017**, *159*, 349–359.

(166) Jahangirian, H.; Lemraski, E.; Webster, T.; Rafiee-Moghaddam, R.; Abdollahi, Y. A Review of Drug Delivery Systems Based on Nanotechnology and Green Chemistry: Green Nanomedicine. *Int. J. Nanomedicine* **2017**, *12*, 2957–2978.

(167) Wani, M. C.; Taylor, H. L.; Wall, M. E.; Coggon, P.; McPhail, a T. Plant Antitumor Agents. VI. The Isolation and Structure of Taxol, a Novel Antileukemic and Antitumor Agent from Taxus Brevifolia. *J. Am. Chem. Soc.* **1971**, *93* (9), 2325–2327.

(168) World Health Organization. 19th WHO Model List of Essential Medicines. *Http://Www.Who.Int/Medicines/Publications/Essentialmedicines/En* **2015**, No. April, 1–43.

(169) Kops, G. J.; Weaver, B. A.; Cleveland, D. W. On the Road to Cancer: Aneuploidy and the Mitotic Checkpoint. *Nat. Rev. Cancer* **2005**, *5* (10), 773–785.

(170) Lara-Gonzalez, P.; Westhorpe, F. G.; Taylor, S. S. The Spindle Assembly Checkpoint. *Curr. Biol.* **2012**, *22* (22), R966–R980.

(171) Mekhail, T. M.; Markman, M. Paclitaxel in Cancer Therapy. *Expert Opin. Pharmacother.* **2002**, *3* (6), 755–766.

(172) Weaver, B. A. How Taxol/paclitaxel Kills Cancer Cells. *Mol. Biol. Cell* **2014**, *25* (18), 2677–2681.

(173) Hillmen, P.; Gribben, J. G.; Follows, G. A.; Milligan, D.; Sayala, H. A.; Moreton, P.; Oscier, D. G.; Dearden, C. E.; Kennedy, D. B.; Pettitt, A. R.; et al. Rituximab plus Chlorambucil as First-Line Treatment for Chronic Lymphocytic Leukemia: Final Analysis of an Open-Label Phase II Study. *J. Clin. Oncol.* **2014**, *32* (12), 1236–1241.

(174) Begleiter, A.; Mowat, M.; Israels, L. G.; Johnston, J. B. Chlorambucil in Chronic Lymphocytic Leukemia-Mechanism of Action. *Leuk. Lymphoma* **1996**, *23*, 187–201.

(175) Deutsch, H. M.; Glinski, J. a; Hernandez, M.; Haugwitz, R. D.; Narayanan, V. L.; Suffness, M.; Zalkow, L. H. Synthesis of Congeners and Prodrugs. 3. Water-Soluble Prodrugs of Taxol with Potent Antitumor Activity. *J. Med. Chem.* **1989**, *32* (2), 788–792.

(176) Xu, Z.; Zhu, S.; Wang, M.; Li, Y.; Shi, P.; Huang, X. Delivery of Paclitaxel Using PEGylated Graphene Oxide as a Nanocarrier. *ACS Appl. Mater. Interfaces* **2015**, *7* (2), 1355–1363.

(177) Zhu, S.; Meng, Q.; Wang, L.; Zhang, J.; Song, Y.; Jin, H.; Zhang, K.; Sun, H.; Wang, H.; Yang, B. Highly Photoluminescent Carbon Dots for Multicolor Patterning , Sensors , and Bioimaging. *Angew. Chem., Int. Ed.* **2013**, *52* (14), 1–6.

(178) Liu, S.; Tian, J.; Wang, L.; Zhang, Y.; Qin, X.; Luo, Y.; Asiri, A. M.; Al-youbi, A. O.; Sun, X. Hydrothermal Treatment of Grass : A Low-Cost , Green Route to Nitrogen-Doped , Carbon-Rich , Photoluminescent Polymer Nanodots as an Effective Fluorescent Sensing Platform for Label-Free Detection of Cu (II) Ions. *Adv. Mater.* **2012**, *24*, 2037–2041.

(179) Cedervall, T.; Lynch, I.; Lindman, S.; Berggård, T.; Thulin, E.; Nilsson, H.; Dawson, K. A.; Linse, S. Understanding the Nanoparticle – Protein Corona Using Methods to Quantify Exchange Rates and Affinities of Proteins for Nanoparticles. *PNAS* **2007**, *104* (7), 2050–2055.

(180) Johnston, B. D.; Kreyling, W. G.; Pfeiffer, C.; Schäffler, M.; Sarioglu, H.; Ristig, S.; Hirn, S.; Haberl, N.; Thalhammer, S.; Hauck, S. M.; et al. Colloidal Stability and Surface Chemistry Are Key Factors for the Composition of the Protein Corona of Inorganic Gold Nanoparticles. *Adv. Funct. Mater.* **2017**, *27* (42), 1701956–1701965.

(181) Zhu, Y.; Li, W.; Li, Q.; Li, Y.; Li, Y.; Zhang, X.; Huang, Q. Effects of Serum Proteins on Intracellular Uptake and Cytotoxicity of Carbon Nanoparticles. *Carbon N. Y.* **2009**, *47* (5), 1351–1358.

(182) Hu, W.; Peng, C.; Lv, M.; Li, X.; Zhang, Y.; Chen, N.; Fan, C.; Huang, Q. Protein Corona-Mediated Mitigation of Cytotoxicity of Graphene Oxide. *ACS Nano* **2011**, *5* (5), 3693–3700.

(183) Wang, W.; Damm, C.; Walter, J.; Nacken, T. J.; Peukert, W. Photobleaching and Stabilization of Carbon Nanodots Produced by Solvothermal Synthesis. *Phys Chem Chem Phys* **2016**, *18* (1), 466–475.

(184) Fleischer, C. C.; Payne, C. K. Nanoparticle − Cell Interactions: Molecular Structure of the Protein Corona and Cellular Outcomes. *Acc. Chem. Res.* **2014**, *47* (8), 2651–2659.

(185) Chanana, M.; Gil, P. R.; Correa-duarte, M. A.; Liz-marzan, L. M.; Parak, W. J. Physicochemical Properties of Protein-Coated Gold Nanoparticles in Biological Fluids and Cells before and after Proteolytic Digestion. *Angew. Chemie Int. Ed.* **2013**, *52*, 4179–4183.

(186) Treuel, L.; Eslahian, K. A.; Docter, D.; Lang, T.; Zellner, R.; Nienhaus, K.; Nienhaus, G. U.; Stauber, R. H.; Maskos, M. Physicochemical Characterization of Nanoparticles and Their Behavior in the Biological Environment. *Phys. Chem. Chem. Phys.* **2014**, *16*, 15053–15067.

(187) Tang, J.; Kong, B.; Wu, H.; Xu, M.; Wang, Y.; Wang, Y.; Zhao, D.; Zheng, G. Carbon Nanodots Featuring Efficient FRET for Real-Time Monitoring of Drug Delivery and Two-Photon Imaging. *Adv. Mater.* **2013**, *25* (45), 6569–6574.

(188) Chen, Z.; Wang, X.; Li, H.; Li, C.; Lu, Q.; Yang, G.; Long, J.; Meng, L. Controllable and Mass Fabrication of Highly Luminescent N-Doped Carbon Dots for Bioimaging Applications. *RSC Adv.* **2015**, *5* (29), 22343–22349.

(189) Li, S.; Amat, D.; Peng, Z.; Vanni, S.; Raskin, S.; De Angulo, G.; Othman, A. M.; Graham, R. M.; Leblanc, R. M. Transferrin Conjugated Nontoxic Carbon Dots for Doxorubicin Delivery to Target Pediatric Brain Tumor Cells. *Nanoscale* **2016**, *8* (37), 16662–16669.

(190) Etame, A. B.; Smith, C. A.; Chan, W. C. W.; Rutka, J. T. Design and Potential Application of PEGylated Gold Nanoparticles with Size-Dependent Permeation through Brain Microvasculature. *Nanomedicine Nanotechnology, Biol. Med.* **2011**, *7* (6), 992–1000.

(191) Mosmann, T. Rapid Colorimetric Assay for Cellular Growth and Survival: Application to Proliferation and Cytotoxicity Assays. *J. Immunol. Methods* **1983**, *65* (1–2), 55–63.

(192) Zhao, Q.-L.; Zhang, Z.-L.; Huang, B.-H.; Peng, J.; Zhang, M.; Pang, D.-W. Facile Preparation of Low Cytotoxicity Fluorescent Carbon Nanocrystals by Electrooxidation of Graphite. *Chem. Commun.* **2008**, *281* (41), 5116–5118.

(193) Zhu, Z. J.; Posati, T.; Moyano, D. F.; Tang, R.; Yan, B.; Vachet, R. W.; Rotello, V. M. The Interplay of Monolayer Structure and Serum Protein Interactions on the Cellular Uptake of Gold Nanoparticles. *Small* **2012**, *8* (17), 2659–2663.

(194) Liu, J. H.; Cao, L.; LeCroy, G. E.; Wang, P.; Meziani, M. J.; Dong, Y.; Liu, Y.; Luo, P. G.; Sun, Y. P. Carbon 'Quantum' Dots for Fluorescence Labeling of Cells. *ACS Appl. Mater. Interfaces* **2015**, *7* (34), 19439–19445.

(195) Wang, Y.; Anilkumar, P.; Cao, L.; Liu, J. H.; Luo, P. G.; Tackett 2nd, K. N.; Sahu, S.; Wang, P.; Wang, X.; Sun, Y. P. Carbon Dots of Different Composition and Surface Functionalization: Cytotoxicity Issues Relevant to Fluorescence Cell Imaging. *Exp Biol Med* **2011**, *236* (11), 1231–1238.

(196) Zhou, N.; Zhu, S.; Maharjan, S.; Hao, Z.; Song, Y.; Zhao, X.; Jiang, Y.; Yang, B.; Lu, L. RSC Advances Tra Ffi Cking , and Exocytosis of Carbon Dots in Neural. *RSC Adv.* **2014**, *4*, 62086–62095.

(197) Scarcelli, G.; Yun, S. H.; Hahn, S. K. Bioimaging of Hyaluronic Acid Derivatives Using Nanosized Carbon Dots. *Biomacromolecules* **2012**, *13*, 2554–2561.

(198) De Jong, W. H.; Borm, P. J. A. Drug Delivery and Nanoparticles:applications and Hazards. *Int. J. Nanomedicine* **2008**, *3* (2), 133–149.

(199) Lesniak, A.; Fenaroli, F.; Monopoli, M. P.; Aberg, C.; Dawson, K. A.; Salvati, A. Effects of the Presence or Absence of a Protein Corona on Silica Nanoparticle Uptake and Impact on Cells. *ACS Nano* **2012**, *6* (7), 5845–5857.

(200) Treuel, L.; Brandholt, S.; Maffre, P.; Wiegele, S.; Shang, L.; Nienhaus, G. U. Impact of Protein Modification on the Protein Corona on Nanoparticles and Nanoparticle-Cell Interactions. *ACS Nano* **2014**, *8* (1), 503–513.

(201) Treuel, L.; Nienhaus, G. U. Toward a Molecular Understanding of Nanoparticle-Protein Interactions. *Biophys. Rev.* **2012**, *4* (2), 137–147.

(202) Solly, K.; Wang, X.; Xu, X.; Strulovici, B.; Zheng, W. Application of Real-Time Cell Electronic Sensing (RT-CES) Technology to Cell-Based Assays. *Assay Drug Dev. Technol.* **2004**, *2* (4), 363–372.

(203) Abassi, Y. A.; Xi, B.; Zhang, W.; Ye, P.; Kirstein, S. L.; Gaylord, M. R.; Feinstein, S. C.; Wang, X.; Xu, X. Kinetic Cell-Based Morphological Screening: Prediction of Mechanism of Compound Action and Off-Target Effects. *Chem. Biol.* **2009**, *16* (7), 712–723.

(204) Liebert, M. A.; Atienza, J. M.; Yu, N.; Kirstein, S. L.; Xi, B.; Wang, X.; Xu, X.; Abassi, Y. a. Dynamic and Label-Free Cell-Based Assays Using the Real-Time Cell Electronic Sensing System. *Assay Drug Dev. Technol.* **2006**, *4* (5), 597–607.

(205) Yang, Y.; Aloysius, H.; Inoyama, D.; Chen, Y.; Hu, L. Enzyme-Mediated Hydrolytic Activation of Prodrugs. *Acta Pharm. Sin. B* **2011**, *1* (3), 143–159.

(206) Ojima, I.; Das, M. Recent Advances in the Chemistry and Biology of New Generation Taxoids. *J. Nat. Prod.* **2009**, *72*, 554–565.

(207) Kihlmark, M.; Imreh, G.; Hallberg, E. Sequential Degradation of Proteins from the Nuclear Envelope during Apoptosis. *J. Cell Sci.* **2001**, *114* (Pt 20), 3643–3653.

(208) Mellado, W.; Garcia-arenasi, R.; Magri, N. F.; Or, G. A.; Kingstonl, D. G.-; Horwitz, S. B. Preparation and Biological Activity of Taxol Acetates. *Biochem. Biophys. Res. Commun.* **1984**, *124* (2), 329–336.

(209) Sansing, H. A.; Renner, N. A.; MacLean, A. G. An Inverted Blood-Brain Barrier Model That Permits Interactions between Glia and Inflammatory Stimuli. *J. Neurosci. Methods* **2012**, *207* (1), 91–96.

(210) Hanada, S.; Fujioka, K.; Inoue, Y.; Kanaya, F.; Manome, Y. Cell-Based in Vitro Blood – Brain Barrier Model Can Rapidly Evaluate Nanoparticles ' Brain Permeability in Association with Particle Size and Surface Modification. *Int. J. Mol. Sci.* **2014**, *15*, 1812–1825.

(211) Lundholt, B. K.; Scudder, K. M.; Pagliaro, L. A Simple Technique for Reducing Edge Effect in Cell-Based Assays. *J. Biomol. Screen.* **2003**, *8* (5), 566–570.

"It always seems impossible until it is done"
Nelson Mandela